

Enabling Active Nanotechnologies by Phase Transition: From Electronics, Photonics to Thermotics

Chunqi Zheng, Robert E. Simpson, Kechao Tang, Yujie Ke, Arash Nematy, Qing Zhang, Guangwei Hu, Chengkuo Lee, Jinghua Teng, Joel K.W. Yang, Junqiao Wu, and Cheng-Wei Qiu*



Cite This: *Chem. Rev.* 2022, 122, 15450–15500



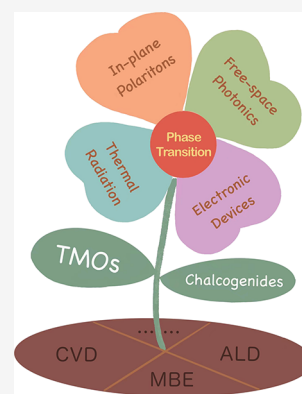
Read Online

ACCESS |

Metrics & More

Article Recommendations

ABSTRACT: Phase transitions can occur in certain materials such as transition metal oxides (TMOs) and chalcogenides when there is a change in external conditions such as temperature and pressure. Along with phase transitions in these phase change materials (PCMs) come dramatic contrasts in various physical properties, which can be engineered to manipulate electrons, photons, polaritons, and phonons at the nanoscale, offering new opportunities for reconfigurable, active nanodevices. In this review, we particularly discuss phase-transition-enabled active nanotechnologies in nonvolatile electrical memory, tunable metamaterials, and metasurfaces for manipulation of both free-space photons and in-plane polaritons, and multifunctional emissivity control in the infrared (IR) spectrum. The fundamentals of PCMs are first introduced to explain the origins and principles of phase transitions. Thereafter, we discuss multiphysical nanodevices for electronic, photonic, and thermal management, attesting to the broad applications and exciting promises of PCMs. Emerging trends and valuable applications in all-optical neuromorphic devices, thermal data storage, and encryption are outlined in the end.



CONTENTS

1. Introduction	15451	3.3. Phase Transition Based Neuromorphic Devices	15468
2. Materials Physics and Chemistry of Phase Transition	15452	4. Phase Transition for Nanophotonics	15470
2.1. Introduction of Phase Transition	15452	4.1. Tunable Metasurfaces for Dynamic Light Intensity Control	15471
2.2. TMOs	15453	4.2. Tunable Metasurfaces for Wavefront Manipulation	15471
2.2.1. Introduction of TMOs	15453	4.3. Tunable Integrated Photonic Devices	15473
2.2.2. Properties of TMOs	15455	4.4. Phase Transition for in-Plane Polaritons	15474
2.2.3. Modulation of T_{MIT}	15455	4.4.1. Polaritons in Different Types of Materials	15474
2.2.4. Fabrication Technologies	15455	4.4.2. Phase Transition Based Plasmonic Devices	15475
2.3. Chalcogenide PCMs	15456	4.4.3. Reversible Switching of Low-Loss and Highly Confined Polaritons	15478
2.3.1. Introduction of Chalcogenides	15456	4.4.4. Phase Transition for van der Waals (vdWs) Polaritonic devices	15479
2.3.2. The Physical Origin of Amorphous-to-Crystalline Phase Transition	15457	5. Phase Transition for Thermal Radiation	15479
2.3.3. Stimulation Technologies of Chalcogenides	15459	5.1. Phase Transition Based Thermal Emission Control	15479
2.3.4. Fabrication of Chalcogenides	15461	5.1.1. IR Camouflage	15479
3. Phase Transition for Electronic Nanodevices	15461	5.1.2. Self-Adaptive Radiative Cooling	15480
3.1. Electrical Properties of PCMs	15462		
3.2. Phase Transition Based Nonvolatile Memory (NVM)	15463		
3.2.1. Compositional Modification via Doping	15463		
3.2.2. New Material Developments	15464		
3.2.3. Novel Cell Designs	15465		
3.2.4. Heterostructures with a Single Interfacial Layer	15466		
3.2.5. Superlattices and Superlattice-Like (SLL) Heterostructures	15467		

Special Issue: Chemistry of Metamaterials

Received: March 14, 2022

Published: July 27, 2022



5.1.3. Dynamic Spatial Control of Thermal Emission	15482
5.2. Thermal Properties and Applications of W-doped VO ₂ (W-VO ₂)	15482
6. Conclusion Remarks and Outlook	15484
6.1. Future Tunable Electronic Devices	15485
6.2. Reconfigurable Active Nanophotonics	15485
6.3. Dynamic Thermal Radiation Control	15486
Author Information	15486
Corresponding Author	15486
Authors	15486
Author Contributions	15487
Notes	15487
Biographies	15487
Acknowledgments	15488
Abbreviations	15488
References	15489

1. INTRODUCTION

The realization of dynamic and reconfigurable functional nanodevices has been a long-term pursuit, where many avenues have been explored. Spatiotemporal control can be achieved via operation near critical points where physical properties of materials present strong dependencies on external conditions.¹ For instance, electrical gating is one important approach in nanoelectronics. Applying electrical potential can be used to modulate the resistivity of AgS nanodots via the removal of dopant atoms² and to modulate the bandgap^{3,4} of low-dimensional nanomaterials such as graphene and black phosphorus (BP). In nanophotonics, multiphysics processes can be exploited, using optical nonlinearity,⁵ thermal-optic effect,⁶ electro-optical effect,⁷ and nanomechanical actuation^{8–11} to tune electromagnetic wave response of materials for multiple functions. However, further applications of these modulation technologies are hindered due to different limitations. For example, chemical engineering is usually slow, mechanical control is faced with the problems of accuracy and reliability, and optical nonlinearity and thermal-optical effect are too weak, which require high excitation power. All these factors restrict the tuning range and efficiency of nanodevices.

Phase transition, a physical process for a medium varying from one state to the other, is ubiquitous and offers an alternative avenue to modulate the response of materials. One of the most well-known examples is the phase transition of water among solid, liquid, and gas states: when ice absorbs enough heat it transits to liquid states; when liquid water is heated to the boiling point, it can transfer to the gaseous state. Besides, the ambient pressure plays deterministic roles in the phase transition of water. Together, the property of water, such as density, viscosity, and others, can vary significantly. Beyond this commonly observed transformation among basic states, many more complicated kinds of phase transitions can exist, all usually accompanied by dramatic change of specific or multiple physical properties. For instance, the electrical conductivity drops suddenly after metal-to-insulator transition (MIT);¹² materials lose their permanent magnetic properties when heated above the Curie point, known as ferromagnetism to paramagnetism switching;¹³ optical dielectric constant changes obviously in the presence of amorphous and crystalline phase change.¹⁴

Taking advantage of these tailorable physical properties, the phase transition has become a promising route toward active nanotechnologies, spanning from electronics, photonics, and

thermotics to many other important scientific branches.^{15–22} In this work, we selectively focus on two classes of PCMs, TMOs and chalcogenides, for reconfigurable nanotechnologies. We note that, although there are various material systems with exciting phase transition properties, we focus on these two emerging PCMs because they host various phases, which can be flexibly modulated in the nanoscale and that our discussions of its modulation mechanism herein can facilitate the understanding of other systems and technologies (such as inorganic and organic compounds for heat storage), for which the interested readers can refer to several existing literature.^{23,24}

TMOs are compounds formed by combining transition metals with oxygen atoms. One of their peculiar properties is MIT, accompanied by change of various physical properties. The vanadium dioxide (VO₂) is a typical TMO, which switches from insulator to metal state at $T_{\text{MIT}} = 67$ °C. During its MIT, both the optical and thermal properties change dramatically (dielectric constant of 4.9 switch to $-35 + 119i$ near 10.6 μm ;²⁵ and thermal emissivity can drop with large contrast at IR region²⁶), making the material a promising candidate for reconfigurable photonic devices^{25,27,28} and thermal radiation control.^{26,29–31} Furthermore, the phase change temperature of TMOs can be controlled via doping various impurities such as tungsten, offering more freedom to manipulate this transition. In addition, considering that the in situ fine modulation of ambient temperatures could be available with the resolution of few tens of nanometers, TMOs hence could support the nanoscale tunable functionalities in the field of optics, information technology, and energy. Examples include photonic metacanvas,²⁵ IR camouflage,²⁶ thermal imaging sensitizer (TIS),²⁹ and temperature-adaptive radiative coolers,³¹ which we will discuss in detail.

Alternatively, the amorphous-to-crystalline transition occurs in binary and ternary chalcogenide alloys when the material is heated above its phase transition temperature.¹⁵ During the phase change process, both the electrical conductivity and the refractive index increase.³² Chalcogenides can support large resistance contrast and nonvolatile property during the transition, important for electrical NVM and breaking the limit of classical memory.³³ Besides, the continuous crystallization and reamorphization process of chalcogenides can enable neuromorphic devices including artificial neurons,^{34,35} synapses,³⁶ and other novel devices,^{37–39} providing a new platform of neuromorphic computing. In optical systems where high integration, miniaturization, programmability, and multiple functionalities are favored, chalcogenide nanostructures can be a suitable candidate. The composition of those deeply sub-wavelength nanostructures can form an artificial media, with optical properties that are unattainable in nature, known as metamaterials, where each constituent structure is called the meta-atom.⁴⁰ The direct engineering of phase-change meta-atoms would pave a new way to modulate the overall meta-devices and to realize tunable nanophotonic devices.⁴¹ Furthermore, various nanophotonic phenomena, enabled by the resonance or enhanced light confinement at nanoscale, strongly depend on surroundings, while chalcogenides may be introduced to modulate those nanoscale optical events.^{42–46} In addition, the emissivity of chalcogenide films increases obviously in IR region during the crystallization process, enabling active control of thermal radiation for thermal emitters and camouflage technology.^{47–50}

One thing should be noticed is that although TMOs and chalcogenides can both have phase transitions when temperature changes, there are many differences in their material

properties. For example, the property change of VO₂ (a typical TMO) across the phase transition is volatile, which means continuous power should be applied to keep the material at a constant temperature. On the other hand, phase transitions in GeSbTe alloy (a typical chalcogenide) are stimulated by pulsed heating and are nonvolatile, leading to no energy in need for material property maintaining. Comparison between properties of VO₂ and GeSbTe alloy is listed in Table 1.

Table 1. Differences between VO₂ and GeSbTe Alloy

	VO ₂ (a typical TMO)	GeSbTe alloy (a typical chalcogenide)
volatility	volatile	nonvolatile
phase transition scheme	background temperature driven	pulsed heating driven
energy consumption during phase transition	low	high
contrast	low	high
transition speed	sharp and fast	gradual and slow

In Figure 1, we have summarized the excitation, phase transition, and typical applications of TMOs and chalcogenides in electrical nanodevices, nanophotonics, and thermal radiation control. In last few decades, there are various literature reviews on recent advances of PCMs in nanophotonics,^{51,52} metasurfaces,^{41,53,54} nonvolatile memory,^{33,55–57} and neuromorphic devices.^{58,59} However, a comprehensive introduction from material physics and chemistry (particularly on emerging TMOs and chalcogenides) to their applications in nanodevices (including electronics, nanophotonics, and thermotics) is still lacking. In this review, we start by introducing the physics and mechanism of transition oxide and chalcogenide PCMs. Then its feasible applications are reviewed from the aspects of electrical nanodevices, wave manipulation in nanophotonics, and thermal radiation control. Benefiting from the dramatic change of physical properties during the process, we illustrate phase transition as the perfect method to build novel programmable and dynamic nanodevices. Finally, we discuss major obstacles in the current development of PCM-based nanotechnologies and provide our prospect of future developing trends.

2. MATERIALS PHYSICS AND CHEMISTRY OF PHASE TRANSITION

2.1. Introduction of Phase Transition

Phase transitions describe the process in which a crystal or electronic structure undergoes a change between two different states. This review is focused on structural phase transformations that lead to useful electrical, optical, and thermal property contrasts. Phase transitions occur when an initial phase is unstable relative to a second phase. For example, heating glassy silica above 1000 °C can result in crystalline quartz because quartz is more stable at 1000 °C than the disordered structure of glassy silica. Yet the opposite transition happens at 1715 °C when the disordered state of molten silica is thermodynamically more stable. Quenching molten silica at a higher rate than that of crystallization transform the material back to its glassy solid state. However, the glassy silica to quartz phase transformation results in a rather small change to the material's intrinsic electronic and optical properties, which may not be suitable for reprogrammable devices. In contrast, local structural changes in the common PCMs result in radical

changes to the refractive index and electrical conductivity, and it is these property changes that are now providing a new way to design programmable nanodevices.

The most well-studied PCMs were originally developed for data storage. Indeed, they were successfully commercialized by Panasonic for rewriteable compact and digital versatile discs. More recently, both Samsung and Intel have commercialized electronic memory devices that are based on the same family of PCMs, namely those along the Sb₂Te₃–GeTe pseudobinary compositional tie-line. Beyond data storage, the enormous property contrast exhibited by PCMs has been used to adjust the resonant frequency of optical metamaterial filters^{61–63} and microring waveguides;^{64,65} achieve homeostasis by controlling surface emissivity,⁶⁶ create low energy reflective displays,⁶⁷ perform arithmetic,⁶⁸ control the transmission of GHz, surface plasmon polariton (SPP), and optical waves,^{69–71} modulate surface phonons, and control the movement of micro-particles.^{72,73}

Many properties need to be considered when designing or selecting PCMs for nanodevices, such as contrasts of physical properties between two states, the minimum refractive index, optical loss at the operation wavelength, archive stability, switching speed, switching power and energy, fabrication precision, multilevel ability, and write–erase cyclability. Currently, no single PCM composition is well-suited to programming all conceivable nanodevices.⁷⁴ For example, Sb₂Te₃–GeTe PCMs are better suited to mid-infrared (MIR) photonics than near-infrared (NIR) and visible photonics because in the MIR they exhibit a large change in the real part of the refractive index with low absorption. These Sb₂Te₃–GeTe PCMs were originally designed for data storage where archival stability and high rates of crystallization are key considerations. But for many emerging photonics applications, such as off-line trained optical neural networks (ONNs) for feedforward inference operations, the PCM is used to program weights of the network, and the programming time and cyclability are unimportant because these devices are infrequently trained. In contrast, the multilevel ability, refractive index contrast, and low absorption are of greater concern. Currently, there are a handful of candidate PCM compositions that seem suitable for low-loss programmable photonics applications in the visible and NIR spectral bands. We believe that more effort from the photonics-materials community is required to design bespoke PCM for different applications.

Although most materials can exist in amorphous and crystalline states, for example, quartz and glassy silica are both made of silicon dioxide, only a small fraction of these materials exhibit physical properties that make them ideal for programmable photonics and data storage. An ideal PCM should have a large refractive index change between phases, be capable of reversible switching between phases, rapidly change phases with low input energy, and have phases that are stable under the typical operating conditions of the device. Clearly, the stability requirement is contradictory. For example, PCM needs to be stable at room temperature yet be unstable and change phase rapidly with moderate input energy. Such structural changes require atomic mobility to exhibit a highly nonlinear response to the input energy. We can see now why the phase transition between glassy silica and quartz is unsuitable for active photonics. The refractive index difference between silica and quartz is either 0.07 or 0.03, depending on the polarization of the light. Above the glass transition temperature, the melting temperature is 1710 °C, and SiO₂ is considered a strong liquid,

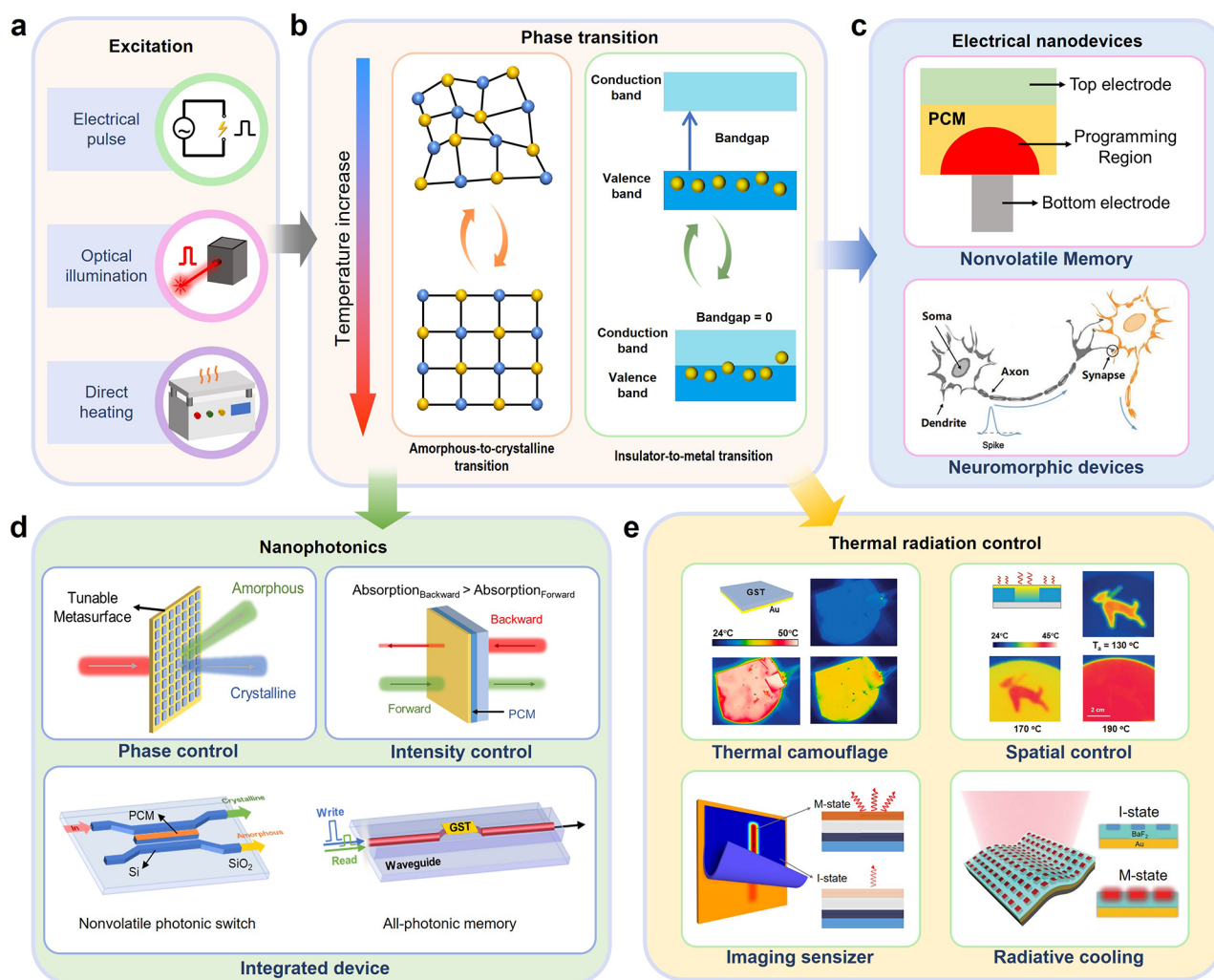


Figure 1. Excitation, phase transition, and typical applications of PCMs. (a) Excitation methods to stimulate phase transition, including electrical pulse (top), optical illumination (middle), and direct heating (bottom). (b) Two kinds of phase transitions which are discussed in this review: amorphous-to-crystalline transition (left) and insulator-to-metal transition (right). (c) Applications of PCMs on electrical nanodevices: NVM (top) and neuromorphic device (bottom).⁵⁸ The bottom panel is adapted with permission from ref 58. Copyright 2020 Wiley-VCH. (d) Applications of PCMs on nanophotonics and some typical examples including phase control (top left), intensity control (top right), and integrated device (bottom). (e) Applications of PCMs on thermal radiation control: thermal camouflage (top left),⁴⁷ spatial control (top right),⁶⁰ imaging sensitizer (bottom left),²⁹ and radiative cooling (bottom right).³¹ The top left panel is reproduced with permission from ref 47. Copyright 2018 The Author(s). The top right panel is reproduced with permission from ref 60. Copyright 2022 Wiley-VCH. The bottom left panel is reproduced with permission from ref 29. Copyright 2020 The authors. The bottom right panel is reproduced with permission from ref 31. Copyright 2021 The American Association for the Advancement of Science.

which means that the atomic mobilities do not show the abrupt changes that are necessary for amorphous PCMs to be stable at room temperature yet crystallize rapidly when heated above the glass transition temperature. In contrast to the silica-quartz phase transition, several binary and ternary chalcogenide PCMs and TMOs that can fulfill these requirements have been developed.

2.2. TMOs

2.2.1. Introduction of TMOs. TMOs are compounds formed by combining transition metals with oxygen atoms. Some of them, such as VO_2 ^{75–77} and MoO_3 ,^{78,79} show the peculiar property of the reversible MIT, at which the physical properties change dramatically, including their electrical resistivity, dielectric constant, transmittance/absorbance, and thermal emissivity. Among them, VO_2 is the most studied one and presents as a textbook of MIT materials.^{75–77}

In 1959, Morin pioneered the work of MIT VO_2 and demonstrated the reversible crystal structural transition at the critical temperature T_c of ~ 340 K (68 °C).¹² During the transition, the VO_2 changes from its high-temperature rutile (R) to low-temperature monoclinic (M) phase. The VO_2 (R) crystal shows a body-centered cubic structure with linear V–V chains of ~ 2.85 Å, which is lower than the critical V–V distance of ~ 2.94 Å, leading to the shared electrons in the d-orbital and the bulk metallic property (Figure 2a).⁸⁰ The VO_2 (M) displays a slightly distorted crystal structure made of zigzag V–V chains with two different chain lengths of ~ 2.65 and ~ 3.12 Å, resulting in the insulating property (Figure 2a).⁸⁰ In 1971, Goodenough first described the molecular band structures of VO_2 (R/M).⁸¹ The metallic VO_2 (R) has a partially overlapped π^* and d// bands, while the insulating VO_2 (M) has an elevated π^* band and a split d// band, leading to a band gap of ~ 0.7 eV (Figure 2b).

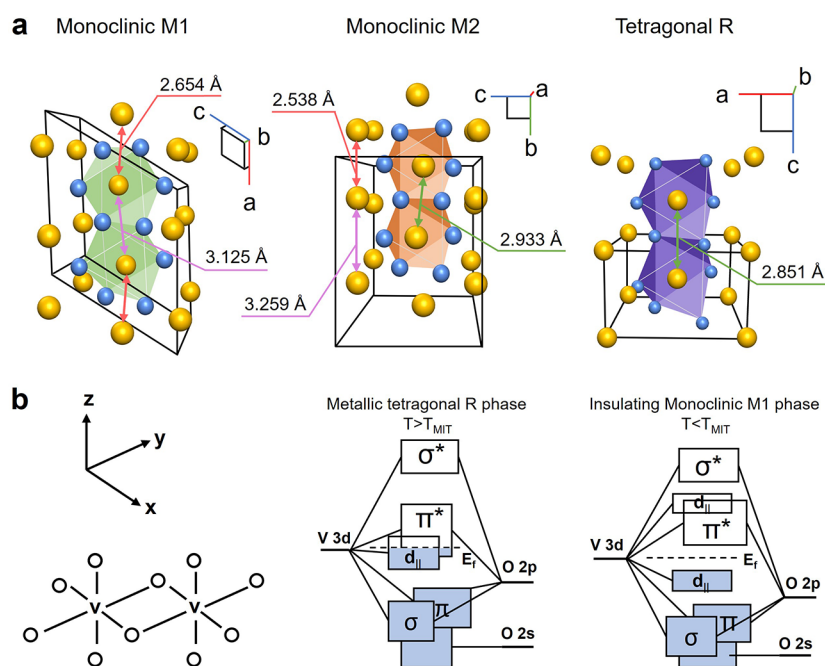


Figure 2. Crystal structure and band structure of VO₂. (a) Schematic crystal structures of insulating monoclinic (M1 and M2) and metallic tetragonal (rutile R) VO₂. The V atom and oxygen atoms are indicated as gold and blue spheres, respectively. The V–V distances are also indicated. (b) Schematic band structure of the VO₂ (M) and VO₂ (R).⁸⁰ Reproduced with permission from ref 80. Copyright 2011 American Chemical Society.

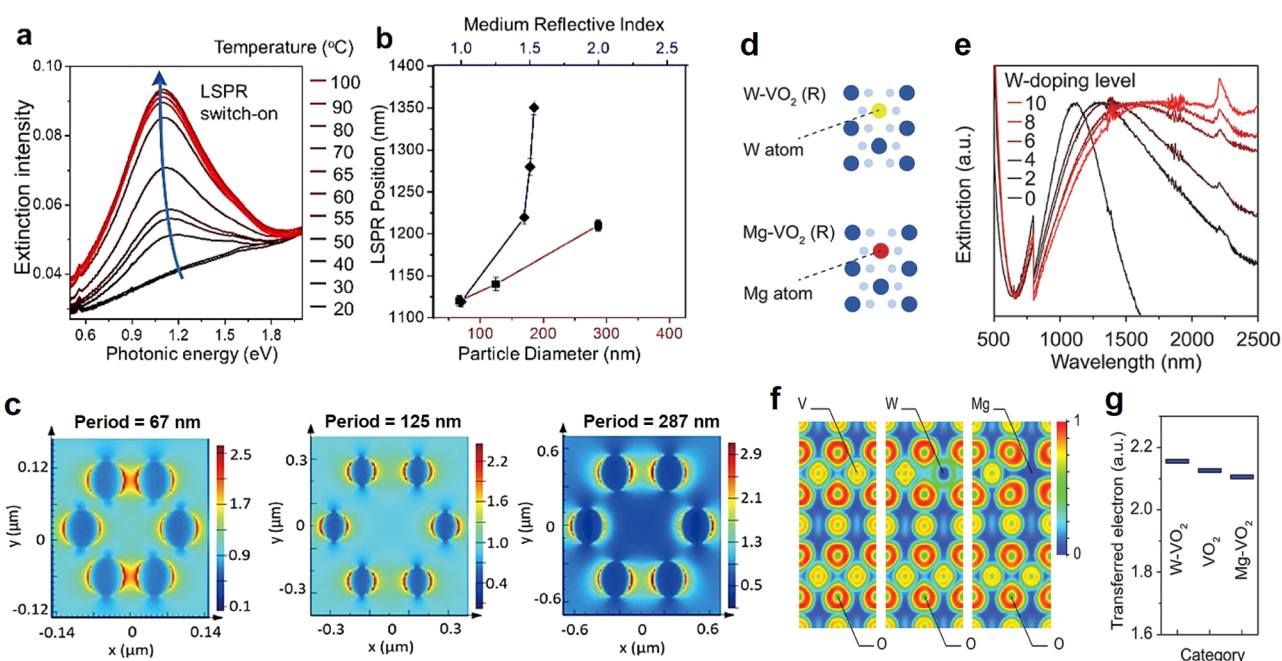


Figure 3. Modulation of LSPR in VO₂. (a) The "on-off LSPR" behavior in temperature-responsive VO₂(M/R). The LSPR intensity increases under elevated temperatures. (b) The effects of particle size and medium refractive index on the LSPR peak position. (c) Calculated electrical fields in the x - y plane of patterned VO₂ (R) nanoparticles with a periodicity of 67, 125, and 287 nm, respectively.⁹² Reproduced with permission from ref 92. Copyright 2017 American Chemical Society. (d) Illustration of the substitutional W and Mg dopant in VO₂ (R) crystal lattices. (e) Extinction spectra of VO₂ (R) nanoparticles with different W doping levels. (f) Calculated electron localization function (ELF) maps and (g) the total transferred electrons from V to O atoms of pristine VO₂, W-VO₂, and Mg-doped VO₂ (Mg-VO₂).⁹⁸ Reproduced with permission from ref 98. Copyright 2021 Royal Society of Chemistry.

The mechanism of VO₂ phase transition has been under debate for decades between the Peierls and the Mott–Hubbard models.^{82–86} The Peierls model describes the nature of the phase transition and suggests that the insulating is driven by the crystal structural distortion alone, while the Mott–Hubbard model suggests that strong electron–electron correlations are

involved in the transition, which contributes to the unusual phenomena, such as the ultralow conductivity.⁸⁷ Both of the two models have been strongly supported by experiments, and the debate remains by now.^{84–86} This may be attributed to the challenge in decoupling the electronic and structural portions

during the ultrafast transition, and the mechanism may differ when the transition is driven by different stimuli.⁸⁴

2.2.2. Properties of TMOs. The phase transition of metal oxides can be driven by many different stimuli, and the property change varies a lot from case to case.⁸⁴ Here, we concentrate on VO₂, as it is the most commonly used TMO in current tunable nanodevices. The VO₂ MIT was achieved by many methods that can be classified as thermal, magnetical, electrical, mechanical, optical, and electrochemical stimuli. Also, the transition leads to significant properties difference in electric, optical, thermal, and even mechanical properties. As a textbook material, VO₂ has been widely investigated in diverse devices and applications, and a detailed summary of VO₂ regarding its different stimuli-responsive transitions and the extensive applications can be referred to recent review works.^{84,86} On the basis of the range of its applications, we mainly focus on the property of nanophotonics and long-wave infrared (LWIR) thermal radiation.

The MIT transition leads to significant changes in its optical properties. One of the most investigated properties is its transmittance/absorbance modulation in visible-to-near-infrared (Vis-to-NIR) regions. The high-temperature metallic VO₂ shows a much lower NIR absorbance than the low-temperature insulating VO₂. The temperature-dependent transmittance characteristic makes it a promising material for energy-saving smart windows.^{85,88,89} So far, a lot of works have been reported to improve the modulation performance, including the methods by increasing the crystallinity, introducing dopants, tuning the nanoscale morphology, and so on, the detail of which can be referred to a more focusing summary work for VO₂ in smart window applications.^{85,90} In general, the VO₂-based smart window exhibits two merits: (1) the “passive” work mechanism by applying the temperature-dependent transmittance change, and (2) working in a “silence” way, where the visible change is negligible and indiscernible. One of the interesting nanophotonic works is to apply the VO₂-based photonic crystal to the smart window.⁹¹ Long’s group proposed a hexagonal-closed-packed monolayer structure consisting of VO₂-SiO₂ core-shell spheres and demonstrated the photonic bandgap in the visible region by tuning the diameter of the core-shell spheres from ~400–800 nm while maintaining the NIR modulation of VO₂.⁹¹ This method is effective to produce blue, green, and yellow glasses using the yellow-brown VO₂.

The surface plasmon resonance of VO₂ is interesting because it only appears on the metallic state but is being quenched on the insulating state. This active/dynamic characteristic makes VO₂ distinct from those classic plasmonic materials such as gold, silver, and aluminum. Ke et al. demonstrated active localized surface plasmon resonance (LSPR) on patterned VO₂ nanoparticles.⁹² The LSPR can be reversibly switched on by elevating the temperature to transit VO₂ from insulating to the metallic state while being entirely quenched at a lower temperature (Figure 3a). Also, the LSPR in VO₂ is affected by the local media reflective index,^{92,93} crystal sizes, and particle shapes (Figure 3b).^{92,94} Above the critical transition temperature, the nanoparticles exhibit a strong electrical field near their interfaces (Figure 3c). In their following work, they verified that the particle size and W dopants are effective to control the LSPR energy (Figure 3d,e), for example, the energy decreases to ~0.7 eV on the sample with a W doping level of 10 at. %. They also pointed out that there is less electron transfer from W to its neighboring O atoms (Figure 3f) and suggested that the effect of the charge of cations (Barder charge transfer) plays a dominant

role over a number of valence electrons to determine the free carrier density (Figure 3g).

The emissivity change of VO₂ during phase transition has witnessed increased attentions recently. A VO₂ thin film decreases its emissivity in the LWIR region with changes from its insulating to metallic states.⁹⁵ This property was applied for thermal camouflage in early reports.⁹⁶ Quite recently, two groups applied the material to building envelopes by constructing Fabry–Perot resonator structures for enhancement of the emissivity change to meet the energy-saving demands.^{31,97} Wu’s group reported the sample constructed of patterned W-VO₂ in BaF₂ film with an Ag-based back reflectance layer.³¹ The sample shows a low emissivity ~0.2 on low temperature and a high emissivity ~0.9 on high temperature with a low absorptance in the solar spectrum, which is able for building roofs. Long’s group reported applying the switchable emissivity of VO₂ in smart window applications.⁹⁷ In their work, the sample has a multilayer structure consisting of VO₂, poly(methyl methacrylate) (PMMA), indium tin oxide (ITO), glass, and ITO in sequence. Besides the switchable emissivity in the LWIR region, their sample is also transparent in solar spectra and can be dynamically modulated in NIR, while maintaining a nearly constant transmittance in the visible range.

2.2.3. Modulation of T_{MIT}. Modulating the phase transition of VO₂ has been attracted long-standing research interest. One of the most efficient methods is to introduce the substitutional dopants, such as W, Mg, and so on.⁸⁵ Most of these methods target to reduce its intrinsic critical temperature of ~68 °C to near room temperature, thus making it more suitable for some applications such as temperature-independent camouflage, TIS, which will be discussed in section 5. To our knowledge, the W doping is the most efficient and the most widely used method to reduce the critical transition temperature by ~15–30 °C/at. %.⁸⁵ Reza’s group observed the W dopants in insulating VO₂ nanowire generate anisotropic localized stress⁹⁹ while introducing more uniform stress distraction in metallic VO₂. They further proved that this lattice-stress difference gives an energetic consequence of structural distortion and transition.

Different from substitutional dopants, interstitial dopants such as H atoms can tune the VO₂ from insulating to metallic phases without destroying its lattice framework.¹⁰⁰ Son’s group achieved the reversibly H intercalation by depositing Pt on VO₂ surface as catalysis.¹⁰¹ The H atom, known as the smallest and lightest atom, can stay on the interstitial sites in VO₂ lattice to form metallic H_xVO₂ by filling the interinteger *d*-band.

Besides, lattice strain/stress can also be generated by the interfacial lattice mismatch in epitaxial films. Muraoka et al. grew VO₂ thin film on TiO₂ (001) and (110) surface and found out the epitaxial stress can compress and expand the VO₂ along *x*-axis, leading to a tunable critical temperature.¹⁰² In detail, the critical transition temperature decreases significantly from 341 to 300 K for VO₂ grown on TiO₂ (001) and increases to 369 K for VO₂ on TiO₂ (110). The effect is also thickness dependent and becomes less obvious for thick epitaxial VO₂ film due to the stress relaxation effect alone out-of-plane directions.^{103,104} Wu’s group modulated the phase transition by applying the strain onto a single VO₂ nanowire directly, and they plotted a phase diagram of VO₂ by considering both the strain and temperature effects.¹⁰⁵

2.2.4. Fabrication Technologies. So far, plentiful technologies have been developed for VO₂ syntheses, such as hydrothermal method, vapor deposition, template-/mode-

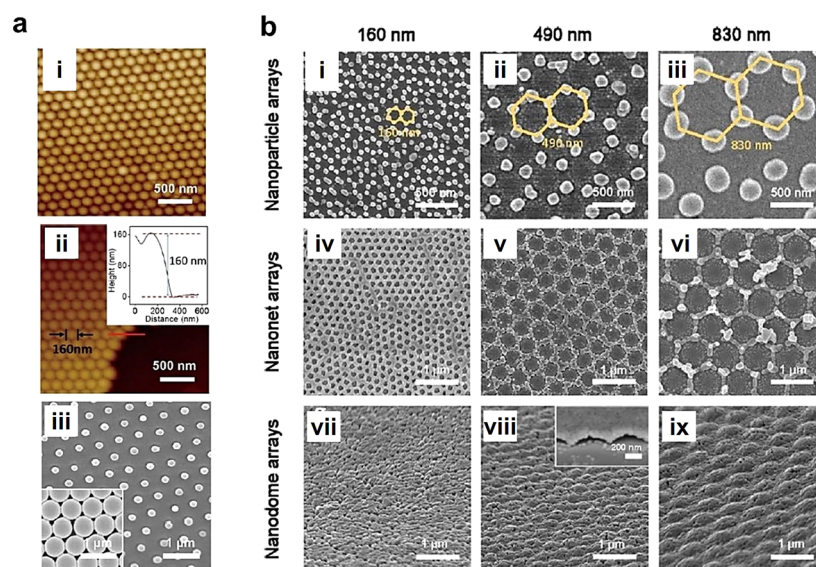


Figure 4. VO₂ polycrystals fabricated by the template-/mode-assisted method. (a) Monolayer colloidal templates consisted of polystyrene spheres. Atomic force microscope (AFM) topographic images of the monolayer colloidal templates on its surface (i) and edge (ii). Inset of (ii): the high analysis on edge. (iii) Scanning electron microscope (SEM) images of the colloidal templates before (inserted figure) and after the O-plasma treatment. (b) SEM images of produced VO₂ (M/R) crystals. The samples are produced with hexagonal nanoparticles (i–iii), nanonet (iv–vi), and nanodome arrays (vii–ix) with tunable periodicity from 160, 490, to 830 nm. Inset of (viii): the tiled view to illustrate the hollow dome structure.⁹² Reproduced with permission from ref 92. Copyright 2017 American Chemical Society.

assisted replication, and so on. In general, VO₂ (M/R) tends to grow alone on its *c*-axis, resulting in rod and wires structures.

The hydrothermal method has been used to develop VO₂ crystals with different sizes, shapes, and dopants. The summary of hydrothermal synthesis of VO₂ can be referred to other focusing review work.¹⁰⁶ Doped VO₂ is achievable by adding dopants elements (e.g., W, Mg, F, Fe) in precursors, and a more complex structure can be realized through post-treatment. For example, the group of Gao and Luo has successfully produced core/shell W-VO₂/TiO₂ nanorods.¹⁰⁷ In their process, the V and W precursors are mixed in an autoclave and undergo 260 °C for 48 h to produce the W-VO₂ nanorods. The TiO₂ shell is prepared by mixing the produced W-VO₂ crystals in Ti solution precursor and the TiO₂ shell forms during an 80 °C hydrolysis process. Furthermore, vapor deposition is widely applied for the fundamental study of VO₂ properties as the product usually comes with very high crystallinity with a rod morphology with dimensions from several hundred nanometers to micro-scale.^{87,108–110} The epitaxial growth method can obtain high-quality VO₂ thin film with a controllable thickness in sub-100 nm, although high-quality substrates are usually required.^{101,104,111,112} Besides, the template-/mode-assisted method is appropriate to prepare VO₂ polycrystals in sub-100 nm scale with controllable size, shape, and composition (Figure 4).^{92,98}

Despite the sufficiency of preparation methods for VO₂(M/R), it is still challenging to prepare high-quality VO₂(M/R) in sub-50 nm with well-controlled size and shapes. One reason is that the V element shows many valences (e.g., V⁺³, V⁺⁴, and V⁺⁵), and the vanadium oxide can exist in different forms, such as V₂O₃, VO₂(M/R), VO₂(B), V₂O₅, and so on. Another reason is that the synthesis requirement of VO₂(M/R) is harsh, which commonly requires a high-temperature process.

2.3. Chalcogenide PCMs

2.3.1. Introduction of Chalcogenides. Because of its remarkable change of refractive index and thermal emissivity

during phase transition, TMOs have been widely applied in many fields including meta-canvas,²⁵ IR camouflage,⁹⁶ TIS,²⁹ encryption,¹¹³ smart windows,^{85,90} and much more. However, a disadvantage of TMO-based devices is that the material must be heated continuously to maintain the desired property. Contrarily, phase change chalcogenides can latch into metastable amorphous or crystalline phases without a continuous supply of heat. This nonvolatile property has led to many new programmable nanodevices.

Chalcogenides are materials composed predominantly of either sulfur, selenium, or tellurium. These elements belong to group 6 of the periodic table. Many chalcogenides crystallize at temperatures sufficiently high that their amorphous state is relatively stable at room temperature, yet the crystallization temperature is sufficiently low that it can be accessed using a focused laser diode irradiation or electrical Joule heating. This means that both the amorphous and crystalline states can be stable at room temperatures. When many tellurium-based materials crystallize, their physical properties undergo a pronounced change where electrical conductivity and low-frequency refractive index increase. It is these alterations that are now being exploited in programmable displays, metamaterials, on-chip photonics, nonvolatile memories, and so on.

Chalcogenides can exist naturally as minerals; two of the most well-known being FeS₂ (pyrite) and AuTe₂. In fact, AuTe₂ was the main reason for the goldrush town in Southwest Colorado being named “Telluride”. One can, therefore, understand from an etymological perspective that the word chalcogenide is derived from the Greek for “ore former”,¹¹⁴ a word that has existed in the scientific literature since the early 1930s.¹¹⁵ Historically, oxide materials are the oldest known glass-forming systems, especially in silica; it has thus become a tradition to treat them separately from more recently discovered chalcogenide compounds. Scientifically, oxide materials behave rather differently from other chalcogenides. For example, the band gap energy of SiO₂ is approximately 10 eV and therefore it is

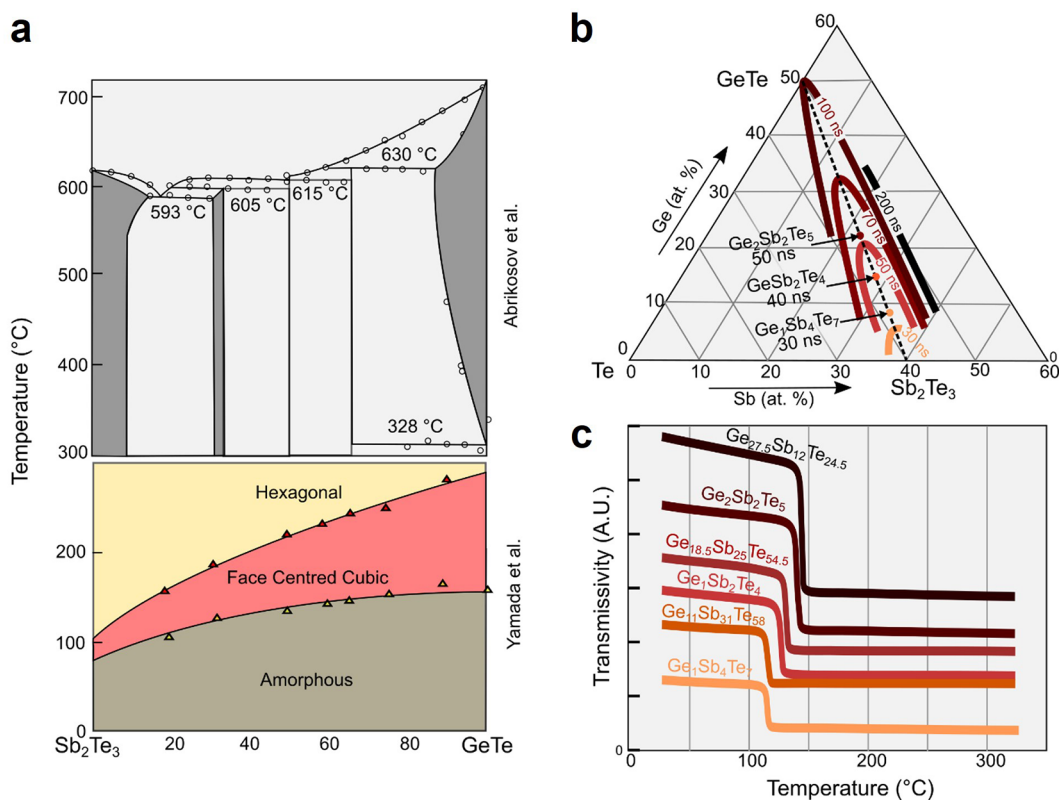


Figure 5. Properties of GeTe–Sb₂Te₃ alloy. (a) The phase diagram for the GeTe–Sb₂Te₃ pseudobinary (top panel) and the associated crystallization temperatures (bottom panel). (b) Crystallization times of ternary amorphous thin films around the GeTe–Sb₂Te₃ pseudobinary tie-line. (c) Transmissivity changes when different GeTe–Sb₂Te₃ compositions are heated at a constant rate of 10 deg/min.¹⁸ Reproduced with permission from ref 18. Copyright 1991 American Institute of Physics.

insulating, yet many chalcogenides have band-gaps below 3 eV and are, therefore, semiconducting.¹¹⁶

N. A. Goryunova and B. T. Kolomiets' seminal work on the semiconducting properties of amorphous chalcogenides initiated a new field in amorphous semiconductor solid-state physics.¹¹⁷ Ultimately, this field led to Stanford Ovshinsky discovering that many telluride materials exhibit threshold switching, a field-driven effect in the amorphous state of chalcogenides where a substantial current flows that can cause Joule heating and a subsequent amorphous to crystalline phase transition.¹¹⁸ This was the start of the phase change chalcogenides era. Since then, chalcogenide phase transitions have been successfully commercialized for both optical and electrical data storage,^{15,119} and now their programmable properties seem well suited to new forms of computing^{35,120} and programmable photonics.^{51,52,121}

2.3.2. The Physical Origin of Amorphous-to-Crystalline Phase Transition. Alloys along the GeTe–Sb₂Te₃ pseudobinary tie-line tend to fulfill many of the specifications required for high-speed programmable devices, including high crystallization rates, enormous property contrast, and non-volatility. These phase change alloys are among the most well-studied PCMs because they were originally developed and commercialized for data storage.¹⁵ The Sb₂Te₃ and GeTe binaries have also been grown as layers within phase change superlattices¹²² and SLL structures,¹²³ which exhibit lower switching energies than their alloy counterparts. The attractive properties of these materials have recently fueled an explosion of interest in Sb₂Te₃–GeTe alloys with researchers and engineers reimagining their application in reprogrammable photonics and

thermotics. For this reason, we discuss the physical origin of their properties in some details in the following paragraphs.

In 1990, the Ge₂Sb₂Te₅ (GST) ternary compound was first commercialized by Matsushita Electrical (Panasonic Corporation) for optical memory applications.¹²⁴ GeTe was chosen because it has a high optical contrast between amorphous and crystalline states, which is needed to accurately read data from an optical disc. However, the crystallization speed of as-deposited GeTe is relatively slow. In contrast, Sb₂Te₃ was known to crystallize rapidly. It was hypothesized, therefore, that alloying Sb₂Te₃ with GeTe may enable high crystallization rates and high optical contrast, an ideal combination for optical data storage.¹⁸ The phase diagram for the GeTe–Sb₂Te₃ system was first published by Abrikosov and Danilova-Dobryakova in 1965 (Figure 5a).¹⁸ The phase diagram exhibits a relative flat melting temperature at 611 ± 19 °C across a wide compositional change from ~20% GeTe to ~84% GeTe. Ternary compounds exist along with the phase diagram by periodically stacking GeTe and Sb₂Te₃ in hexagonal unit cells with a face-centered cubic (FCC) stacking rule.¹²⁴ These compounds have two prominent crystallization events. At lower temperatures, the amorphous material first crystallizes into an FCC structure, and then at a higher temperature, the FCC structure transforms into a stable hexagonal crystal. This is clearly seen in the lower panel of Figure 5a, which shows the amorphous → FCC and FCC → hexagonal crystallization temperatures as a function of composition. Note, the reversible amorphous ↔ FCC transition is normally used for data storage. The optical, electrical, and phase change performance of GeTe–Sb₂Te₃ alloys can be tuned by the GeTe:Sb₂Te₃ ratio. The hypothesis that allowing GeTe with

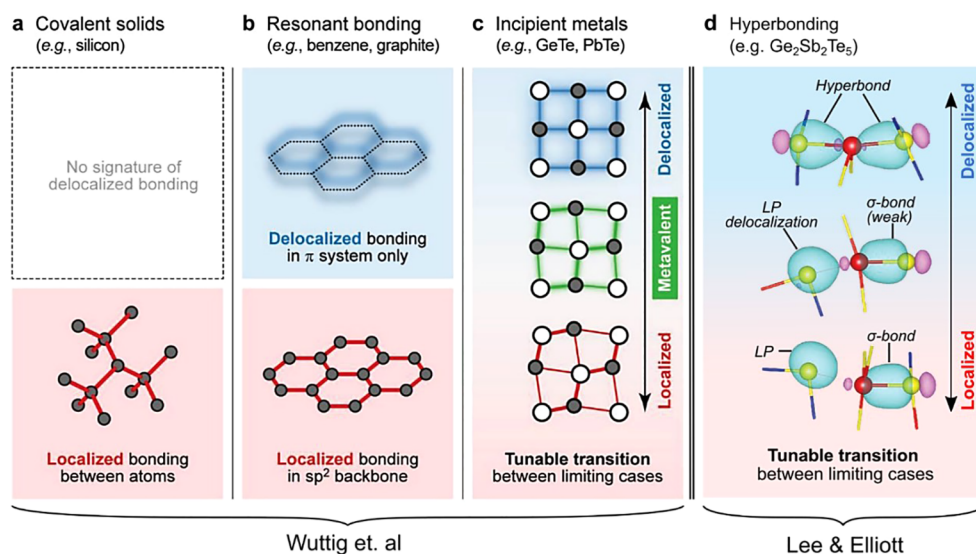


Figure 6. Delocalized bonding models from Wuttig et al. and Lee and Elliott. (a) Covalent solids show localized bonding without any enhancement to their optical matrix elements. (b) Resonant bonding exists in benzene and graphene with p_z orbitals out of the plane of the sp^2 backbone. (c) Metavalent bonding has been proposed by Wuttig et al. Here, the delocalization occurs along p -orbitals across the multiple crystallographic unit cells. Intermediate electronic and optical properties are suggested to occur when the backbone undergoes small structural changes, thus making the properties of the material tunable.¹³¹ Reproduced with permission from ref 131. Copyright 2018 RWTH Aachen University. (d) Hyperbonding (lone-pair antibonding orbital) model was proposed by Lee and Elliott. The most delocalized arrangement shows a hyperbond pair. The intermediate configuration exhibits a nontrivial interaction between a LP orbital and the antibonding orbital of a bonding pair. It is suggested that the relative proportion of these different three center four electron ($3c/4e$) different interactions within a PCM will radically change its macroscopic properties.¹³² Reproduced with permission from ref 132. Copyright 2020 The Authors.

Sb_2Te_3 would produce a ternary compound that crystallized quickly and exhibited a large optical contrast was correct. In 1991, Yamada et al. showed this in their seminal paper on the application of $GeTe-Sb_2Te_3$ for data storage. It has been shown that the optical transmission contrast increases with the $GeTe$ concentration, while the crystallization time decreases with the Sb_2Te_3 concentration (Figure 5b). Later, $GeTe$ was found to recrystallize from its melt-quenched state much faster than crystallization of the as-deposited amorphous material.^{18,125} This difference is due to the reamorphized state retaining crystal nuclei; hence the melt-quenched amorphous state does not need time to nucleate a crystal.

To understand the physical properties of Sb_2Te_3-GeTe alloys, we must first discuss their crystal and electronic structures. Matsunaga and Yamada used X-ray diffraction studies to show that the FCC phase of the Sb_2Te_3-GeTe alloys is important for data storage. The FCC phase of GST, which is the most commonly studied PCM due to its commercial success in digital video disk (DVD)—random access memory (RAM)¹²⁴ and electronic memory,¹¹⁹ is constructed of two sublattices, with Te atoms occupying one sublattice and a mixture of Sb , Ge , and vacancies occupying the other.¹⁸ Robertson proposed that bonding in $GeTe$ can be resonant covalent if the bond lengths are similar.¹²⁶ Note, however, that $GeTe$ is a ferroelectric crystal with three short and three longer $GeTe$ bonds, but when this material is alloyed with Sb_2Te_3 , the $Ge-Te$ and $Sb-Te$ bond lengths become more similar, and it was supposed that resonant bonding is possible.

Resonant bonding can explain the large refractive index of the crystalline Sb_2Te_3-GeTe alloys.¹²⁷ The electrons in a resonantly bonded crystal are delocalized along the p -orbital bonds across multiple unit cells. Delocalized electrons are easily polarized by an external electric field, and polarizability is directly connected to the dielectric permittivity via the

Clausius–Mossotti relation. Therefore, explaining the unusually large dielectric permittivity of Sb_2Te_3-GeTe PCMs being due to resonant bonding is reasonable.¹²⁷

There are distinct differences in the short-range order between crystalline and amorphous Sb_2Te_3-GeTe alloys. Indeed, Kolobov et al. used extended X-ray absorption fine structure (EXAFS) spectroscopy to show that Ge atoms are predominantly 6-fold coordinated with the FCC crystalline phase in FCC GST yet in the amorphous state occupy a mixture of tetrahedral, pyramidal, and defective octahedral sites.¹²⁸ This difference in local structure is important because valence electron delocalization, which enhances the dielectric permittivity, requires the p -orbitals to align across neighboring bonds, and any disruption to this alignment will lower the dielectric permittivity.^{129,130} Thus, a simple model emerges to describe how the optical properties of GST depend on the local structure. That is, the local structural transition of Ge atoms from predominantly octahedral sites to a mixture of pyramidal, tetrahedral, and defective octahedral sites disrupts electron delocalization and its concomitant molecular polarizability, and this causes a radical decrease in the GST refractive index.

Although the description of resonant bonding in GST provides a neat way to describe the property contrast in the Sb_2Te_3-GeTe system, this form of bonding is not the same as the textbook resonant bonds that are observed in graphene and benzene. For example, the carbon atoms in graphene are bound together by a strong covalent sp^2 backbone with p_z orbitals pointing out of the two-dimensional (2D) surface and delocalized across it. These p_z orbitals do not interact with the sp^2 backbone (Figure 6b). In contrast, $GeTe-Sb_2Te_3$ crystals tend to share delocalized p -orbital electrons along the structure's backbone, and consequently, small changes in the backbone structure produce radical changes to the macroscopic properties of the $GeTe-Sb_2Te_3$ PCMs. Wuttig et al. introduced the

concept of metavalent bonding (MVB), which is a whole new bonding category, to distinguish this different bonding behavior from resonant bonding.¹³¹ It has been noted that the atomic coordination number and electronic conductivity of MVB materials take intermediate values between covalent and metallic solids and have a substantial anharmonic lattice instability. Therefore, it is suggested that the properties resulting from the metavalent bond can be tuned by the degree of electron sharing along the p-orbitals. Elliott and Lee, however, explain this tunability as not being a property of the bond itself, rather the result of mixing different bonding types. This mixture can result in a distribution of bonds with cubic GST exhibiting a subset of the bonds that are also present in amorphous GST. The argument for this assertion is based on bond character; the bond character in cubic GST overlaps with bond characters seen in amorphous GST. From an atomistic perspective, the interatomic bond distances in cubic GST are on average longer than those in amorphous GST. Moreover, the bond-length distribution indicates that axial bonds are dominant in cubic GST. Axial bonds can form three center/four electron (3c/4e) hyperbonds, which exhibit stronger electron delocalization than two center/two electron (2c/2e) covalent bonds, thus explaining the large dielectric permittivity seen in cubic GST. Moreover, hyperbonding can also explain the reason that 6-fold coordinated atoms are possible in both cubic and amorphous GST using three p-orbitals and simultaneously allowing 5- and 6-fold coordinated Ge and Sb atoms in amorphous GST. Parts c and d of Figure 6 compares the model proposed for delocalization by Wuttig et al.¹³¹ with that proposed by Lee and Elliott.¹³² Although these two viewpoints are somewhat different, they both agree that bonding in the Sb_2Te_3 -GeTe alloys is not the same as resonant bonding in graphite and benzene, and they also agree that there is substantial valence electron delocalization, which radically increases the dielectric permittivity when amorphous Sb_2Te_3 -GeTe alloys crystallize. It is worth noting that Sb_2Te_3 is a topological insulator, and the interplay between spin-orbit coupling and the crystalline electric field further seems to further enhance the dielectric permittivity.¹³³ The valence-electron delocalization-dependent permittivity change is essential in programmable electronic and photonics devices. Therefore, throughout this review, we refer to bonding in the crystalline phase of the GeTe- Sb_2Te_3 alloys as “delocalized-bonding”, rather than resonant, metavalent, or hyperbonding because it encompasses all these possibilities.

The Sb_2Te_3 -GeTe alloys have one major drawback for photonics: they strongly absorb light in the visible and NIR spectrum due to interband electronic transitions. Although the bandgap can be tuned by changing the relative ratio of Sb_2Te_3 to GeTe,¹³⁴ they seem suboptimal for visible and NIR photonics applications. For this reason, Sb_2S_3 , $\text{Ge}_2\text{Sb}_2\text{Se}_4\text{Te}_1$ (GSST), and Sb_2Se_3 have been proposed.¹³⁵⁻¹³⁷ All of these compositions have a wider bandgap than GST, with Sb_2S_3 having the largest bandgap and is consequently transparent to the red end of the visible spectrum. The refractive index change of these materials is large and sufficient to tune resonant photonic devices. The switching times tend to be longer than GST, and further work needs to be done to understand and then optimize the switching mechanism. Nonetheless, recent studies on the switching cyclability of Sb_2S_3 show the potential of designing nonvolatile photonic devices with cyclable optical states.¹³⁸

Different PCMs are needed to meet the programming requirements for specific applications. Typically, the properties of a chalcogenide PCM are controlled through doping and

alloying with other PCMs, which can tailor their properties for the application. For example, if phase change memories are employed in automobile engine microcontrollers, they must operate at high temperatures and the RESET (amorphous) state of the PCM must be stable against spontaneous crystallization. Because crystal nucleation is a stochastic process, controlling the nucleation process can increase the programming speed and repeatability.^{139,140} Indeed, the inference accuracy of emerging phase change neural network devices depends on the accuracy to which multibit interconnection weights can be stably programmed. For this reason, Sb_2Te_3 - TiTe_2 heterostructures have been designed whereby the Sb_2Te_3 layers act as a consistent seed from which the TiTe_2 layers can be switched with a high degree of repeatability, thus increasing the multibit programming repeatability.¹³⁹ Therefore, doped-GeTe, with its higher crystallization temperature, has been proposed for automobile applications.

2.3.3. Stimulation Technologies of Chalcogenides.

Phase transitions are driven by thermodynamics. For a material to change phase in a nonvolatile manner, it should lower its enthalpy. The simple picture of crystallization in the GeTe- Sb_2Te_3 alloys is based on thermally induced atomic relaxations into a lower energy crystalline phase. The atoms should be given sufficient thermal energy to overcome an activation energy barrier. For GST crystallization tends to happen between 420 and 650 K, depending on the heating rate.¹⁴¹ Amorphization, on the other hand, is rather different. In this case, the crystal should melt and then be quenched into the amorphous phase. Quenching is necessary because amorphous GST is higher in enthalpy than the crystalline phase and the atoms should not be given time to relax, otherwise, they will move back into their thermodynamically metastable crystalline structure. The local structure of molten GST is characterized by shorter bond distances¹⁴² and a prevalence of 4-fold coordinated Ge atoms.¹⁴³ However, the energetically more favorable cubic GST alloy is characterized by 6-fold coordinated atoms. This means the free energy of the crystal and amorphous structures must cross at a temperature close to the melting point such that the amorphous structure becomes more energetically favorable. Amorphization involves locking atoms into lower coordination by removing energy from the structure at a sufficient rate to prevent them from moving back into their lower energy 6-fold coordination sites. For GST, the quench rate needs to be $\sim 10^{10}$ K/s.¹⁸ The phase stability also depends on pressure, which can slow recrystallization.¹⁴⁴ Indeed, phase change compositions that do not exhibit a change in volume during the phase transition require less energy to switch because no work is done on the surrounding structures.¹⁴⁵ Finally, limiting configurational entropy change during a phase transition can be used to substantially increase phase transition efficiency. If one considers that GST consists of a spectrum of different atomic configurations^{128,132} or microstates, then limiting the number of microstates that can exist will increase the efficiency of the phase transition. This can be achieved using interfacial phase-change memories (iPCMs),¹²² which will be discussed in section 3.

Chalcogenides phase transitions depend not only on temperature but also the heating and cooling rates. These effects are most visible if one measures the crystallization temperature of GST. At relatively low heating rates, such as 50 K/s, GST crystallizes at 452 K with high activation energy, but at 40 000 K/s, the crystallization temperature increases to 625 K with a much lower activation energy.¹⁴¹ This activation energy lowering at high heating rates allows amorphous GST to

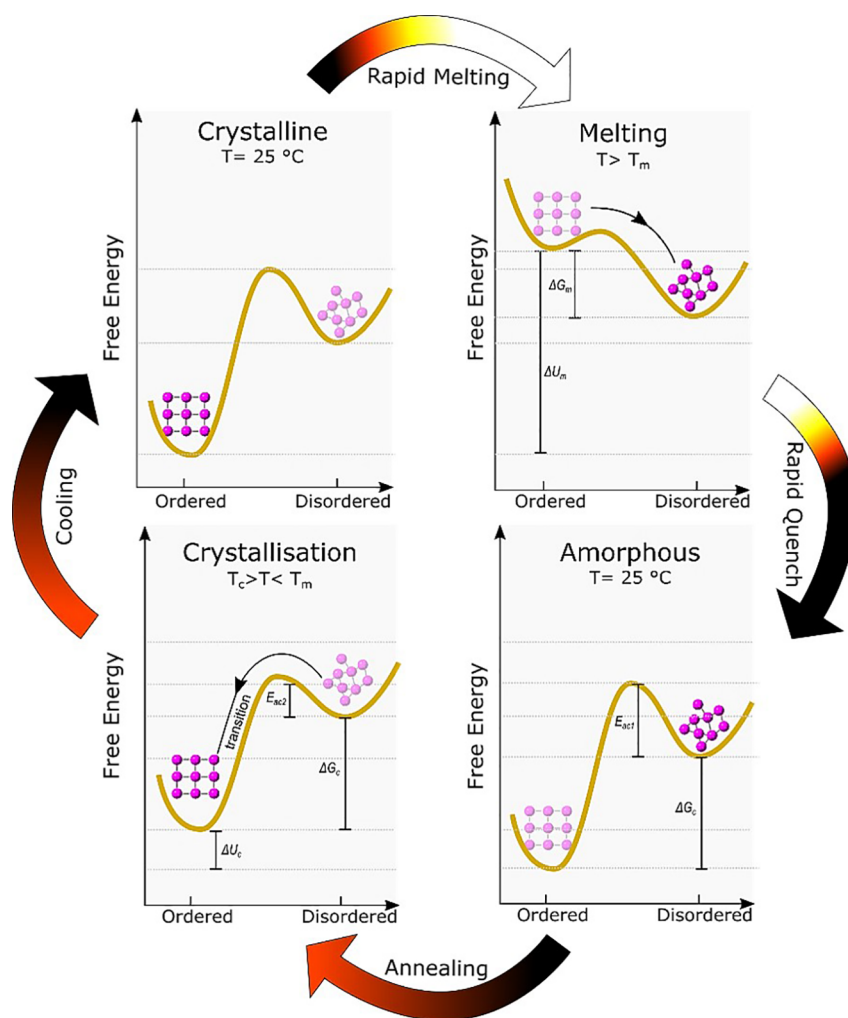


Figure 7. Changes in the potential landscape due to quenching and annealing Sb_2Te_3 – GeTe PCM. At room temperature, the PCMs lowest energy state is crystalline. However, heating the material to its melting point raises the energy of the crystalline structure, ΔU_m , disproportionately to the amorphous state, and the disordered state becomes more stable, thus melting and disordering occur. At room temperature, the amorphous state is at a local minimum in the potential landscape. It is only possible to access this state under out-of-equilibrium conditions; e.g., rapid quenching. If the quenching rate is sufficiently high and the atoms lose energy sufficiently quickly, then they can be trapped in a disordered state, which is higher in potential and therefore less thermodynamically stable than the crystalline state. The material is stable because a potential barrier, E_{ac1} , prevents the material from spontaneously decaying at room temperature. However, heating the material above the crystallization temperature, T_c , raises the crystal's free energy ($\Delta U_c - T\Delta S$) by ΔF_c and modifies the potential landscape by lowering the activation energy to E_{ac2} . For GST, $E_{ac2} = 2.3$ eV when the crystallization occurs at approximately 150 °C,¹⁴⁶ but if crystallization occurs at much higher temperatures due to high heating rates, then the activation energy can be lower.¹⁴¹

crystallize in nanoseconds when heated to a high temperature with short heat pulses but be stable for years at room temperature. The amorphous phase is usually accessed by heating the material to its melting temperature and then quenching the atoms into a somewhat disordered structural state. The power of the heat pulse used for amorphization is greater than that needed for crystallization because melting happens at a still higher temperature and because melting is an endothermic phase transition. Generally, the heat pulses used for amorphization are shorter than those used for crystallization because often only bond angles and distances need to change to invoke a change in the material's optical properties, i.e., diffusion of atomic species is not necessary. Moreover, longer-duration heat pulses cause heat to diffuse into the PCM surroundings, which concomitantly decreases the quench rate. For amorphization, the quench time must be shorter than the PCM's shortest crystallization time. Thus, short heat pulses, which do not substantially increase the thermal mass and associated quench

rate, are generally used for amorphization. In contrast, a longer heat pulse with lower heat power should be applied to recrystallize the PCM.

Phase transitions occur to lower the free energy of the material, and this fact is the key to understanding both melting and crystallization in PCMs. It is informative to consider the potential landscape when considering phase transitions. Figure 7 illustrates how the potential landscape changes when a typical data storage PCM, such as GST, undergoes a write \leftrightarrow erase (RESET \leftrightarrow SET) phase transition. The free energy is lower for the ordered (crystalline) state than the disordered (amorphous) state at room temperature. However, the potential landscape changes when the crystal is heated and at the melting temperature the free energy of the disordered state is lowered by entropy ($-T\Delta S$) to the point that the disordered state becomes more stable than the crystalline state, and therefore the crystal melts. The material must be quenched at a rate higher than that required for recrystallization in order to lock in the

disordered structure and form the amorphous phase. For example, GST must be quenched from 900 K to <300 K within 50 ns to prevent recrystallization. The amorphous phase is then stabilized by activation energy, E_{ac1} , which for GST is 2.3 eV.¹⁴⁶ This energy is equivalent to a temperature of 27 000 K, and therefore it would seem almost impossible for GST to crystallize in a few 10 s of nanoseconds at temperatures between 450 and 700 K. However, at elevated temperatures the crystallization activation energy for GST decreases to (E_{ac2}). This new activation energy is enforced because the crystallization temperature increases dramatically with the heating rate s , and this allows GST to crystallize quickly at high temperatures. As the temperature is lowered, the ordered crystalline phase is stabilized relative to the amorphous phase by high activation energy and a substantially lower free energy. The write \leftrightarrow erase (RESET \leftrightarrow SET) cycle is complete.

Heating the chalcogenide PCMs is generally achieved by either (1) irradiating with a laser pulse at a wavelength that is absorbed by the PCM, (2) passing a current through the PCM such that Joule heating is possible, and (3) passing a current through a resistive filament that is in contact with the PCM. The electrical, optical, chemical (diffusion and reactions), and thermal performance of the device materials need to be holistically designed to ensure efficient switching. For example, surrounding the PCM with a low thermally conductive material will reduce the heat input power required to melt the PCM, hence lowering the input power needed to melt the material. However, surrounding the PCM with a low thermal conductivity material lowers the quench rate, which makes amorphization difficult. In electrical devices, the metals of the electrodes tend to have a relatively high thermal conductivity, hence only small filamentary electrodes are used that tend to minimize the heat conduction. Or, in line cells, the PCM can be patterned as a dumbbell shape such that the current density and heating are highest in only the narrowest area of the cell.¹⁴⁷ Because chalcogenide PCMs tend to have a low thermal conductivity, the electrode interface remains cool. In optical data storage, ZnS-SiO₂ is often used as a thermal buffer to insulate the PCM from the Al reflector layers. The thickness of the ZnS-SiO₂ can be set to optimize heating and quenching rates. The thermal properties of one-dimensional (1D) and 2D materials also present interesting opportunities to design phase-change devices that can switch with extraordinarily low energies. For example, single-walled carbon nanotube (CNT) electrodes, graphene, and transition metal dichalcogenides (TMDCs) have all been used to substantially improve the efficiency of GST electrical PC devices.^{148–150}

To model electrical and optical responses of PCMs during a phase transition, thermodynamics and crystallization kinetics need to be considered. First, the model should describe the crystal microstructure evolution and then calculate the concomitant optical or electrical properties. Multiphysics phase-field¹⁵¹ and an open-source cellular automata model have recently been developed for this purpose.¹⁵² The cellular automata model, in particular, not only accurately predicts the optical response of the microstructure and optical properties of the polycrystalline and amorphized states of GST but also intermediate states, which is important for developing devices with a multilevel optical response.

2.3.4. Fabrication of Chalcogenides. Phase change chalcogenides are usually sputter deposited onto photonic devices. Although many tellurides can be sputtered using a direct current (DC) power supply, generally radio frequency

sputtering is preferred because chalcogenide sputtering targets tend to have high electrical resistance. Certain chalcogenides, such as Sb₂S₃, have a very high sputtering rate, and the power supplied to the target needs to be relatively low to control the final film thickness. The main problem with sputtering is that the coatings are not conformal, and therefore it is challenging to fill high aspect ratio vias. For this reason, atomic layer deposition (ALD),¹⁵³ chemical vapor deposition (CVD),¹⁵⁴ and electrodeposition¹⁵⁵ techniques have been developed. Although these techniques can fill high aspect ratio holes, they require complicated precursor materials that often contaminate the deposited film. For example, ALD-grown GST films tend to be contaminated with oxygen, hydrogen, and carbon impurities,¹⁵³ which can affect the phase transformation behavior.¹⁵⁶

The GeTe–Sb₂Te₃ superlattices and the Sb₂Te₃-based topological insulators have not properly been exploited for photonics applications, and many of the optical properties still need to be studied. However, their low switching energy and their wide gamut of attractive properties surely point photonic researchers in a new direction. Growing these superlattices is more complex than simply sputtering a chalcogenide film from an alloy target at room temperature because the films exhibit a high degree of (001) crystalline orientation. This requires optimizing the crystal growth process at elevated temperatures; typically, in the range of 200 to 300 °C.¹⁵⁷ The methods to grow the superlattices exploit vdWs epitaxy¹⁵⁸ using either sputtering,^{122,159} molecular beam epitaxy (MBE),¹⁶⁰ or pulsed laser deposition (PLD).^{161,162} The main advantage of sputtering is that it can produce highly uniform films over large areas, and the process is relatively simple. However, the sputtering plasma may damage the growing crystal, and therefore care must be taken to confine the plasma close to the sputtering target. This can be achieved by using low-power plasmas. The main disadvantages of MBE are the small sample sizes and the inability to stoichiometrically deposit from alloy source materials. However, the crystal growth parameters are better controlled by MBE and, consequently, it has the potential to produce films with large crystal grains or even single crystals. PLD can also produce epitaxial films, but unlike MBE, the source materials can be alloy targets and a background gas pressure can be introduced to influence the crystal growth. Indeed, PLD Sb₂Te₃–GeTe superlattices are usually grown in a background pressure of Ar.^{161–163} Interestingly, the PLD growth of Sb₂Te₃ can be performed at a lower temperature than that required for sputtering and MBE because of laser ionization effects extending adatom diffusion lengths.¹⁶² This is important because the typical growth temperatures used in MBE and sputtering are close to the temperature where Te atoms stop adhering to the substrate. An important trick has been developed by Saito to improve the quality of vdW epitaxially grown superlattices.¹⁶⁴ It involves a two-step process, where a 4 nm thick amorphous Sb₂Te₃ layer is initially deposited at room temperature to seed templated growth of a highly oriented crystal at elevated temperature.¹⁶⁴ Although not explicitly studied for superlattice growth, we suspect that CVD-based approaches may also be used to grow superlattices. Indeed, CVD has already produced high-quality Sb₂Te₃ nanowires.¹⁶⁵

3. PHASE TRANSITION FOR ELECTRONIC NANODEVICES

As early as 1968, Ovshinsky reported reversible electrical switching phenomena. At room temperature, chalcogenides are in the amorphous phase, in which atoms are disordered and

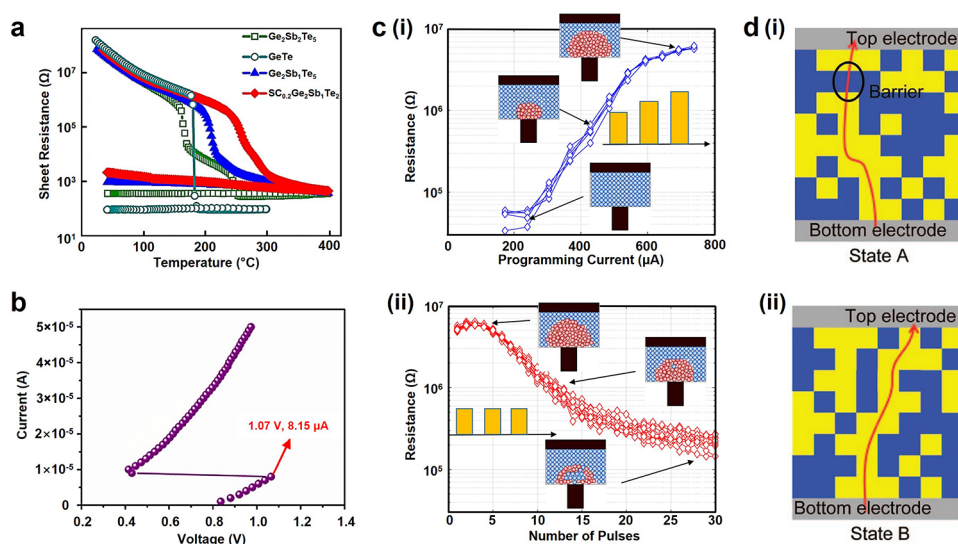


Figure 8. Electrical properties of PCMs. (a) The change of sheet resistance with different in situ annealing temperatures for the GeTe, GST, $\text{Ge}_2\text{Sb}_1\text{Te}_2$, and $\text{Sc}_{0.2}\text{Ge}_2\text{Sb}_1\text{Te}_2$ films.¹⁷¹ Reproduced with permission from ref 171. Copyright 2019 Acta Materialia Inc. (b) I – V curve of the Sb–Ge SLL thin films. The threshold switching can be seen when the curve snaps back.¹⁷² Reproduced with permission from ref 172. Copyright 2017 Elsevier BV. (c) Iterative RESET and cumulative SET process. (i) Possible achievable resistance values as a function of partial RESET pulses with varying amplitude. (ii) Evolution of resistance values versus the successive application of a SET pulse with the same amplitude.¹⁷³ Reproduced with permission from ref 173. Copyright 2018 The Authors. (d) Schematic showing different mixed-phase configurations characterized by an incomplete (i) or complete (ii) percolation path through low-resistivity crystalline grains. The resistance is smaller in state A due to a small amorphous “barrier”. Yellow, crystalline; blue, amorphous.³² Reproduced with permission from ref 32. Copyright 2010 American Chemical Society.

show the covalent type of bonding.⁵⁷ After the transition to the crystalline phase, long-range order of delocalized-bonding is built, facilitating high electric polarizability.¹²⁷ On the basis of this principle, electrical resistivity can change dramatically when phase transition happens in these chalcogenides, which provides opportunities for their follow-up applications. In this section, we start by introducing the electrical properties of chalcogenide PCMs, followed by discussion of their applications on NVM and neuromorphic devices.

3.1. Electrical Properties of PCMs

The energy bandgap in the amorphous phase is larger than that in the crystalline phase, leading to higher electrical resistance. For example, the bandgap of the commonly used material $\text{Ge}_2\text{Sb}_1\text{Te}_2$ is ~ 0.7 eV in the amorphous phase, compared to ~ 0.5 eV in crystalline phase,¹⁶⁶ and this results in a resistance contrast in ~ 2 orders.^{167,168} In the crystalline state, the conduction/valence bands are well-defined just like typical semiconductor materials, while in the amorphous state the bandgap is occupied by many localized states, which remarkably contribute to the density of states.¹⁶⁹ However, these states cannot provide mobile carriers for electrical conductance due to their highly localized character. Therefore, the bandgap in the amorphous phase means the energy range with deficient mobile carriers instead of a gap with no energy states.³²

The electrical resistance in the amorphous phase can be described by Poole–Frenkel (PF) effect, which is affected by an external electrical field and thermal excitation.¹⁷⁰ The conductivity of amorphous PCMs is dependent on the temperature, as shown in Figure 8a.¹⁷¹ Because of the thermal activation effect, the resistivity of 50 nm thin films decreases gradually with increasing temperature until the phase transition point, at which the resistivity drops sharply due to the crystallization process. As discussed, the disorder–order phase transition can happen under different external stimulations. In electrical devices, a typical crystallization method is to apply a

voltage/current pulse with relatively low amplitude and long width to PCM cells, heating the material above the crystallization temperature (T_c). For reamorphization, a short pulse with high amplitude is needed to increase the temperature above the melting point (T_m) and then quenches quickly. For the most used GST devices, the SET (crystallization) time is tens of nanoseconds, while the RESET (reamorphization) time is tens of picoseconds. The most peculiar electrical characteristic of PCM is the threshold of switching in current–voltage (I – V) curves. For instance, Figure 8b reports the I – V curves of Ge/Sb SLL structures with different voltages.¹⁷² If the PCM is initially in amorphous state with high resistivity, the curve suddenly snaps back under continuously increasing voltage. The voltage value at the abrupt change point of resistivity is known as threshold voltage (V_{th}). It is worth noting that reaching this specific V – I point does not necessarily lead to phase change as the material needs enough long time to be heated above T_c and crystallize.³²

Usually, the resistivity of intermediate states is related to the ratio of the crystalline to amorphous parts.⁵⁸ Multiple intermediate resistance levels can be achieved starting from either an amorphous or crystalline state. By sending a series of electrical pulses with a fixed width but various amplitudes to materials in crystalline phase, the volume of amorphous phase can be gradually increased.^{173,174} This process is named iterative RESET, describing the gradual transition from SET (crystalline, highly conductive) to RESET (amorphous, highly resistive) state. Contrarily, cumulative SET can be achieved by applying pulses with the same width and small amplitude.^{173,174} The resistance changes through the iterative RESET and cumulative SET process are illustrated in Figure 8c.¹⁷³ The multiple resistance levels achieved in PCMs play a key role in multiple level cell (MLC) and neuromorphic devices.³³ Apart from the volume ratio of composite phases, the intermediate resistance is also influenced by the percolation of carriers through dispersive

crystalline grains.³² For instance, Figure 8d shows the schematic drawing of two different intermediate state configurations, which can be described by the percolation path of crystalline grains. In state A, the current is impeded by an amorphous high-resistive block, leading to a relatively higher resistance compared with state B, in which no barrier blocks the current path. Because of the stochasticity in crystallization process, the distribution of crystalline grains varies in different devices and programming cycles, which causes cell resistance fluctuation even in the same intermediate level.

3.2. Phase Transition Based Nonvolatile Memory (NVM)

The electric field driven reversible phase transition is reported in 1869, while its application of memory devices has been only realized based on GeTe in 1986¹⁴ and GeTe–Sb₂Te₃ pseudobinary alloy in 1987.¹⁷⁵ Phase transition-based memory is first commercialized in the optical field including compact disks (CDs), DVDs, blu-ray disks, and high-definition digital versatile disks (HD DVDs).¹⁵ The NVMs based on phase transitions utilize the resistance contrast between the amorphous (RESET, high resistivity) and crystalline (SET, low resistivity) to store the data. When the memory is working, a weak readout electrical pulse that does not disturb the SET/RESET state will be sent to the cell, measuring the resistance of memory units. Recently, artificial intelligence (AI) technologies are developed to achieve accurate target recognition, recommendation system, automatic drive, and other tasks by designing programs mimicking neural networks of human brains. Running these software algorithms requires a high level of computing power and a large space of data storage, raising the issue of how to store the massive data accurately and read it quickly. The interest in phase transition-based NVM is triggered by the fast development of optical phase-change technology and a need of breaking the limit of classical memory.

In general, an excellent memory should have good performance including fast SET speed, low RESET energy, good thermal stability and cyclicity, long data retention, large resistance contrast, and low resistance drift. To achieve these objectives, many technologies are developed in recent decades. Herein, we focus on research progress in phase transition based NVMs and discuss how to improve those technologies from perspectives of doping, exploring alternative materials, redesigning the memory cell, and adopting heterogeneous structures.

3.2.1. Compositional Modification via Doping. Doping impurities in semiconductors is a typical technique to control carrier densities, Fermi level, and other properties,¹⁷⁶ widely used in configuring PCM to enhance memory cell performances. From the early 2000s, many dopants, including C,^{177–181} N,^{182–185} Cu,^{186–188} Ni,¹⁸⁹ O,¹⁸⁹ Ga,¹⁹⁰ Ru,¹⁹¹ Sc,^{171,192} BN,¹⁹³ and SiC,¹⁹⁴ have been used in GeSbTe or GeTe alloy with reported enhanced performance. Dopants can increase the disorder or form new types of bonds in amorphous states, leading to higher resistance and increased T_c . High resistive PCM can help decrease the RESET energy, and the elevated T_c can enhance the thermal stability. Therefore, most research in this area focuses on reducing RESET power and improving thermal stability. In a memory cell, data retention temperature for 10 years ($T_{10\text{years}}$) is a significant parameter to evaluate the thermal ability, which can be defined by the Arrhenius equation⁵⁵

$$t = \tau \exp\left(-\frac{E_a}{k_B T_{10\text{years}}}\right) \quad (1)$$

where t is the failure time for the initial resistance to drop to its half value, τ is a proportional time constant, E_a is the activation energy for crystallization, and k_B is the Boltzmann constant.

In 2003, Honi et al. tried to increase the PCM resistivity by doping nitrogen. With 7% N doping, the grain size was suppressed, leading to high resistivity and increasing the T_c by 50 °C when compared to that of the undoped GST.¹⁸² The memory cell can operate with 0.6 mA–50 ns RESET current with 2⁷ cycles, which is reduced by 60% in contrast to the undoped GST of 1.5 mA. However, the resistance contrast of this device is only 6–8, still not large enough for long-term memory application. Later in 2012, Cheng et al. incorporated N in the material along the Sb₂Te₃ and Ge tie-line. Through abundant Ge concentration and N doping, the crystallization temperature can be elevated to 413 °C with the reduced RESET current of 50–100 μ A and resistance contrast of 1–2 orders.¹⁸⁴ Compared to conventional GST material, the 10-year retention temperature is increased by around 33 °C from 87 to 120 °C, satisfying the requirements of good thermal stability in many fields such as the automotive industry. Using a similar method of doping N in Ge-rich GST, 10-year data retention of 210 °C was reported with the expense of resistance drift.¹⁹⁵ Nevertheless, the increased T_c in these works causes low crystallization speed and long SET time. To this end, Sc doped GST alloy was proposed recently, which can be set with an ultrashort electrical pulse of 6 ns, 10-year retention temperature of 119 °C, and 77% RESET power reduction compared to the GST cell.¹⁹² The octahedral Sc–Te motifs in RESET state act as crystallization precursors and shorten nucleation incubation time, therefore yielding the ultrafast switching speed. Meanwhile, the smaller grain size in Sc-doped GST alloy results in larger crystalline resistance, which can explain the significantly reduced RESET power and good thermal stability.

Compared to GST, GeTe shows higher T_c (\sim 185 °C) and 10-year retention temperature (\sim 94 °C).¹⁸⁶ Zhang et al. investigated the effect of doping Cu in GeTe and found that the crystallization temperature can be enhanced to 230 and 260 °C for Cu_{0.06}(GeTe)_{0.94} and Cu_{0.13}(GeTe)_{0.87}, inducing 10-year data retention at 151 and 185 °C, respectively.¹⁸⁶ The enhanced thermal stability can be explained by the large number of bonds introduced by the dopants, which increases the activation energy for SET state. Meanwhile, the increased resistance contributes to the reduced SET pulse in only 80 ns, much faster than the GeTe PCM cell. However, its disadvantage is that the resistance contrast of \sim 2 orders can only remain stable within 2.8×10^3 cycles, which may not meet the requirement of a commercial device. To this end, Hu et al. reported Cu-doped GeTe material Ge₄₀Cu₂₀Te₄₀ in 2018, which can be used as a PCM memory cell to achieve 10-year data retention at 159 °C with an electrical pulse of 5 ns up to 1×10^6 cycles.¹⁸⁸ Besides, other dopants were also explored in GeTe in the last decades. For example, under SET pulse width of 6 ns, 10-year data retention at 149 °C is achieved by doping Ni.¹⁸⁹ The device can keep the resistance contrast of 2 orders for $\sim 3 \times 10^4$ operation cycles. Recently, the device performance of Ru doped GeTe alloy was analyzed, and Ru_{6.8}Ge₅₀Te₅₀ was reported to show 114.9 °C data retention for 10 years with 6 ns SET pulse length. The good thermal stability is due to the refined grain size in the crystalline phase, which can improve the adhesion between the PCM and the surrounding material.¹⁹¹

Additionally, other characteristics of phase transition-based memory such as resistance drift were also improved by incorporating with impurities.^{178,181} The resistance drift in

Table 2. Device Performance of Doped GeSbTe–GeTe Alloy

material	SET pulse width	RESET power/current/voltage	thermal stability	cyclability	resistance drift	refs
C-doped GeSbTe	250 ns	>50% current reduction than GST device	10-year @ 128 °C	1×10^8 cycles	$\nu = 0.046$	178, 180, 181
N-doped GeSbTe	100 ns	50–100 μ A	10-year @ 210 °C	1×10^7 cycles		182, 184, 195
Cu-doped GeSbTe	300 ns	1.5 V	10-year @ 134 °C	3×10^4 cycles		187
Sc-doped GeSbTe	6 ns	77% power reduction than GST device	10-year @ 160 °C	1×10^6 cycles		171, 192
Ga-doped GeSbTe	2 μ s	4 V	10-year @ 135 °C	1.05×10^5 cycles		190
SiC-doped GeSbTe	20 ns	3 V	10-year @ > 120 °C	1×10^5 cycles		194
C-doped GeTe	1 μ s	30% current reduction than GST device	10-year @ 127 °C			177
N-doped GeTe	100 ns	30 mA	10-year @ 154 °C		$\nu = 0.145$	183
Cu-doped GeTe	80 ns	2.5 V	10-year @ 185 °C	1×10^6 cycles		186, 188
Ni-doped GeTe	6 ns	Lower than GeTe device	10-year @ 149 °C	3×10^4 cycles		189
Ru-doped GeTe	6 ns	3 V	10-year @ 144.9 °C	8.5×10^4 cycles		191

SET states originates from the stress release after quick quenching in the RESET process, which causes the material relaxation to lower energy state. Basically, the resistance drift is governed by a power-law relationship as^{33,55,58}

$$R(t) = R(t_0) \left(\frac{t}{t_0} \right)^\nu \quad (2)$$

Here t is the time since the cell is programmed, and $R(t_0)$ is the resistance at time t_0 . The power term ν is the drift coefficient which can evaluate the resistance drift. Hubert et al. investigated the device performance of carbon-doped GST (C-GST) and found that the drift coefficient ν decreased much from 0.119 to 0.046 when the carbon concentration increased from 0 to 15%.¹⁷⁹ The main reason for the smaller drift coefficient is the reduced resistance in the amorphous state, as reported by Lacaita group.¹⁹⁶ Besides, the resistance drift in the amorphous state was evaluated in C-GST (5%) and C-GST (10%) recently.¹⁸¹ With the same operating voltage, the cyclability and resistance drift performance are continuously enhanced by doping more C in GST. The researchers argue that the stable resistance in RESET state roots in the generation of C–Ge chemical bonds when GST is doped with a low C concentration. When increasing the carbon concentration to 10%, the structure distortion is moderated by C–Sb bonds, which further improves the resistance stability. The summary of device performance based on doped GeSbTe–GeTe alloy is shown in Table 2.

Even without new chemical elements, changing the composition of PCMs can modify the device's performance. Cheng et al. explored Ge-rich $\text{Ge}_2\text{Sb}_1\text{Te}_2$ which is dubbed as "golden composition" and examined the performance of a 128 Mb PCM test chip based on this material.¹⁹⁷ Although there is a sacrifice on switch speed and resistance drift, experiment results show a 30% reduction of RESET current and ~ 100 °C increase of T_c when compared to conventional GST material. In 2014, the effect of Ge composition in $\text{Ge}_x\text{Te}_{1-x}$ on resistance drift was explored.¹⁹⁸ In the flexible glasses state ($x < 0.25$), the drift coefficient reduces with decreasing Ge content until 0.05. However, after the Maxwell rigidity transition from a flexible to a rigid state, the material exhibit even worse resistance drift. This work presented the relationship between stiffness and resistance stability, which is suggestive for further material modification.

3.2.2. New Material Developments. Along with doping the traditional GST, alternative new materials have also been explored as NVM candidates. Sb–Te alloys present fast crystallization speed due to their growth-dominated mechanism in the SET process, in contrast to the nucleation-dominated mechanism of GST.¹⁹⁹ However, the low T_c and poor data

retention limit their applications in phase transition based NVM. Accordingly, many researchers devoted themselves to optimizing the Sb–Te alloy performance by incorporating this kind of material with other chemical elements. Among all elements, titanium doped Sb–Te (Ti–Sb–Te) alloy is commonly used and can achieve fast switching speed with low RESET power.^{199–204} The decreased power consumption roots in the resistance increase in the crystalline phase due to reduced mobility and thermal conductivity.^{200,202} By doping Ti, the crystallization temperature will be improved, leading to improved thermal stability and 10-year data retention temperature. Simultaneously, fast phase transition can still be realized because of the small grain size (in nanometers) and point defects introduced by the Ti atoms in the growth-dominated crystallization process.^{202,203} Furthermore, the reduction of grain size and density change during phase transition can help improve the adhesion between substrate and PCM, which contributes to the device's stability. Zhu et al. fabricated a T-shaped PCM cell based on $\text{Ti}_{0.4}\text{Sb}_2\text{Te}_3$ alloy, and the device can be SET in 6 ns with 10^7 cycles.²⁰¹ Compared to the GST cell with the same bottom electrode contact (BEC) size, the RESET power of the $\text{Ti}_{0.4}\text{Sb}_2\text{Te}_3$ cell can be reduced by $\sim 78\%$. They explained the enhancements by the Ti-centered atomic motifs (TCAMs), which can fix the local structures in both amorphous and crystalline states. The robustness of the atomic structure can facilitate the fast phase transition and lower energy consumption.

Apart from titanium, other elements were also doped in Sb–Te alloy including Al,²⁰⁵ Sc,^{140,206} Er,²⁰⁷ Ag,²⁰⁸ Zn,²⁰⁹ V,²¹⁰ Mo,²¹¹ and Ta.²¹² After incorporation with these impurities, most of the doped Sb–Te materials show good performance in SET speed (due to growth-dominated crystallization process) and thermal stability (increased crystallization temperature via doping effect). In 2017, Rao et al. demonstrated a $\text{Sc}_{0.2}\text{Sb}_2\text{Te}_3$ -based conventional phase-change random-access memory (PCRAM) which can achieve a switching speed of 700 ps with no need of preprogramming.¹⁴⁰ The ultrafast writing speed can be attributed to both the suppressed stochasticity of nucleation, which is due to the strong chemical bonds between Sc and Te. Furthermore, $\sim 4 \times 10^7$ cycles can be achieved with RESET energy 1 order of magnitude lower than that of the GST device. Recently, Ta doped Sb–Te alloy was reported with ultrafast SET speed of 2 ns and good thermal stability.²¹² When Ta is doped as impurity, it tends to strongly bond with the Te atom, which makes the device able to retain the data for 10 years at 115 °C. Moreover, combining Ta and Te leads to the increase of Sb–Sb homogeneous bonds and causes an ultrahigh

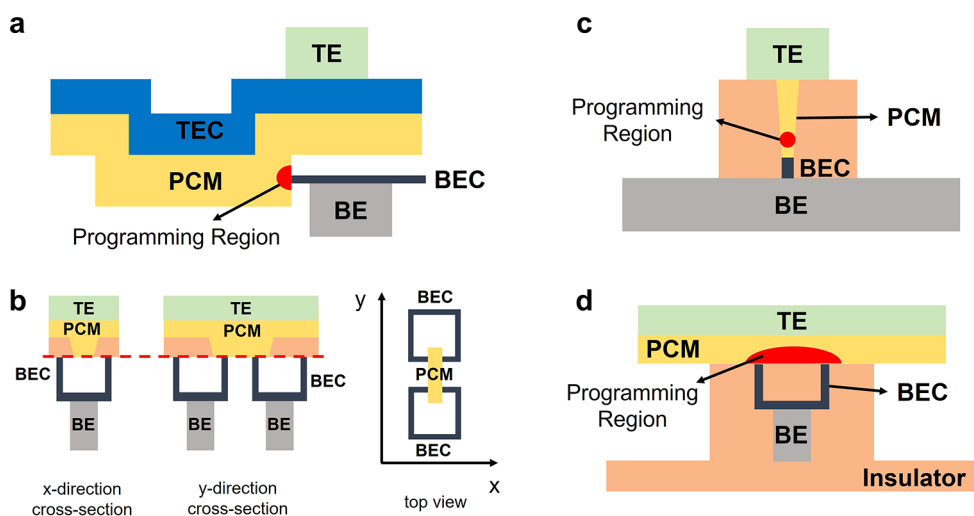


Figure 9. Schematic diagrams of various device structures of PCM-based memory. (a) Edge contact type. (b) μ -trench type. (c) Confined volume type. (d) Ring type.

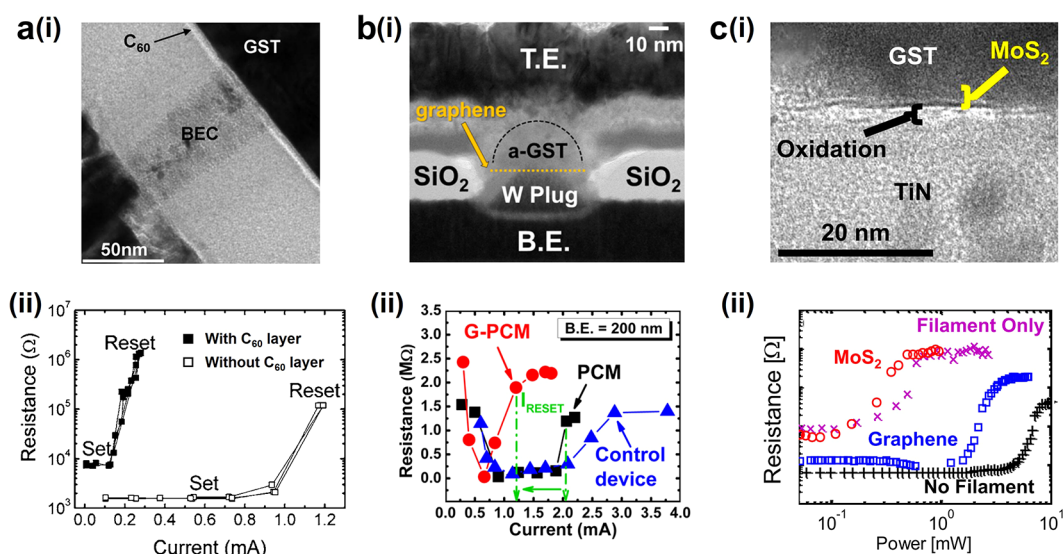


Figure 10. NVM based on PCMs consisting of heterostructures with a single interfacial layer. (a) A PCM cell with a thin C₆₀ film (several nanometers) inserted between GST and BEC. (i) The cross-section image of the proposed PCM cell. (ii) The comparison of resistance changes with and without the C₆₀ layer after applying an electrical pulse for 50 ns.²³⁰ Reproduced with permission from ref 230. Copyright 2008 American Institute of Physics. (b) A PCM device with a graphene layer inserted between the PCM and the W plug. (i) Cross-sectional image of the device in the RESET state with the position of graphene highlighted with a dashed orange line. (ii) The comparison of the resistance change of G-PCM device, control samples without the graphene and with a wider graphene layer.¹⁴⁸ Reproduced with permission from ref 148. Copyright 2015 American Chemical Society. (c) A PCM device with a layer of MoS₂ inserted between GST and TiN. (i) Cross-sectional image showing the position of the oxide filament and 2D material layers in a PCM device. (ii) The resistance change as a function of the input power of different devices. Red circles, device with a MoS₂ interfacial layer and an oxide filament; purple Xs, controlled device only with oxide filament; blue squares, device with graphene interfacial layer and oxide filament; black crosses, device with graphene interfacial layer and no oxide filament.¹⁵⁰ Reproduced with permission from ref 150. Copyright 2019 The Author(s).

operation speed. The grain size is limited to smaller values due to the three-dimensional (3D) confinement of the Ta impurity, contributing to efficient Joule heating and lower power consumption. To further improve the material stability, codoping of two different dopants in Sb–Te alloy can help reduce the volume change. For instance, codoping of O–Ti,²¹³ Ge–Bi,²¹⁴ Sc–Bi,²¹⁵ Al–Sc,²¹⁶ and Sc–Y²¹⁷ have been reported in recent years for performance optimization.

With the development of simulation and material modeling methods, more candidates for phase transition-based material are screened and proposed.^{218,219} Liu et al. screened 158 candidates by checking the compounds, bandgap, local

structure, and phase stability of 124 515 inorganic compounds. After further analyses such as bond angle, cohesive energy, and Born effective charge, 52 materials were proposed to be potentially used in nonvolatile memory applications, including CdPb₃Se₄, AgBiTe₂, TlBiTe₂, etc.²²⁰

3.2.3. Novel Cell Designs. Apart from material modification, new designs of memory cells have also been demonstrated to reduce power consumption. As the RESET current is proportional to BEC area,⁵⁵ one strategy is to minimize the contact size by optimizing architectural design such as edge contact type,²²¹ confined volume type,^{222–225} μ -trench

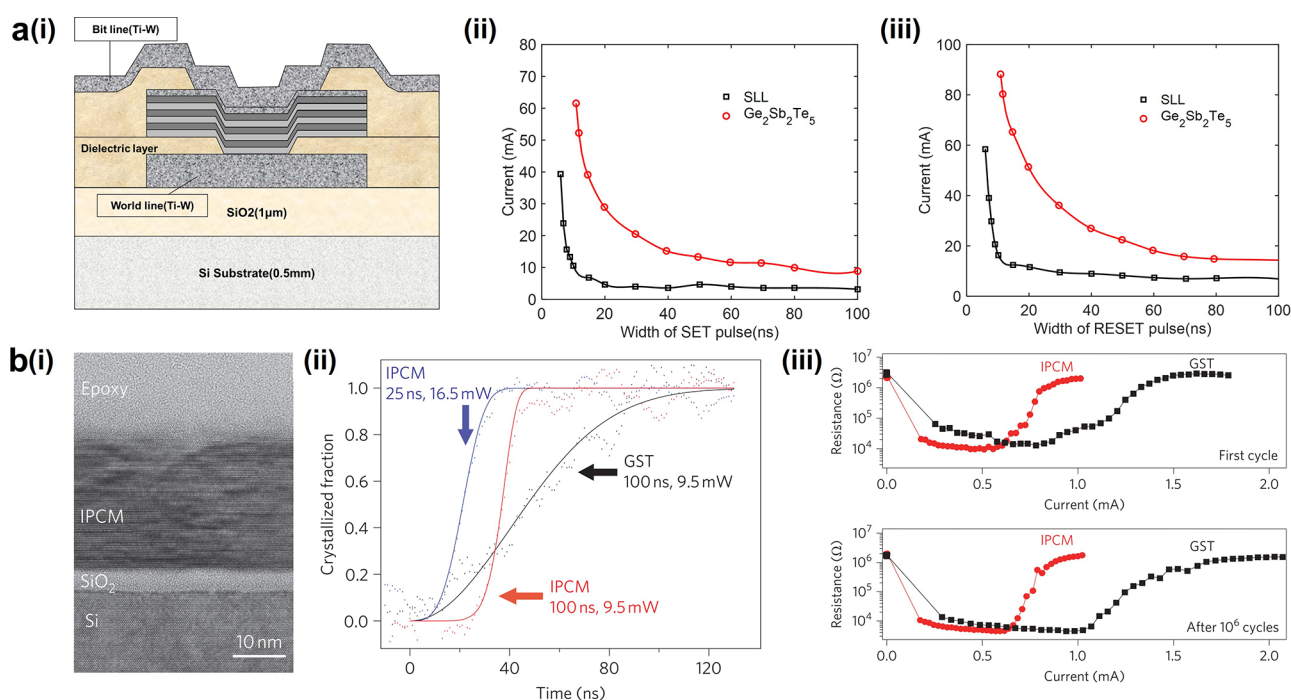


Figure 11. NVM based on superlattices and SLL heterostructures. (a) A phase-change random access memory (PCRAM) cell with GeTe–Sb₂Te₃ SLL structures. (i) Schematic diagram of the proposed cell structure. (ii) Comparison of the SET current versus pulse width between the SLL structure and the conventional GST material. (iii) Comparison of the RESET current versus pulse width between the SLL structure and the conventional GST material.²³⁷ Reproduced with permission from ref 237. Copyright 2006 American Institute of Physics. (b) An iPCM with GeTe–Sb₂Te₃ heterostructures. (i) TEM image of the proposed (GeTe)₂(Sb₂Te₃)₄ interfacial phase-change material on a silicon substrate. (ii) The change of recrystallized fraction versus time for GST (100 ns, 9.5 mW pump pulses; black); iPCM (100 ns, 9.5 mW pump pulses; red); iPCM (25 ns, 16.5 mW pump pulses; blue). (iii) Comparison of resistance change versus current between the iPCM and the GST-based cell in the first cycle (top) and after 1 × 10⁶ cycles (bottom).¹²² Reproduced with permission from ref 122. Copyright 2011 Nature.

type,^{226,227} ring type.^{228,229} The schematic diagrams of these cell designs are shown in Figure 9.

In edge contact type cell, the contact area between PCM and BEC is determined by the thickness of bottom electrodes instead of the photolithography area in conventional bottom contact type structures. By decreasing the contact size to ~4000 nm², a low RESET current of 0.2 mA can be realized with an electrical pulse of 30 ns.²²¹ Alternatively, confining the volume can also result in a small contact area, leading to a high-density memory cell with a reduced RESET current of 80 μA.²²⁴ Another type of structure design is named a μ-trench, in which two neighboring cells share a common top electrode. The BEC area is confined by the width of the trench, where PCM is deposited in one direction and by the thickness of the heater sidewall in the other direction.²²⁶ By using this μ-trench design, the RESET current was reduced to 400 μA from 700 μA in the traditional bottom contact structure.²²⁷ In 2006, Jeong et al. developed an advanced BEC with a ring-type contact scheme, in which the TiN is only deposited in the bottom and outer part of the bottom electrode.²²⁹ Compared to the memory cell with the same size, the contact size of the ring-shaped BEC is reduced, leading to a decreased RESET current of 0.57 mA. Simultaneously, the contact area variation with disturbed BEC size is smaller than the conventional type of contact, which means a reliable cell distribution between the device to device.

3.2.4. Heterostructures with a Single Interfacial Layer.

During the operation process, the thermal energy generated by Joule heat is mainly distributed near the interface between PCM and BEC. However, because of the good thermal conductivity of bottom electrodes, the heat will dissipate into surrounding

materials, leading to low thermal efficiency. Accordingly, the power consumption could be reduced by inserting a barrier with high thermal resistance to increase the heating efficiency of cells. In recent years, various materials have been explored to be used as thermal isolators to reduce RESET power. In 2008, Kim et al. proposed a PCM cell with low RESET power by inserting a thin C₆₀ film (several nanometers) between GST and BEC, the cross-section image of which is shown in Figure 10a(i).²³⁰ Both the interfacial contact resistance and sheet resistance contribute to the increased total electrical resistance in the SET state, leading to a considerable boost of Joule heatings. Simultaneously, the C₆₀ film acts as a thermal isolator to confine the heat dissipation due to its low thermal conductance, resulting in a dramatic reduction of the RESET current after the insertion of the C₆₀ film (Figure 10a(ii)). Thereafter, tungsten trioxide (WO₃)²³¹ and titanium dioxide (TiO₂)^{232–234} were also exploited as thermal barriers to decrease power consumption.

One issue of memory cells with a single interfacial layer is the poor stability and endurance due to the atomic intermixing of PCMs and thermal barrier materials.^{232,234} To solve this problem, a 2D thermal isolator with the thickness of a subnanometer was introduced. In 2015, Ahn et al. reduced the RESET current to ~40% by inserting a graphene layer of similar size of the BEC between the GST and the W plug while sustaining 10⁵ cycles.¹⁴⁸ The cross-sectional transmission electron microscope (TEM) image and electrical properties of the memory device are shown in Figure 10b. Although graphene is highly conductive in the direction parallel to the surface plane, it has high thermal resistance in the cross-plane direction due to the weak vdWs interfaces.²³⁵ The thermal resistance restricts the

heat flow to surrounding materials and enhances the heating efficiency. Then in 2016, Zhu et al. reported GST–graphene–GST structure, in which the graphene layer acts as external electrical and thermal resistance.²³⁶ Additionally, the upper GST films can prevent heat dissipation through the top electrode in the crystalline state. Thus, the RESET energy could be further reduced to 1.5 nJ with 10^6 cycles. Lately, the advantage of small BEC size and 2D thermal barriers was combined by introducing a volume confined cell with insertion of MoS₂ ultrathin (0.6 nm) layer.¹⁵⁰ The schematic diagram of the memory structure is demonstrated in Figure 10c(i), in which the oxide filament layer is introduced to reduce the contact area between the PCM and the BE. The experimental results show that the confined cell volume contributes 70% reduction of the RESET current while the 2D MoS₂ film is responsible for the other 30% decrease due to its low thermal out-of-plane conductivity. The RESET power of devices with different structures is exhibited in Figure 10c(ii).

3.2.5. Superlattices and Superlattice-Like (SLL) Heterostructures. As mentioned, doping is an effective method to increase the data retention temperature by escalating T_c of PCMs. However, the excellent device performance of fast switching speed <10 ns together with a good endurance > 10^8 cycles has not been reported yet in memory cells based on homogeneous PCMs.⁵⁵ In this context, the advent of superlattices and SLL heterostructure paves a new way to further enhance the performance of phase transition-based nonvolatile memories. The concept of SLL structure was first proposed by Chong et al. in 2006.²³⁷ Instead of using homogeneous GST material, they applied a 50 nm thick GeTe–Sb₂Te₃ SLL structure with a mole ratio of 2:1, which is the same as GST (Figure 11a(i)). A significant reduction of SET/RESET current was achieved due to the 30% lower thermal conductivity of SLL than GST single layer (Figure 11a(ii,iii)). Furthermore, the improved thermal efficiency, as well as the fast crystallization of Sb₂Te₃, leads to the fast SET speed with 5 ns pulse width. The memory cell can retain its good performance for 10^7 cycles, which is mainly because of the small active area, short duration of temperature high than the melting point, and the stable chemical bond of Ge–Te and Sb–Te near the interfaces. With this experimental demonstration of SLL reported, more efforts have been devoted to study the physics behind the enhanced performance of GeTe–Sb₂Te₃ SLL structures. For instance, the effect of GeTe sequence on phase transition has been studied.^{238,239} Through first-principal calculations, it is reported that the Ge–Te–Ge–Te sequence has the lowest energy in (GeTe)₂(Sb₂Te₃)₁ superlattice and therefore cannot be operated with SET/RESET cycles.²³⁸ By comparing characteristics of GeTe–Sb₂Te₃ superlattice and single Sb₂Te₃ alloy with the same GeTe top layer, Ohyanagi et al. found that only the region around the top layer is responsible for the switching.²⁴⁰

Apart from GeTe–Sb₂Te₃ SLL structures, other heterostructures have also been explored. The design principle of SLL is to achieve good endurance, high thermal stability, and rapid crystallization speed. For example, Tan et al. deposited GST and N-doped GST (N-GST) film alternately and achieved both low RESET current (37% reduction) and high endurance (~ 10^8 cycles) due to compositional matching between N-GST and GST, which reduced the interfacial diffusion gradient and the phase change-induced stress.²⁴¹ Another strategy is to combine the material with good thermal stability and the alloy with fast phase change speed. In 2017, Hu et al. fabricated the SLL GeTe–Sb thin films, and the phase switching speed of GeTe alloy was enhanced by incorporating with Sb material.²⁴² The

experiment results indicate that the resistance in the RESET state, as well as the switch time, is lower with thicker Sb films when the size of the GeTe layer is fixed as 5 nm. In the same year, Liu et al. combined SnSb₄ and SbSe to form a multilayer structure and investigated its performance.²⁴³ Because of the fast-switching speed of SnSb₄ and excellent thermal stability of SbSe, the SLL can switch from RESET to SET state in only 5 ns with 10-year data storage under 122 °C.

Another technology is depositing superlattices to improve the device performance. The critical difference between the SLL heterostructures and superlattice structures is that SLL structures are deposited at room temperature in an amorphous state, while superlattices need to be grown with preferred crystallographic orientation. As a pioneer in this field, research group of Tominaga demonstrated iPCM data storage devices for the first time in 2011 (Figure 11b(i)).¹²² They aligned the <111> direction in a GeTe layer and the *c*-axis of a Sb₂Te₃ layer and formed heterostructure, in which the chemical bond changes from covalent type (RESET state) to resonant type (SET state) when optical pulses are applied. The device can switch from RESET to SET state in just 25 ns due to the pre-existing nucleation interfaces provided by Sb₂Te₃ layers (Figure 11b(ii)). The SET energy of this proposed device is 11 pJ, which is much smaller than 90 pJ of a conventional GST device. The switching performance with ultralow energy consumption can be reserved even after 10^6 cycles (Figure 11b(iii)). The decreased power consumption of iPCM relies on interfacial atomic transitions, which minimize the change in entropy and lead to fast and low energy switching. By lowering the entropy of the RESET state, the device properties such as resistance variations can be highly repeatable with a million cycles. In addition, the cycle limit of the iPCM does not depend on film thickness strongly, which means the device can be switched between SET and RESET states for more than a billion cycles with an ultrathin film (15 nm). Another exotic characteristic of iPCM structure is that it can exhibit a topologically nontrivial band structure, and its properties can be engineered through strain controlling approach.^{244,245} Then in 2019, Okabe et al. investigated the switching mechanism of GeTe–Sb₂Te₃ iPCM and found that the thermal properties of iPCM account only for ~13% reduction of RESET current change when compared with traditional GST alloys.²⁴⁶ Another significant cause of the reduced RESET energy is the void migration process, in which the random voids distributed in iPCM move and concentrate around BEC, leading to smaller BEC area and RESET current. Recently, the resistance drift in GeTe–Sb₂Te₃ iPCM was analyzed by Zhou et al.²⁴⁷ Through electrical transport measurement, it has been shown that interface defects and body defects in bulky PCMs account for the suppressed resistance drift. Therefore, the reliability properties of PCM can be optimized through structural parameters such as the single period length of the superlattice.

An alternative method is to confine the atoms to prevent long-range diffusion along the pulsing direction by introducing multilayer heterostructures assembled from sheets of confinement material and PCM. In 2019, Ding et al. proposed the basic requirements of confinement material,¹³⁹ which should (1) be dynamically robust as effective diffusion barriers, (2) be chemically inert and have weak coupling to PCM, (3) have similar local arrangements to that of the crystalline PCM, (4) be thermally resistive to prevent thermal diffusion, (5) have almost same electrical resistance as PCM, and (6) be compatible to current PCMs and devices. On the basis of these selection

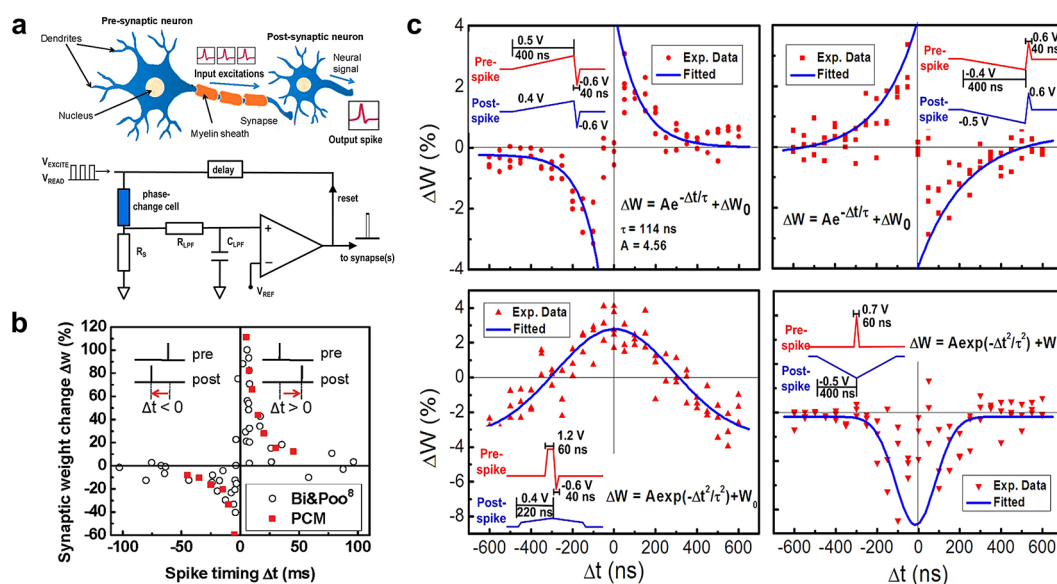


Figure 12. PCM-based neuromorphic devices. (a) A self-resetting spiking phase-change neuron based on PCM.³⁴ Reproduced with permission from ref 34. Copyright 2018 IOP. (b) Synaptic weight change as a function of the relative timing of pre- and postspikes.³⁹ Reproduced with permission from ref 39. Copyright 2012 American Chemical Society. (c) Different relationships between the weight change and the relative timing of pre- and postspikes. Top left: antisymmetric Hebbian learning rule. Top right: antisymmetric anti-Hebbian learning rule. Bottom left: symmetric Hebbian learning rule. Bottom right: symmetric anti-Hebbian learning rule.⁵⁸ Reproduced with permission from ref 38. Copyright 2013 The Authors.

principles, TiTe_2 was chosen as confinement material, and Sb_2Te_3 was picked as PCM. The memory device built on the $\text{TiTe}_2/\text{Sb}_2\text{Te}_3$ heterostructure showed fast switching speed and low energy consumption, which is attributed to the improved thermal efficiency via the confinement layers and the potential nucleation sites introduced by TiTe_2 . Furthermore, such heterostructure exhibits ultralow resistance drift with $\nu = 0.002$ at the RESET state and $\nu = 0.001$ at the SET state. This can be explained by the absence of Ge and tetrahedral defects in Sb_2Te_3 as well as the limited structural relaxation in the heterostructure. Recently, SLL structures with other compositions have also been investigated including such as $\text{V}_2\text{O}_5/\text{Sb}$, $\text{GeTe}-\text{Bi}_4\text{Te}_3$,²⁴⁹ and much more.

3.3. Phase Transition Based Neuromorphic Devices

In past decades, AI technologies are developed and shown to endow the powerful capability of massive data processing using, for example, artificial neural networks. However, the current von Neumann structure limits the computational power due to the heavy data transmission between processors and memories.⁵⁸ Thus, novel computing structures have been proposed to break this bottleneck, where PCMs provide a new platform to achieve neuromorphic computing. The name neuromorphic computing originates from its imitation of neural networks in the human brain, which is mainly composed of neurons and synapses. A neuron consists of three parts: dendrites, soma, and axons (Figure 1c). When the dendrites receive a postsynaptic potential pulse (PSP), the soma decides to fire a presynaptic pulse (PRP) if the amplitude of the PSP exceeds the threshold, and then the axon transfers the new pulse to the next neuron. Between two adjacent neurons, the synapse determines the weight of spiking pulse transmission from PRP to PSP, which changes during the “learning” process, which is named “spike-timing-dependent plasticity” (STDP). If the PRP stimulates the adjacent neuron to transmit a new pulse, the synaptic efficacy will be increased as long-term potentiation (LTP). On the other hand, if the PRP happens after the emission of the next neuron, these two spiking

pulses will be considered as unrelated and the strength between the neurons will be compressed, which is termed as long-term depression (LTD).

PCMs are suitable for neuromorphic devices due to their threshold switching and gradual crystallization/amorphization characteristics.⁶⁸ Besides, the high performance including excellent thermal stability, fast switching speed, and low energy consumption make PCMs possible for large-scale production and commercialization. The basic principles of neuromorphic devices are similar to that of PCM-based memory.⁵⁸ However, because neuromorphic devices require multiple resistance levels, which deserves special attention.⁵⁸ For instance, to emulate the continuous weight change of synapsis, the resistance window between amorphous and crystalline states should be large enough to sustain multiple intermediate levels. Simultaneously, the resistance in intermediate states should be stable and robust to avoid misidentifications, which requires ultralow resistance drift and variability between different cycles. What is more, during iterative RESET/cumulative SET process, the resistance increase/decrease should follow a linear relationship.

Artificial neurons are important building blocks of spike-based neural networks in modern technologies,⁵⁸ which can be built based on PCMs. The basic function of an artificial neuron is to process incoming signals and fire a new pulse when the sum value exceeds the electrical threshold. In 2016, Tuma et al. used the effective thickness of the amorphous region in mushroom-shaped GST to represent the neuronal membrane potential, which can be measured by the electrical conductance.³⁵ By sending crystallizing pulses to amorphous GST alloy, the PCM can crystallize gradually. Simultaneously, the electrical conductance increases and surpasses the firing threshold of $\theta_{\text{th}} = 2$ μS . After that, the crystalline GST will be RESET to amorphous state by applying an electrical pulse with high amplitude and be ready for the next cycle. On the basis of this concept, a spiking phase-change neuron with self-resetting characteristic was put forward, the schematic diagram of which is demonstrated in Figure 12a.³⁴ Under the electrical excitation, the conductance of

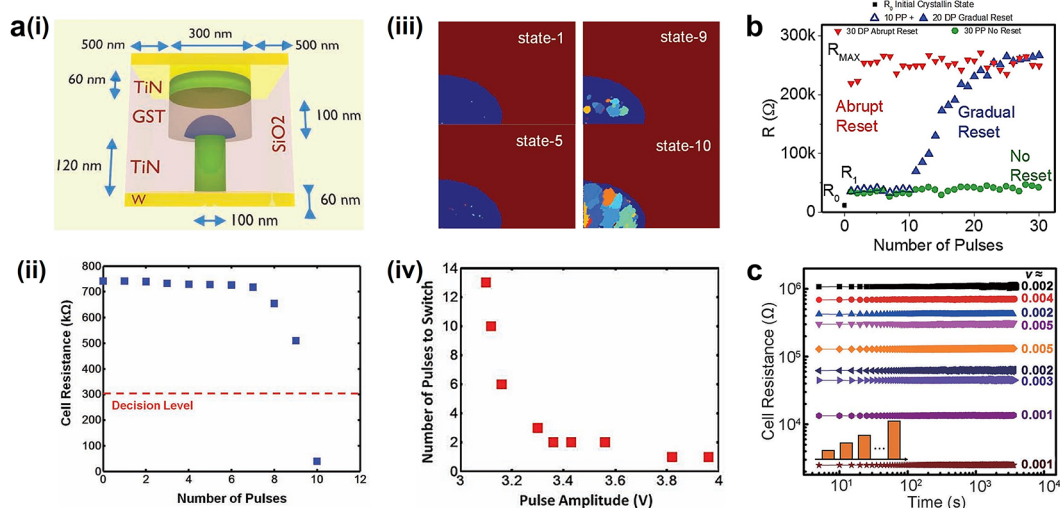


Figure 13. PCM-based computing device and improvement methods. (a) A nanoscale phase-change memory device with arithmetic computing. (i) Schematic of the PCM mushroom-type cell used for the base-10 accumulator response. (ii) The resistance changes of the PCM cell with the application of each of 10 input pulses. (iii) Showing the simulated structure of the active region after the first, fifth, ninth, and tenth pulses (i.e., state-1, state-5, state-9, and state-10). Dark blue regions, materials in the amorphous state; various colors, materials in the crystalline state. (iv) The number of (≈ 100 ns) pulses needed to switch a cell from high-resistance to low-resistance with different pulse amplitudes.³⁷ Reproduced with permission from ref 37. Copyright 2013 Wiley-VCH. (b) A bidirectional artificial synapse. R_0 is the initiation state. For the gradual reset process, the application of 10 potentiation pulses (PP, voltage of 1.25 V) is needed first to set the cell to R_1 (“memory window initialization” step). Then 20 depression pulses (DP, voltage of 1.6 V) are applied to reach gradually R_{\max} (blue curve). Otherwise, the device is set suddenly to R_{\max} via the application of 30 DP (red curve), or the cell is set abruptly to R_1 without a RESET transition (green curve).³⁶ Reproduced with permission from ref 36. Copyright 2018 Wiley-VCH. (c) The resistance drift of different levels during the iterative RESET process in $\text{TiTe}_2/\text{Sb}_2\text{Te}_3$ heterostructure.¹³⁹ Reproduced with permission from ref 139. Copyright 2019 The American Association for the Advancement of Science.

phase-change cells can decrease abruptly, resulting in a sudden increase of voltage at the junction point of the phase-change cell and its series resistor R_s . With a high input exceeding the V_{REF} of the comparator, a RESET electrical pulse with high amplitude will apply on the artificial synapse and RESET the PCM cell.

Another important component of neuromorphic devices is the synapse, the weight of which can be adjusted through the learning process via STDP. In 2012, Kuzum et al. proposed a PCM array to emulate neural networks, with the GST cell playing the role of synapses.³⁹ The prespike is set as a pulse train composed of depression (amplitude increases) and potentiation (amplitude decreases) pulses, while the postspike is designed as a 120 ms continuous weak pulse with an 8 ms negative pulse at the center. By controlling the sequence of prespike and postspike, the synaptic weight can be changed and quantified using an exponential relationship as

$$\Delta w = Ae^{-\Delta t/\tau} \quad (3)$$

where Δw is the synaptic weight change in percentage, Δt is the interval between the prespike and postspike, A is the parameter describing the amplitude, and τ is the time constant representing the curve shape. A comparison of the STDP behavior between PCM cells and biological data is exhibited in Figure 12b. The rate of synaptic weight change concerning spiking time interval can be modified by controlling the time constant τ . By decreasing the time spacing between the pulses in prespike, the STDP curve becomes sharp, which means a smaller τ value. Apart from the conventional exponential relationship between the weight change and the time interval, other learning rules can also be achieved via dedicated designing of the pulse shape of pre- and postspike. For example, Figure 12c shows various learning rules by applying spikes with different shapes, including antisymmetric Hebbian learning rule (top left), antisymmetric

anti-Hebbian learning rule (top right), symmetric Hebbian learning rule (bottom left), and symmetric anti-Hebbian learning rule (bottom right).³⁸

Beyond basic artificial neurons and synapse devices, other novel devices for computing are also reported. One interesting device is to achieve arithmetic computing using the accumulation property of GST materials (Figure 13a(i)), which means the abrupt resistance decrease lower than the decision level after several crystallization pulses.³⁷ The resistance decreases gradually with the first nine input pulses of 1.085 V and 60 ns and drops suddenly with the application of the 10th electrical pulse (Figure 13a(ii)). The composition changes during the accumulation process accordingly (Figure 13a(iii)). In addition, the number of crystallization pulses needed for the switch can be controlled by the electrical pulse amplitude. Therefore, arbitrary bases can be achieved (Figure 13a(iv)). On the basis of the multilevel resistance, addition, subtraction, and division can be realized for decimal numbers.

As we discussed above, the ideal resistance change during the iterative RESET/cumulative SET procedure should follow a linear relationship. However, because of the quick quenching process in RESET operation, asymmetric weight change usually happens in LTP and LTD. One approach to tackle this problem is to slow down the amorphization process by choosing an initial resistance level.³⁶ Starting from a partial amorphous state, Barbera et al. demonstrated that the resistance can gradually decrease under the excitation of identical electrical pulses, realizing bidirectional artificial synapse. The comparison of resistance change between the initial partial amorphous state and crystalline state is indicated in Figure 13b.

Another problem in neuromorphic devices is the resistance drift. Different from several intermediate levels in multilevel memory, there can be over a hundred states in synaptic devices

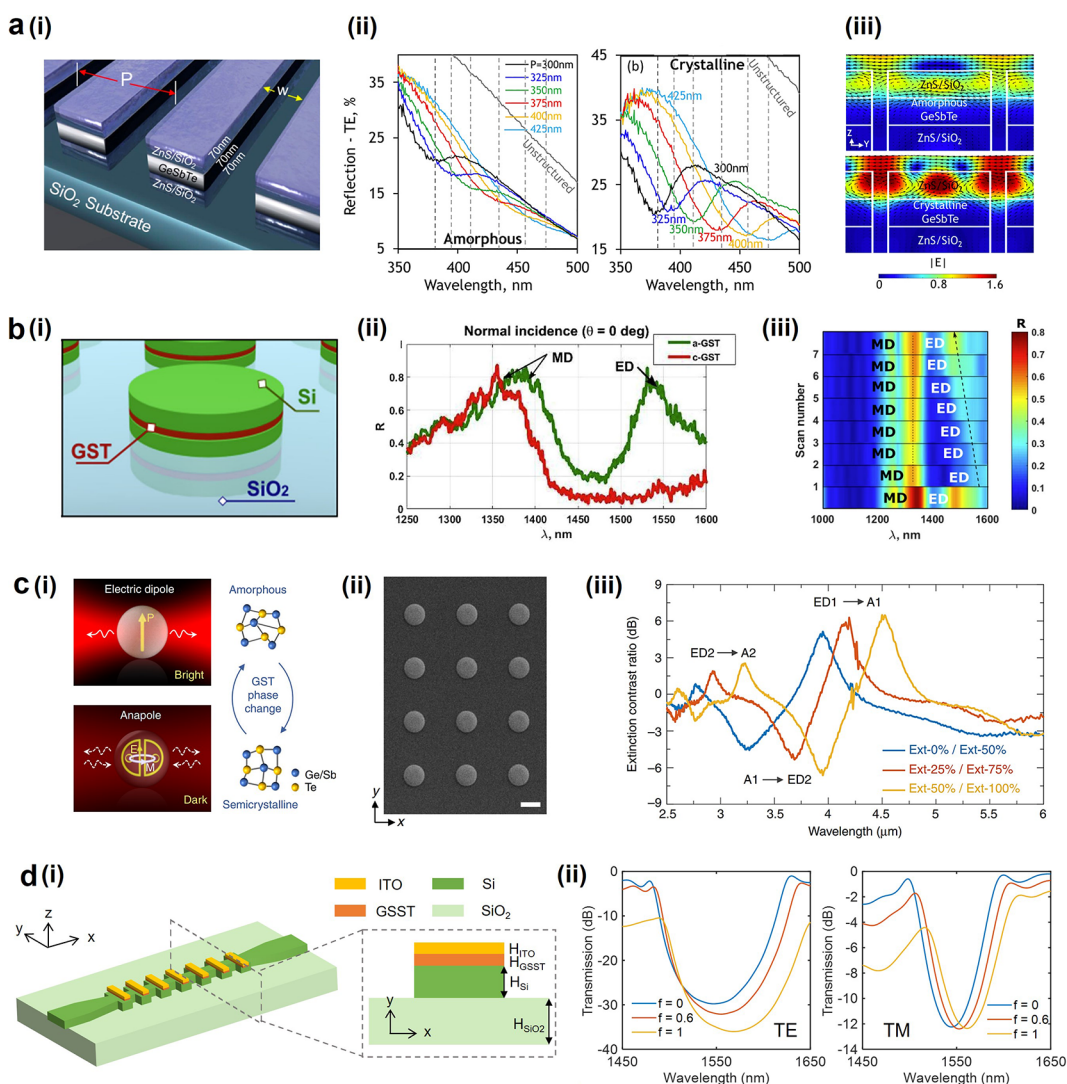


Figure 14. Tunable metasurfaces comprising PCMs for dynamic light intensity control. (a) A reconfigurable all-dielectric UV-HEV metamaterial. (i) Artistic schematic of nanograting structure containing a GST film sandwiched between two ZnS/SiO₂ layers. (ii) Measured reflection spectra of the nanograting metamaterial for the amorphous (left) and polycrystalline (right) states of the GST layer. (iii) The distribution of electric field for the nanostructure with amorphous (top) and crystalline (bottom) GST.²⁷⁶ Reproduced with permission from ref 276. Copyright 2019 American Chemical Society. (b) A reconfigurable hybrid silicon/PCM metasurface with multilevel control. (i) Schematics of the hybrid silicon/PCM metasurface containing arrays of silicon/GST nanodisks. (ii) Reflectance spectra for the device with the GST layer in both amorphous and crystalline states. (iii) Multilevel tuning of the hybrid metasurface. Starting from the amorphous state (bottom panel), the metasurface is first switched to the crystalline state (scan 1) and then switched back to amorphous GST (scans 2–7).²⁷⁵ Reproduced with permission from ref 275. Copyright 2020 Optical Society of America. (c) A multispectral optical switch with multilevel control capabilities. (i) Conceptual illustration of an ED resonance and an anapole excitation in a GST sphere. (ii) SEM image of the GST nanodisks in the multispectral optical switch with multilevel control capabilities (the scale bar represents 2 μm). (iii) Extinction contrasts of GST disks ($R = 1 \mu\text{m}$) with different crystallinities.⁴⁶ Reproduced with permission from ref 46. Copyright 2019 The Author(s). (d) A dual-polarization optical filter based on GSST. (i) Structure of the Bragg grating filter. (ii) Transmission spectra of the optical filter for six crystallization levels with TE (left) and TM (right) mode.²⁹⁹ Adapted with permission from ref 299. Copyright 2021 The Optical Society.

to emulate the continuous weight change smoothly, posing much challenging requirements on stability for artificial synapses. One effective approach to alleviating this problem is to use SLL structures to suppress the spontaneous resistance drift.^{139,247} Figure 13c shows the resistance drift of different levels during the iterative RESET process, which is restrained by the limited structural relaxation of amorphous Sb₂Te₃ sublayers.

4. PHASE TRANSITION FOR NANOPHOTONICS

In past few decades, nanoelectronics has developed rapidly, mostly based on silicon-based microchips. Recent development

in AI technology and massive data have required greater demands on computing power and large-scale data storage, raising the issue of how to break the limitation of traditional Von Neumann architecture. However, the saturation of conventional silicon technology makes it obstructed by Moore's law.²⁵⁰ Similar problems also exist in other nanoelectronic devices, where the integration of electrodes and circuits hinders further reduction of footprint. The advent of nanophotonics, especially on-chip integrated photonics, provides a new platform owing to its small footprint, low cost, and low power consumption.²⁵¹ Moreover, optical components such as metasurfaces, made of assembly of deeply subwavelength nanostructures, and inte-

grated photonics have attracted huge interest and opened great opportunities for optics and photonics for their unique capabilities in controlling light properties in terms of phase, frequency, dispersion, momentum, and polarization.^{40,252–254} Beyond the static metasurfaces with fixed functionality, actively controlled optical components have practical and fundamental significances in autonomous vehicles, robots, display, augmented and virtual reality, consumer electronics, telecommunications, and sensing devices, and could lead to the alluring on-demand optics and photonics.^{1,255}

To achieve the object of active metasurfaces, many technologies have been proposed in recent years. One approach is to use optical nonlinearity to modulate the refractive index of materials through laser pulse.^{5,256,257} However, an ultrafast laser with high power is needed, and the tuning range is rather limited and volatile.²⁵⁸ An alternative way is to use carrier injections through an electrical field, which is usually exploited in ITO^{259–262} and 2D materials.^{263–266} A disadvantage of electrical stimuli is that they are naturally slower than optical processes.⁴¹ Another strategy is to mechanically modulate metasurfaces using a microelectromechanical system (MEMS)^{11,267,268} or stretching flexible materials^{9,269,270} to change their optical properties. Nevertheless, the complexity and instability restrain its application in a wider range. Furthermore, chemical modulation has also been demonstrated by altering optical properties via chemical reactions such as hydrogenation and dehydrogenation processes^{271–274} and others. This tunable technology is only suitable for specific materials (such as magnesium and palladium) and can only be exploited to change the material property of top surface.

Beyond the above technologies, phase transition based on PCMs opens a new opportunity for such tunable and reconfigurable optical components in the UV, visible, and IR spectra due to its large refractive index contrast, various excitation methods (Figure 1a), and fast switching speed. Furthermore, exploiting PCMs to control the flow of different polariton waves can further expand their applications and manipulate light on-chip at the nanoscale in a programmable fashion. Therefore, many types of tunable metasurfaces have been demonstrated, including tunable absorbers and filters,^{46,275–279} phase masks,^{280,281} beam steering,^{25,282–284} display,^{25,67,285} metalens,^{286–289} and enhanced third-harmonic generation (THG).²⁹⁰ On the other side, memory units,^{71,291} switches and modulators,^{292–296} programmable neural networks,²⁹⁷ and arithmetic operations²⁹⁸ are some of the examples of tunable integrated photonic devices proposed. In this section, we first review the application of PCMs as the building block of tunable optical components for light manipulation from the aspects of intensity, wavefront, and tunable integrated photonic devices. Then the recent advances of PCMs on modulation of light at nanoscale are discussed in plasmonic devices, low-loss phonon polaritons, and vdWs polaritonic devices.

4.1. Tunable Metasurfaces for Dynamic Light Intensity Control

When the dielectric constant changes dramatically during the phase transition, the resonance in nanostructures can be modulated and presents large contrast on reflection, scattering, or transmission spectra. Therefore, various tunable metasurface comprising PCMs have been proposed for intensity control from the range of ultraviolet (UV) to MIR. Figure 14a(i) shows the schematic of a nonvolatile reconfigurable all-dielectric metamaterial operating in the UV to high-energy visible (HEV)

consisting of a layered composite of low-loss ZnS/SiO₂ and relatively low refractive index GST.²⁷⁶ The measured reflection spectra of the metamaterial with different periodicities demonstrate that reflection resonances at UV–HEV wavelengths can be substantially modified by light-induced amorphous–crystalline phase transitions of GST (Figure 14a(ii)). After crystallization, the electric field in the overlying ZnS/SiO₂ layer is enhanced because the penetration of fields into the GST layer was minimized (Figure 14a(iii)), and this causes stronger resonance with higher quality factor Q (up to $Q \sim 15$) without a change in resonance wavelength.

In the NIR region, a hybrid silicon/PCM metasurface consisting of arrays of silicon/GST nanodisks (measured nanodisk diameters of 668 nm) on a SiO₂ substrate was proposed for light intensity control near the optical communication wavelength (Figure 14b(i)).²⁷⁵ Amorphous GST has a similar complex refractive index to amorphous silicon in the spectral region interest ($\lambda = 1300$ nm to $\lambda = 1600$ nm), while crystalline GST shows obvious contrast with amorphous silicon with refractive index $\Delta n \sim 1.6$ and extinction coefficient $\Delta k \sim 1.1$. Taking advantage of the permittivity change during phase transition, the electric dipole (ED) resonance at $\lambda = 1540$ nm can be regulated with an absolute modulation depth of 70% (Figure 14b(ii)). Furthermore, reversible multilevel tuning is also achieved by using a single laser pulse with different intensities. Gradual restoration of ED is demonstrated as the GST layer is reamorphized continuously (Figure 14b(iii)). This work paves a new way for a wide range of design possibilities and can be potentially applied in various fields.

Due to its high refractive indices in amorphous states, GST can satisfy the prerequisite of strong Mie resonances at the MIR range.¹³⁴ Combining this possibility with its distinctive tunability, Tian et al. proposed a shifting between ED (amorphous) and anapole (crystalline) resonance in GST nanospheres (Figure 14c(i)).⁴⁶ Moreover, a multispectral optical switch with multilevel control capabilities is also demonstrated in the metasurface consisting of a GST nanodisk array (Figure 14c(ii)). For example, by changing the crystalline phase of GST nanodisks from $C = 0\%$ to $C = 50\%$, the GST nanodisks would be undergoing three varied switching at three different wavelengths simultaneously, obtaining a 6 dB contrast ratio (Figure 14c(iii)). This enables simultaneous “on” and “off” states in different spectral regions. The same behavior was observed when crystalline phase of GST nanodisks were changed from $C = 25\%$ to $C = 75\%$ (red line) and from $C = 50\%$ to $C = 100\%$ (yellow line).

By dedicatedly designing the pattern of nanostructures, polarization-dependent tunable devices can be realized.^{299–303}

As an illustration, Wang et al. reported a dual-polarization optical filter based on the combination of a subwavelength grating waveguide and low-loss GSST PCM (Figure 14d(i)).²⁹⁹ Because of the geometric asymmetry, TM and TE mode experience different effective indices in the grating, leading to separate transmission control of TE and TM mode. By gradually adjusting the crystallization fraction f , the proposed Bragg grating filter can provide up to 20 nm (17 nm) red-shift with intensity modulation of 6 dB (0.15 dB) at 1550 nm for TE (TM) polarization (Figure 14d(ii)).

4.2. Tunable Metasurfaces for Wavefront Manipulation

For light waves, the control of phase is crucial, as it is an essential way to manipulate wavefront. Thanks to its contrast of refractive

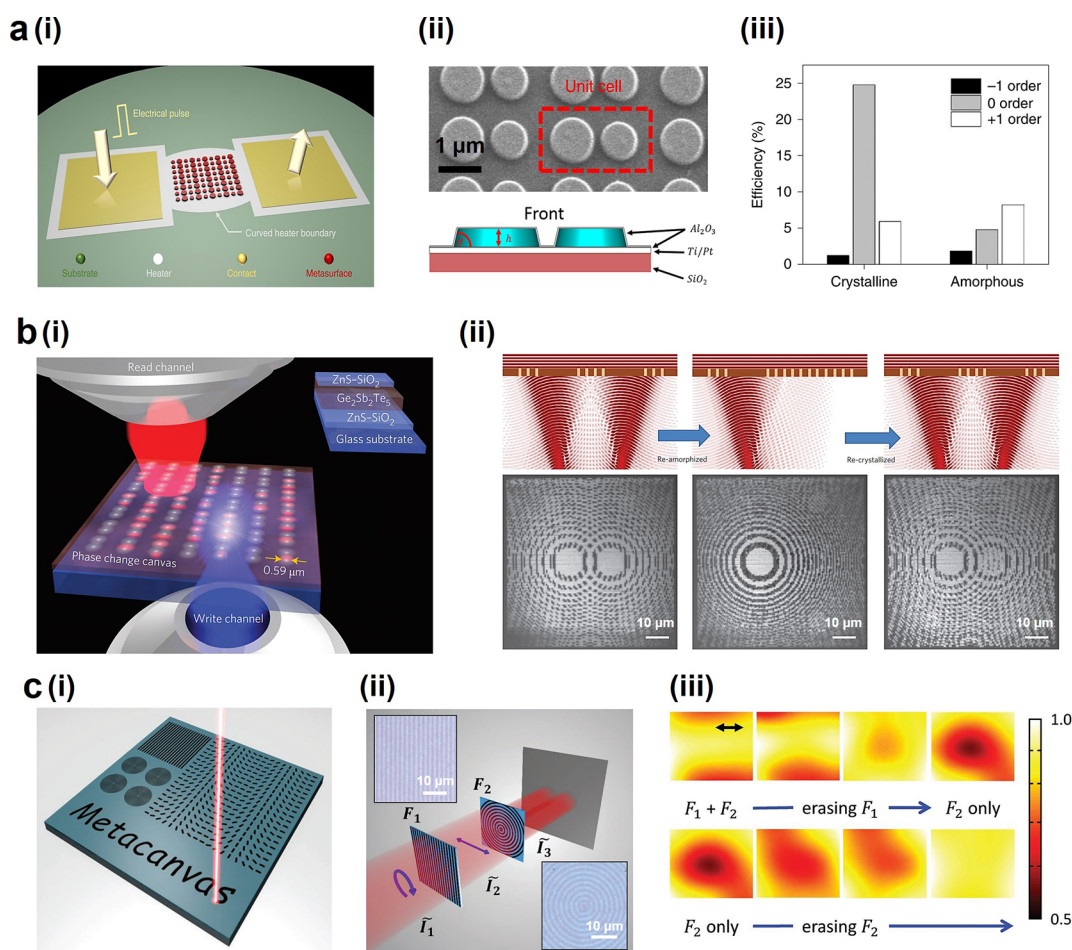


Figure 15. Tunable metasurfaces comprising PCMs for wavefront manipulation. (a) Electrically reconfigurable metasurface based on GST. (i) Schematic of the electrically tunable metasurface on the electrothermal switching configuration. (ii) Top-view SEM image of the fabricated beam steering metasurface consisting of (top) an array of repeating unit cells and (bottom) schematic of each unit cell. (iii) Measured deflection efficiencies of different diffraction orders at $\lambda = 1550$ nm.²⁸² Reproduced with permission from ref 282. Copyright 2021 The Author(s), under exclusive license to Springer Nature Limited. (b) Optically reconfigurable PCM-based metasurface. (i) Schematic of writing a reconfigurable photonic device in a 70 nm thick GST film sandwiched between two layers of 70 nm thick ZnS-SiO₂ films. (ii) Schematic of writing two superimposed Fresnel zone pattern, erasing one of them, and rewriting it. The patterns were imaged at $\lambda = 633$ nm.²⁸¹ Reproduced with permission from ref 281. Copyright 2015 Nature Publishing Group. (c) A lithography-free photonic metacanvas based on VO₂. (i) Schematic of laser writing different photonic operator patterns on a metacanvas. (ii) Schematic of the experimental setup of dynamic transition between different optical fields. (iii) Transmitted light intensity normalized by the profile of the incident light intensity.²⁵ Adapted with permission from ref 25. Copyright 2017 Wiley-VCH.

indices during phase transition, PCMs are exploited in tuning the wavefront of metasurfaces to realize various functionalities such as beam steering, metalens, phase mask, and switchable spin-orbital coupling. For instance, Zhang et al. proposed an electrically tunable metasurface that can achieve polarization-independent phase gradient.²⁸² By depositing the metasurface on the metal heater, electrical pulses can be applied to achieve a reversible switch between the amorphous and crystalline states through the electrothermal effect (Figure 15a(i)). Each unit cell consists of two GSST circular meta-atoms with radii of 560 and 470 nm, respectively (Figure 15a(ii)). A long duration and low-voltage pulse (500 ms, <12 V) triggered the amorphous-crystalline phase transition via Joule heating, and a short and high-voltage pulse (5 ps, 20–23 V) triggered crystalline-amorphous phase transition via a melt-quench process. As shown in the measured deflection efficiencies (Figure 15a(iii)), the reflected light at 1550 nm couples to the +1 order mode ($\theta = 32^\circ$) in the amorphous phase and the 0 order mode in the crystalline phase with contrast ratio to be 8.6 dB.

Owing to the development of modern photonics, it is possible to precisely stimulate the phase transition in desired positions via a focused laser spot. Recently, a platform for reconfigurable optics comprising a thin GST film sandwiched between two ZnS/SiO₂ layers is reported to realize various functions.²⁸¹ Pulses from a Ti: sapphire laser at $\lambda = 730$ nm are focused to excite crystallization (0.39 nJ)/reamorphization (1.25 nJ), leading to changes in the complex refractive index (Figure 15b(i)). The right Fresnel zone in the written pattern for focusing the incident light to foci can be erased and then restored on the GST thin film (Figure 15b(ii)). Similar functions can also be obtained using VO₂ film (Figure 15c(i)).²⁵ First, the metacanvas is heated up to the transition temperature ($T_C = 68$ °C) where the VO₂ film was kept in the insulator phase. Then, the desired pattern is written by a focused laser in the VO₂ film by locally heating and changing its phase to metallic. Finally, the pattern could be erased by reducing the global temperature down. The metacanvas should be reheated to be ready for rewriting a new pattern. On the basis of this technology, dynamic transitions between different optical fields are demonstrated using two

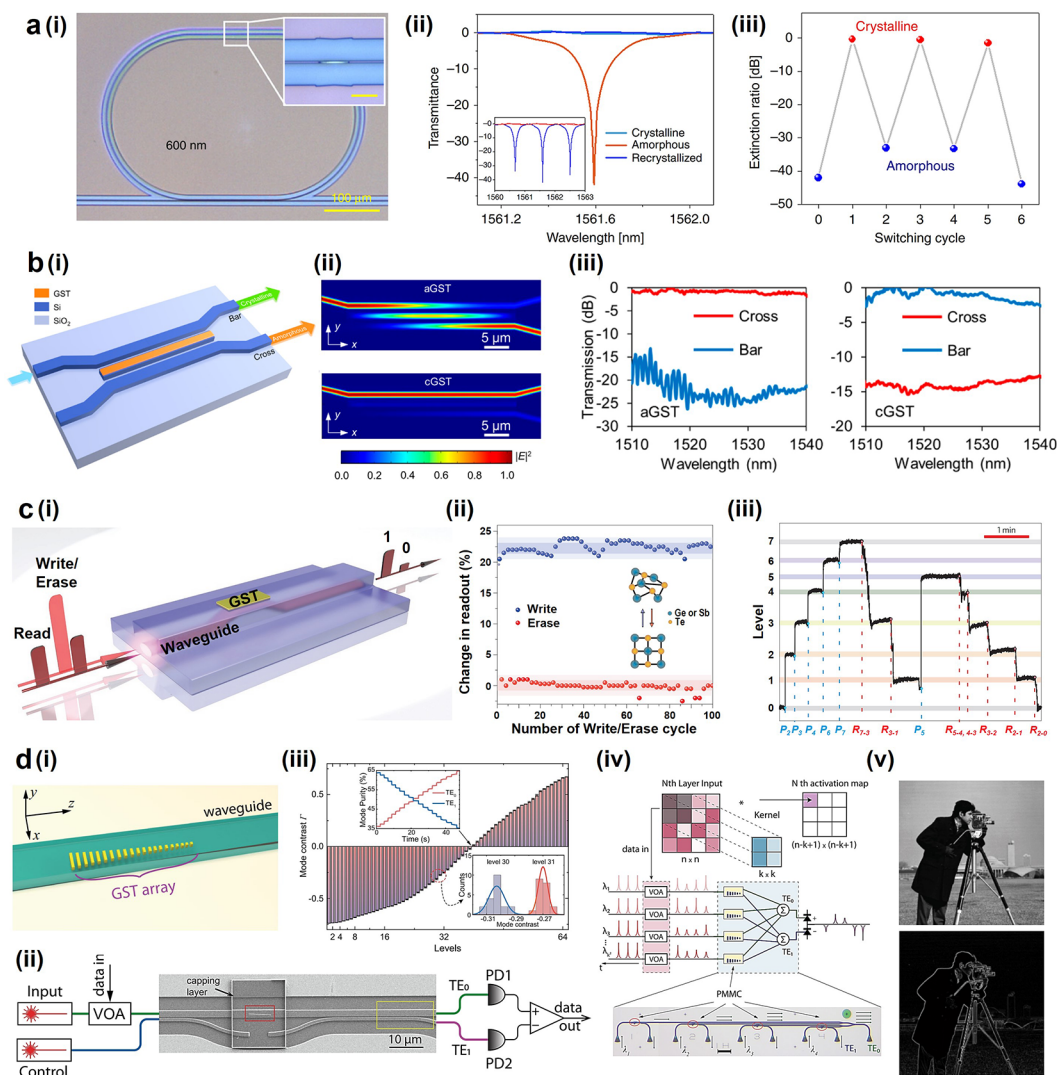


Figure 16. Tunable integrated photonic devices comprising PCMs. (a) A high-performance optical switch working near the optical communication wavelength. (i) Optical micrograph of the resonant switch with inset showing the PCM strip on top of the SiN waveguide. (ii) Normalized transmittance spectra of the resonant switch, showing complete ON/OFF modulation of the resonant peaks. Inset: transmittance modulation in broadband. (iii) Resonance extinction ratio modulation of the device upon laser switching.²⁹² Reproduced with permission from ref 292. Copyright 2019 The Author(s). (b) A nonvolatile PCM-clad silicon photonic 2×2 switch. (i) Schematic showing the photonic switch. (ii) Normalized optical field intensity distribution in the device for amorphous GST (a-GST) and crystalline GST (c-GST) at 1550 nm. (iii) Measured transmission at the cross and bar ports with amorphous and crystalline GST.³⁰⁴ Reproduced with permission from ref 304. Copyright 2019 American Chemical Society. (c) Integrated all-photonic nonvolatile multilevel memory. (i) Schematic of the operational principle of all-optical memory metadevice. Reading, writing, and erasing are performed by ultrashort optical pulses through the waveguide. (ii) Repetitions of the switching cycle over 50 cycles. Shaded areas show the measured confidence interval. (iii) The GST-based microdevice can be operated with eight levels by increasing the readout power by a factor of 10. Each level can be reached from a higher level by applying a partial Erase R_{n-m} .⁷¹ Reproduced with permission from ref 71. Copyright 2015 Nature. (d) A programmable waveguide mode converter for a convolutional neural network. (i) Schematic of the GST array deposited on a waveguide. (ii) SEM image of the complete PMMC, and schematic of the measurement and control units. The GST phase gradient metasurface is encapsulated in the red box and the mode selector in the yellow box. (iii) The mode contrast Γ is controlled at 64 distinct levels enabling 6-bit programming resolution. (iv) Schematic of optical convolution for image processing consisting of an array of k^2 PMMC used as photonic computing core. (v) Top: The grey-scale image of the “cameraman” is used as the input image; bottom: All the sharp edges in the original picture are highlighted by combining the horizontal and vertical edges.²⁹⁷ Reproduced with permission from ref 297. Copyright 2021 The Author(s).

metacanvas F_1 (linear polarizer) and F_2 (concentric-ring grating) (Figure 15c(ii)). With the existence of both F_1 and F_2 , the circularly polarized incidence is transformed into linear polarized light (via F_1), which is further transformed into a two-lobe pattern (via F_2). By sequentially erasing F_1 and F_2 , the original two-lobe pattern is converted into a donut shape (via erasing F_1) and uniform field (via erasing F_2) (Figure 15c(iii)). These lithography-free reconfigurable metasurfaces provide a new method to design functional flat optics in large freedom.

4.3. Tunable Integrated Photonic Devices

Apart from active metasurfaces and metamaterials, PCMs can also be integrated into many photonic chips and achieve a wide range of functionalities. For example, an optical modulator near the optical communication wavelength is proposed by exclusively using the change in the real part of the refractive index (Figure 16a(i)).²⁹² In this work, the authors computationally optimized $\text{Ge}_2\text{Sb}_2\text{Se}_x\text{Te}_{5-x}$ alloys to achieve the highest figure-of-merit (FOM), where $\text{FOM} = \Delta n / \Delta k$ (Δn , the change

of real part of the refractive index; Δk , the change of the imaginary part of the refractive index), which is further integrated on top of a SiN waveguide, illustrating modulation of ON/OFF transmission between amorphous and crystalline states (Figure 16a(ii)). A large contrast ratio of 42 dB and low insertion loss of <0.5 dB are achieved with six switching cycles, which outperforms the nanomodulator based on the traditional GST material with a similar design (Figure 16a(iii)). Furthermore, a 2×2 silicon photonic switch is demonstrated using GST.³⁰⁴ The operation principle of this coupler is based on the mode modification of TE-polarized supermodes in the three-waveguide structure, in which a thin layer of GST is deposited on the middle waveguide (Figure 16b(i)). The phase-matching condition can be satisfied with an amorphous state, completing the power transfer from the input port to the cross port. Contrarily, the coupling wavelength of crystalline GST is much larger than that of amorphous GST. Hence, most of the input light cannot be cross-coupled but rather propagates to the bar port (Figure 16b(ii)). This optical switch can work with a bandwidth of 30 nm and be potentially applied in optical interconnects, neuromorphic computing, and quantum computing (Figure 16b(iii)).

Fast development in AI technology renders higher demands on computing power and large-scale data storage, beyond the capability of traditional Von Neumann architecture. To this end, integrated photonics based on PCMs have opened great opportunities for nonvolatile multilevel memory and on-chip computing. An integrated nonvolatile all-photonic memory based on GST is proposed by utilizing the evanescent coupling between light traveling along the waveguide and the GST element.⁷¹ In this microdevice, the reading, writing, and erasing were performed by ultrashort optical pulses ($\lambda_{\text{pulse}} = 1560$ nm) through the waveguide (Figure 16c(i)). The phase state of GST part atop microdevices determined the information saved in the corresponding memory unit, which dictates readout transmission coefficients. The light was absorbed more (21%) when the GST was in the crystalline phase due to high optical loss of GST material around the operational wavelength of $\lambda_{\text{probe}} = 1570$ nm. A single 100 ns optical pulse was used for writing, and a sequence of six consecutive 100 ns pulses was used for erasing. The memory data is reproducible for at least 50 cycles (Figure 16c(ii)). This nonvolatile memory can be operated with eight levels by increasing the readout power by a factor of 10 at speeds approaching 1 GHz (Figure 16c(iii)), validating its potential as all-photonic on-chip memory to outperform conventional von Neumann architectures.

Another way to eliminate the limitation of traditional computing systems is to introduce neural networks for data storage and processing,³⁰⁵ in which neuromorphic photonic devices has been raised as an auspicious hardware accelerator. Recently, Wu et al. reported a programmable waveguide mode converter using GST metasurface, which can be integrated as the photonic computing core in an optical convolution for image processing.²⁹⁷ It consists of a linear array of 30 nm thick GST nanoantennas with tapering widths on a $1.8 \mu\text{m}$ wide and 330 nm thick SiN waveguide (Figure 16d(i)). The GST metasurface was designed in a way that its equivalent wavevector was equal to the difference between the two spatial modes of the waveguide so that it could efficiently convert the TE_0 mode to the TE_1 mode when GST was in the crystalline phase. This mode conversion would be diminished when GST was amorphous, as GST film would have a smaller refractive index and would not satisfy the required phase gradient. Figure 16d(ii) shows the

SEM image of the programmable metasurface mode converter (PMMC) device and the measurement and control units. Optical pulses are used to control the phase of GST metasurfaces and program PMMC devices to control the proportion of output TE_1 mode to input TE_0 mode. The PMMC controls the mode contrast at 64 distinct levels between -0.73 to $+0.67$ at 1555 nm, corresponding to 6-bit programming resolutions (Figure 16d(iii)). This mode contrast could be used as elements in a matrix in a multiply accumulated operation, which is the constitutional step of matrix-vector multiplication (MVM) in all neural network algorithms. Optical convolution for image processing is schematically shown, consisting of an array of k^2 PMMC used as a photonic computing core to store the kernel matrix (Figure 16d(iv)). The patch of pixels of the image (top panel of Figure 16d(v)) is encoded as optical pulses and input into the channels, and the TE_0 and TE_1 outputs were summed and measured. The horizontal and vertical edges were detected separately and then combined to highlight all the sharp edges (bottom panel of Figure 16d(v)). By using nonvolatile GST material in the integrated photonic device, they have enabled programming and in-memory computing capabilities for on-chip neural network algorithms.

4.4. Phase Transition for in-Plane Polaritons

4.4.1. Polaritons in Different Types of Materials. For conventional photonic devices, one obstacle to manipulate a light beam at the nanoscale is Abbe's diffraction limit, which hinders further reduction of element size from about one-half of the operation wavelength.³⁰⁶ Polaritons, hybrid excitation of matter and photons, can overcome the diffraction limitation and provide a new way to control electromagnetic waves. Hence, manipulating light propagation and dispersion by exploiting polaritons has been attracting significant attention from the nanophotonics community in recent years. The propagation behaviors of polariton waves are determined by specific material characteristics, such as SPP³⁰⁷ (photon hybrid with charge oscillations), phonon polariton^{308–311} (photon hybrid with phonons), and exciton polariton^{312–318} (photon hybrid with exciton). Typically, SPPs in metal suffer from intrinsic optical losses with a lifetime of ~ 10 fs.³¹⁹ These losses limit the transmission output and shorten the propagation lengths of SPPs. Polar crystals, such as SiC,³⁰⁸ α -quartz,³¹⁰ and calcite,³¹¹ support strongly confined phonon polaritons (PhPs) in their Reststrahlen band (negative permittivities) in the IR spectrum.^{309,310,320–323} Because phonons have inherently long lifetimes (~ 1 ps) and low optical loss,³²⁴ the SPhPs have lower propagation losses and longer lifetimes as compared to SPP counterparts.

Particularly, the recent emergence of atomically thin, 2D vdW materials of varying electronic types enables new avenues for light-matter interactions from UV–visible to terahertz spectral ranges, as hosts for ultraconfined polaritons within atomically thin volumes.^{325–328} For instance, 2D semimetals such as graphene and small bandgap semiconductors such as BP exhibit tunable and highly confined SPPs^{329–331} and have led to applications such as molecular sensing, tunable THz generation, and electro-optical light modulation.^{332–335} Likewise, natural hyperbolic vdW crystals such as h-BN,^{309,320,322,336} α - MoO_3 ,^{328,337–339} and α - V_2O_5 ,³⁴⁰ support hyperbolic PhPs, which exhibit long lifetimes, ultralow loss (i.e., long-range transport), ray-like collimation, and ultrahigh field confinement, enabling a plethora of unparalleled opportunities in PhP-based

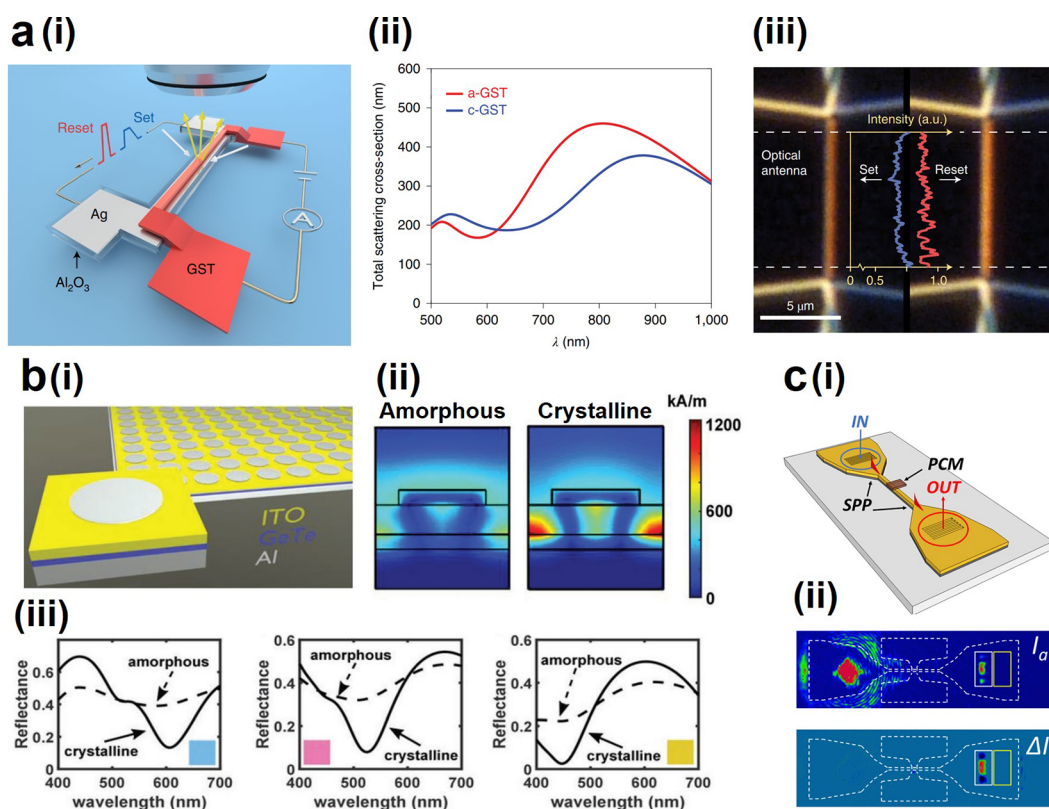


Figure 17. PCM-based plasmonic devices for intensity control. (a) Electrically tunable nanoantenna based on GST. (i) Schematic showing an optical antenna comprised of a GST nanobeam stacked on top of a silver nanostrip, separated by a thin Al_2O_3 layer. (ii) The simulated total scattering cross-section of the optical antenna with a-GST and c-GST. (iii) Dark-field, white-light-scattering images of the antenna taken after a set pulse and a reset pulse, showing a notable change in the scattering intensity. The scattered light intensity measured along the antenna length is plotted in the inset.³⁵⁰ Reproduced with permission from ref 350. Copyright 2021 The Author(s), under exclusive license to Springer Nature Limited. (b) A phase-change metamaterial with the capability of nonvolatile color display. (i) 3D schematic of the phase-change MIM absorber structure and the materials used. (ii) Magnitude of the magnetic field (in the direction perpendicular to the plane) in the MIM absorber with the GeTe layer in the amorphous (left) and crystalline (right) phase. (iii) Optimized reflectance spectra of the cyan (left), magenta (middle), and yellow (right) pixels, as obtained by finite element method (FEM) simulation.⁴³ Reproduced with permission from ref 43. Copyright 2019 The Authors. (c) Active control of surface plasmon waveguides. (i) Schematic showing active control of surface plasmon waveguides with a PCM. (ii) Measured intensity distributions in the amorphous (top) state (I_a) and change of intensity (ΔI) after crystallization of the PCM (bottom).⁶⁹ Reproduced with permission from ref 69. Copyright 2015 American Chemical Society.

functional nanodevices.³⁴¹ In the visible frequency regime, TMDCs support exciton-polaritons, which were recently demonstrated in MoSe_2 with a small polariton wavelength (down to 300 nm) and a long propagation length (up to 12 μm).³¹³

With the galloping development of polariton-based nanodevices, how to actively control in-plane polaritons has become a new objective in the community. To date, many technologies have been proposed to modulate the polariton behavior, including twisting the angle between optical axes of two adjacent metasurfaces,^{339,342–346} hydrogenation of the surface atoms,^{272,347,348} and photoexcitation to inject electron–hole pairs.³⁴⁹ Nevertheless, these modulation methods are rather slow or only limited in specific materials. With different methods to stimulate phase transition in PCMs, such as electrical pulses,^{282,350} optical laser pulses,³⁵¹ and thermal scanning probes,³⁵² it is possible to have simultaneous control of size, position, and phase-transition depth of meta-atoms.³⁵³ Hence, exploiting PCMs with tunable electronic or lattice properties has become a competitive approach to control the flow of different polariton waves and programmably manipulate light on-chip at the nanoscale. Herein, we discuss the applications of PCMs on modulation of in-polaritons from the aspects of plasmonic

devices, low-loss phonon polaritons, and vdWs polaritonic devices.

4.4.2. Phase Transition Based Plasmonic Devices.

Surface plasmons have been viewed as an emerging candidate of information technologies, facilitating high-capacity, high-speed, and integrated plasmonic chips. Because of its sensitivity to the dielectric constant in surrounding materials, plasmonic resonance can be widely modulated by incorporating PCMs with metals, resulting in light intensity change during phase transition.^{27,69,350,354–358} For example, Wang et al. recently stacked GST film on a silver strip, which can serve as heating stage and plasmonic resonator simultaneously (Figure 17a(i)). By sending SET and RESET current pulses through the silver nanostrip, GST can transform between amorphous and crystalline states, leading to the contrast of scattering cross-section (Figure 17a(ii,iii)).³⁵⁰ Modulation of beam amplitude makes it possible to exploit PCMs to realize multiple functionalities. For example, Figure 17b demonstrates a switchable phase-change metamaterial resonant absorber with nonvolatile color generating capabilities by embedding GeTe in metal–insulator–metal (MIM) nanostructure (Figure 17b(i)).⁴³ When the PCM is in the crystalline state, plasmons can be excited and result in a transversal magnetic resonant mode,

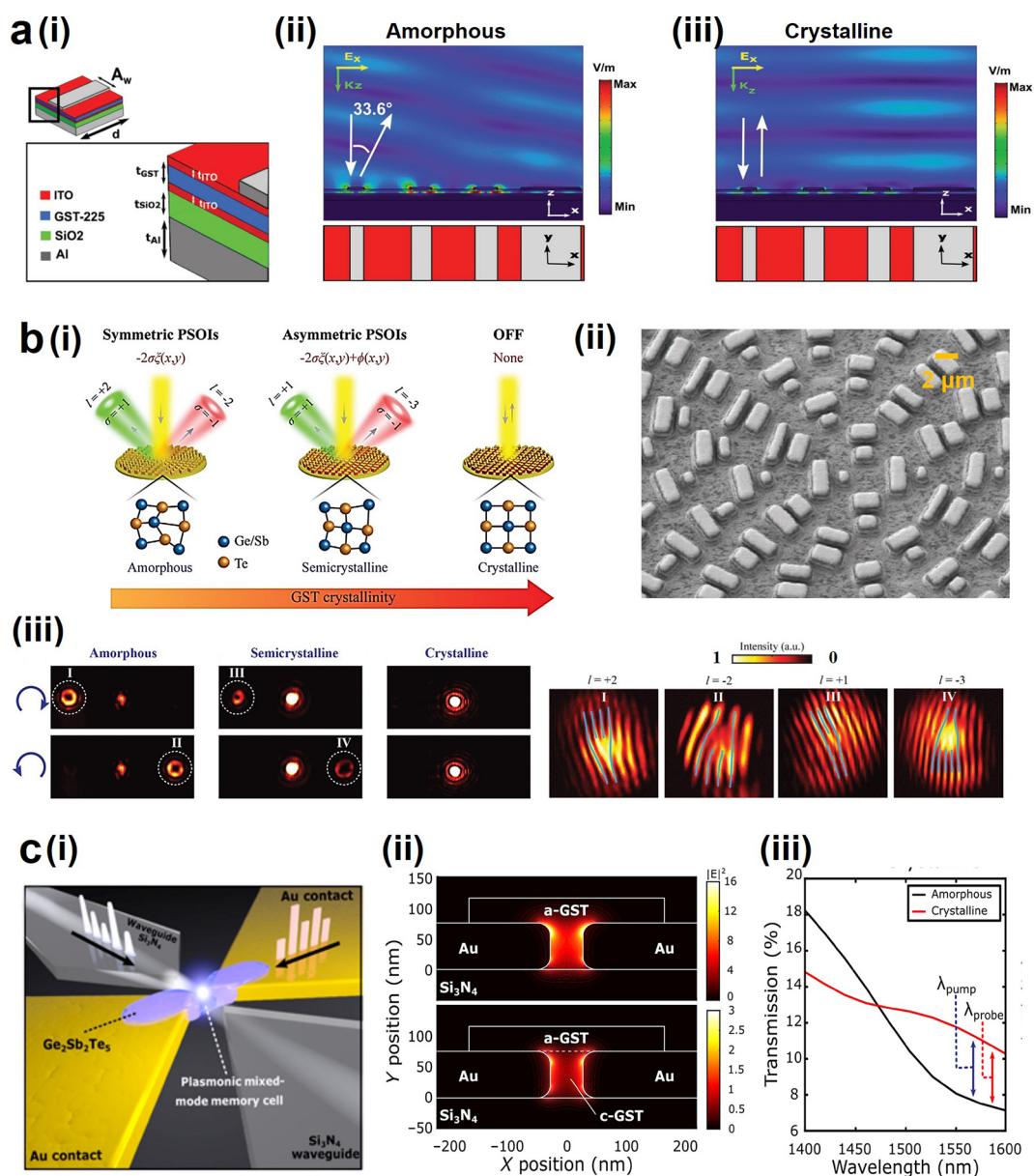


Figure 18. PCM-based plasmonic devices for phase control and waveguide memory. (a) Reconfigurable metasurfaces incorporated with PCM for beam steering. (i) Schematic showing the design of actively controlled beam steering. (ii) Anomalous reflection ($\theta_r = 33.6^\circ$) with amorphous GST layer. (iii) Specular reflection with crystalline GST layer.⁴⁵ Reproduced with permission from ref 45. Copyright 2018 The Authors. (b) Active switching of PSOs in phase-change metasurfaces. (i) The schematic diagram of active PSOs enabled by the proposed phase-change metasurfaces. (ii) SEM images of the fabricated metasurface consisting of top Au and GST nanobar deposited on Au film. (iii) Measured diffraction patterns at different crystallization levels under RCP and LCP illumination (left) and interference patterns obtained through the interference of the orbital angular momenta (OAM) beams and a tilted circularly polarized Gaussian beam (right).³⁶⁷ Reproduced with permission from ref 367. Copyright 2020 Wiley-VCH. (c) Plasmonic memory cell integrated into a photonic waveguide. (i) Schematic of an integrated plasmonic–photonic waveguide memory with dual electrical–optical functionality through embedded PCM (GST) (ii) Simulation of the field enhancement within the nanogap when the GST is in amorphous (top) and crystalline (bottom) state. (iii) The transmission of the device before and after crystallization. The significant change in the refractive index changes the coupling between the nanogap and waveguide, which reduces reflection from the input waveguide, thereby increasing the overall transmission of the device in the crystalline state.³⁷⁰ Reproduced with permission from ref 370. Copyright 2019 The Authors.

leading to wideband absorption in the visible range. Contrarily, the resonant mode is switched off with amorphous PCMs, leading to flat, pseudowhite reflection spectra. The magnetic fields in the amorphous and crystalline states are shown in Figure 17b(ii). By adjusting the geometry of MIM absorbers, the peak position of the reflection spectra can be shifted to present cyan, magenta, and yellow colors (Figure 17b(iii)).

Another application is to employ modulated light intensity to achieve optical switching function.^{69,351} For instance, a

plasmonic switch is achieved when GST is applied on a waveguide to control the propagation of SPP at an Au/SiO₂ interface (Figure 17c(i)). By using a laser pulse to reversibly control the phase of GST transition from its amorphous to crystalline structural phase, the refractive index, transmission, and absorption coefficient of SPPs are modulated, thus enabling optical switching of SPP. As shown in Figure 17c(ii), the intensity at the out-coupling grating changes strongly upon

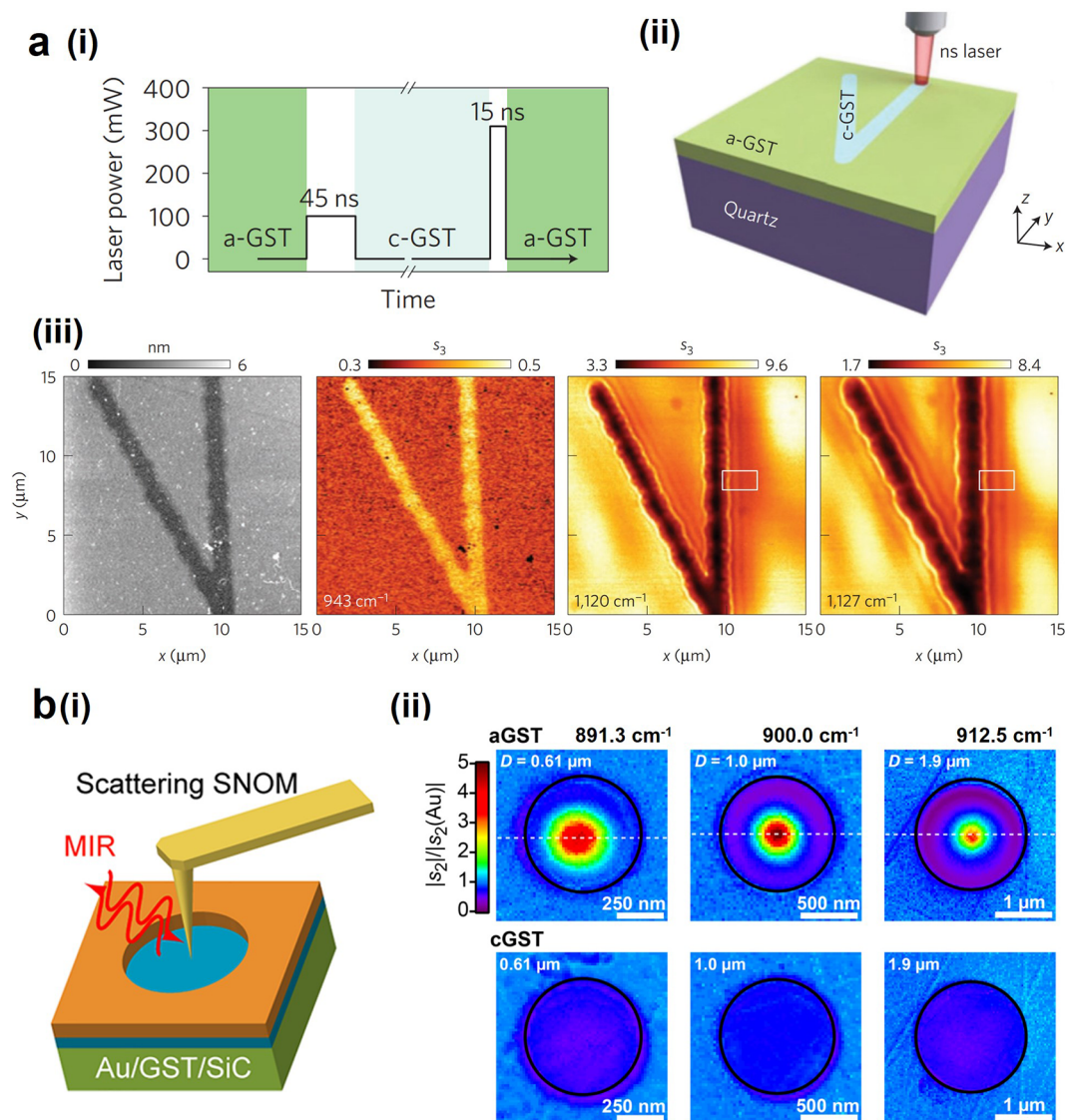


Figure 19. Reversible switching of low-loss and highly confined polaritons. (a) Reversible optical switching of SPhPs with GST-covered quartz. (i) Laser parameters used for switching the GST films. (ii) Schematic of switching a V-shaped domain by scanning a pulsed laser beam. (iii) AFM topographic image (left) and s-SNOM images (left medium, 943 cm^{-1} ; right medium, 1120 cm^{-1} ; right, 1127 cm^{-1}) of the c-GST wedge.³¹⁰ Reproduced with permission from ref 310. Copyright 2016 Nature. (b) Switchable SPhP resonance of planar circular cavities. (i) Cavity structure. The diameters of the metal holes D used are 0.61 , 1.0 , and $1.9\text{ }\mu\text{m}$. (ii) Near-field images of the cavities at different frequencies before (top) and after (bottom) thermal annealing of the samples.³⁷¹ Reproduced with permission from ref 371. Copyright 2019 American Chemical Society.

changing the GST phase, leading to a strong differential signal ($\Delta I \sim 31\%$) upon phase transition of GST.

Apart from intensity control, phase modulation is also required to achieve many important photonic devices in nanoscale. Incorporating PCMs with nanostructures can allow the continuous phase shifter through applied voltage.³⁵⁹ An intuitive application of actively controlled phase shift is beam steering.^{45,360} Figure 18a(i) shows a schematic diagram of MIM metasurface with a dielectric layer involving GST sandwiched between the top Al strip and bottom Al blanket. Different phase shifts can be realized in the amorphous and crystalline states via tuning the width of the top aluminum strip.⁴⁵ Hence, by delicately designing the width of aluminum strip in each unit cell, the metasurface can switch between anomalous reflection ($\theta_r = 33.6^\circ$) in the amorphous phase (Figure 18a(ii)) and specular reflection in the crystalline phase (Figure 18a(iii)).

Vortex beams have huge potential to be applied in quantum information, encryptions, and optical communications. Conventional devices such as spatial light modulators (SLM) used to create vortex beams have the problem of huge volume, large unit cells, and limited bandwidth, which hinders its further applications.³⁶¹ The advent of metasurfaces offers a novel approach to the research of vectorial and vortex beam generation due to its freedom of phase design, miniaturization of footprint, and flexible manipulation.^{362–366} Furthermore, the combination of PCMs makes it possible to achieve the reconfigurable and switchable generation of vortex beam and photonic spin–orbit interactions (PSOIs).^{361,367–369} For example, tuning between symmetric and asymmetric PSOIs is demonstrated using a GST-based MIM metasurface (Figure 18b(i,ii)).³⁶⁷ In the amorphous state, the metasurfaces are only characterized by geometric phase (Pancharatnam–Berry phase, i.e., PB phase) of $-2\sigma\xi(x,y)$, resulting in symmetric PSOIs; while in the semicrystalline

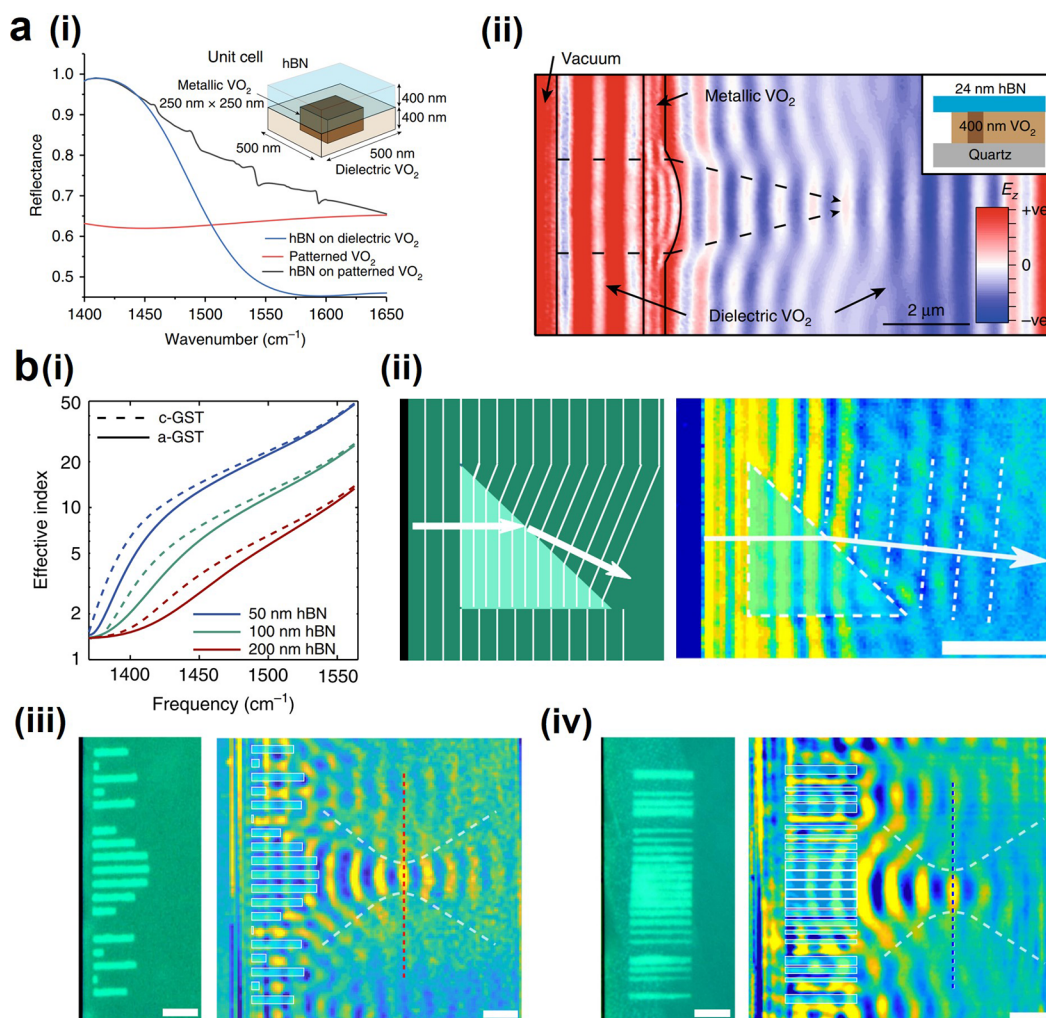


Figure 20. PCM for vdW polaritonic devices. (a) (i) A tunable polariton metasurface of hBN and VO₂. By patterning the VO₂ with metallic domains, we can excite a rewritable reflection profile, which cannot be generated from either of the materials alone. (ii) PhPs are launched by the hBN edge when light impinges on the sample. Because of the n_{eff} contrast between the background and the lens domains, the propagating PhP focusing outside on the focal plane.⁴⁴ Reproduced with permission from ref 44. Copyright 2018 The Author(s). (b) (i) Dispersion of PhPs for different hBN thicknesses on a-GST and c-GST. (ii) (left) Schematic of wavefronts for a rewritable polaritonic prism. The direct laser writing process is used to write and erase the prism pattern by selectively crystallizing or re-amorphizing GST. (right) The s-SNOM image of polaritonic prism showing a clear deflection angle of the outgoing PhP wavefronts. (iii) (left) Optical images of the written metalens 1. (right) The s-SNOM image of metalens 1 showing focusing of polaritons at 1452 cm⁻¹. (iv) (left) Optical images of the written metalens 2. (right) The s-SNOM image of metalens 2 at 1445 cm⁻¹.⁴² Reproduced with permission from ref 42. Copyright 2019 The Author(s).

state, an additional propagation phase of $\phi(x,y)$ is introduced to the PB phase. Under this condition, asymmetric coupling with independent control of two different spins (left-handed and right-handed circular polarization, i.e., LCP and RCP) can be achieved. When GST is fully crystallized, PSOs are switched off and only mirror reflection exists (Figure 18b(iii)). The switching ability of PSOs may provide an inspiring envision in optical encryptions and information security.

While plasmonics permits strong light–matter interactions in nanoscale, the optical loss of metal plasmon at optical frequencies limits the propagation lengths of SPPs and makes guiding light inefficient. Some integrated approaches have been developed by combining plasmonics with nanoscale photonics, which allow for both low-loss light delivery and strong light–matter interaction in a compact footprint.³⁷⁰ For example, Nikolaos et al. first demonstrated a plasmonic-phase-change memory cell integrated into a photonic waveguide (Figure 18c(i)). The memory device can be electrically or optically

switched between binary or multilevel states. As shown in Figure 18c(ii), one can reversibly regulate the intensity of the electrical field within the nanogap by switching between its highly resistive amorphous phase and conductive crystalline phase. Hence, the overall transmission of the device is largely modulated by the phase transition (Figure 18c(iii)). In addition, this device can also be simultaneously read out both optically and electrically, offering a new strategy for merging computing and communications technologies. This work integrated plasmonics, photonics, and electronics, providing an exciting outlook in the development of switchable and reconfigurable meta-devices.

4.4.3. Reversible Switching of Low-Loss and Highly Confined Polaritons. Thus far, most on-chip plasmonic devices are limited by their high optical loss and low light confinement. The high research interests have been changed to controlling low-loss PhPs in polar crystals and highly confined polaritons in vdW materials.²⁸ The same approach by employing PCM can also be used to actively control PhPs, for example, the

PCM such as GST on quartz as illustrated in Figure 19a. The bottom bulk polar substrate supports surface phonon polaritons (SPhPs). Li et al. demonstrated that a thin layer of GST on a quartz surface can dramatically squeeze the wavelength of SPhPs, while the local switching of the PCM after direct laser-writing structuring can create rewritable SPhP resonators (Figure 19a(i,ii)).³¹⁰ The scattering-type scanning near-field microscopes (s-SNOM) measured SPhPs wavelengths have been squeezed down to $(\lambda_0/50)$, which is three times smaller than previously reported SPhPs in bulk polar crystals. The V-shaped marker after writing can be clearly seen in AFM topographic image. At the frequency of 943 cm^{-1} , the permittivity of c-GST is larger than that of a-GST, causing a brighter optical signal. At the frequency of 1120 and 1127 cm^{-1} , SPhP fringes can be observed because of the negative permittivity of quartz (Figure 19a(iii)). This PCM enabled reversible optical switching of SPhP has inspired a large amount of studies of active polaritonic optics and meta-optics in many other polar and vdW materials.

Besides propagating mode, the localized resonance mode in a nanocavity can also be enhanced and regulated by combing PCM with polar crystals. Figure 19b(i) shows an Au planar cavity with a high Q factor (~ 150) fabricated on a thin film of GST deposited on a SiC substrate.³⁷¹ The enhanced highly confined SPhP resonance can be switched off by directly annealing the metasurface on a hot plate, which causes material crystallization (Figure 19b(ii)). All the above approaches toward advanced control on the propagation of ultraconfined polaritons empower unique opportunities for many nanocircuit functionalities, e.g., on-chip optical switching,⁶⁹ reconfigurable wavefront shaping,^{44,372} metasurface arrays,⁴² and polaritonic lensing nanodevices.⁴²

4.4.4. Phase Transition for van der Waals (vdWs) Polaritonic devices. The polaritons in vdW materials are highly tunable, for instance, suspending h-BN on substrates that are made of phase-change materials, examples of VO_2 (Figure 20a(i))^{44,373} and GST (Figure 20b(i)),⁴² the effective index ($n_{\text{eff}} = k_p/k_0$) of PhPs can be reduced by a factor of 25 simply by changing the substrate from dielectric to metallic behavior.³⁷² As a result, by mimicking conventional refractive optics and engineering the geometry of planar polaritonic elements (bottom PCM layers), in-plane practical functionalities such as polariton steering, prism, and lensing have been realized.^{42,44,372,374} One typical example is the polariton lensing⁴⁴ within an h-BN slab on VO_2 substrate. Because of the different n_{eff} of PhP modes on dielectric and metallic domains of the VO_2 , when PhP with low- $n_{\text{eff,d}}$ propagates to a high- $n_{\text{eff,m}}$ region with a convex interface, the n_{eff} difference between two mediated polaritons results in a gradual phase accumulation within the curved lens; hence, the transmitted PhP gets focused into a spot (Figure 20a(ii)). Such an approach requires locally heating the VO_2 into microscale polaritonic elements. However, this approach suffers from limitations because VO_2 's different phases cannot coexist at the same temperature, and thus in close spatial proximity as is desirable for the realization of polaritonic devices. Another strategy by utilizing PCM GST has been demonstrated experimentally, which can realize rewritable waveguides and refractive optical elements such as lenses, prisms, and metalenses for PhPs in hBN (Figure 20b). In experiments, a subwavelength laser spot was used to write and erase patterns on the GST films with high spatial resolution. One example is the polariton steering;⁴² due to the different n_{eff} of PhPs on amorphous or crystalline GST, the propagating PhP undergoes positive

refraction at the domain boundary (Figure 20b(ii)). Furthermore, by using GST as switchable meta-atoms, it is also possible to achieve planar meta-optics for polaritons. Because by utilizing direct laser writing, arbitrary patterns can be written, erased, and rewritten in the hBN-GST heterostructure. For instance, the elements in metalens-1 and metalens-2 are truncated c-GST waveguides defined in an a-GST environment. By varying the length (metalens 1) and width (metalens 2) of each element to create the hyperbolic phase profile, focusing effects have been achieved of the two designed metalenses (Figure 20b(iii) and (iv)). This approach can be readily combined with other polaritonic vdW materials and other phase-change materials,^{42,347} thereby enabling a whole range of deeply subwavelength and programmable polaritonic devices on-chip.

5. PHASE TRANSITION FOR THERMAL RADIATION

As discussed above, the dramatic change of complex permittivity can be exploited to a wealth of applications in tunable nanodevices via active modulation both on photons and polaritons, during which the optical spectra are modified. On the basis of Kirchhoff's law of thermal radiation, the emissivity of an arbitrary body in thermodynamic equilibrium is equal to the absorptivity in the IR region, that is, $\epsilon(\lambda) = \alpha(\lambda)$.^{26,375} Hence, an abrupt change of thermal emissivity is expected during phase transition. Taking advantage of the tunable thermal emissivity, different functionalities have been realized including thermal camouflage,^{47,96} anticounterfeiting,³⁷⁶ radiative cooling of buildings,³⁷⁷ and much more.^{30,378,379} Nevertheless, the dramatic variation of thermal properties can only happen around the phase change temperature, which hampers further applications of PCMs in a wide range of temperatures. One effective method to overcome this limitation is to alter the temperature of phase transition, for instance, through doping impurities.^{181,191,380–382} One notable example is doping tungsten in VO_2 to expand its applicable range of emissivity modulation.³⁸³ Recent advances on the W- VO_2 have been reported for a variety of functions, such as temperature-independent camouflage,²⁶ thermal imaging sensitizer,²⁹ as well as the radiative cooler.³¹

In this section, we first summarize the implementations of PCMs on thermal emissivity modulation and relative applications. Then, we introduce the doping method which modulates the phase transition point of VO_2 . The modified thermal properties in turn expand the applications of VO_2 , which are reviewed at last.

5.1. Phase Transition Based Thermal Emission Control

5.1.1. IR Camouflage. According to Kirchhoff's law of radiation,³⁷⁵ the spectral emissivity $\epsilon(\lambda)$ is equal to spectral absorptivity in thermodynamic equilibrium. The thermal radiance per unit angle is given by³⁸⁴

$$P_{\text{rad}}(T) = \int_0^\infty B(T, \lambda)\epsilon(\lambda) d\lambda \quad (4)$$

where $B(T, \lambda)$ is the spectral radiance of a blackbody. Therefore, the possibility of tailoring $\epsilon(\lambda)$ across phase transition allows for flexible tuning of $P_{\text{rad}}(T)$ below the blackbody counterpart. This artificial reduction of $P_{\text{rad}}(T)$ is the principle behind an IR camouflage, causing an apparent temperature captured by the IR camera to be lower than the actual temperature, thus concealing the target object in a colder background.

A typical PCM used for thermal camouflage is VO_2 . In the simplest case, a blanket layer of VO_2 is deposited on a substrate

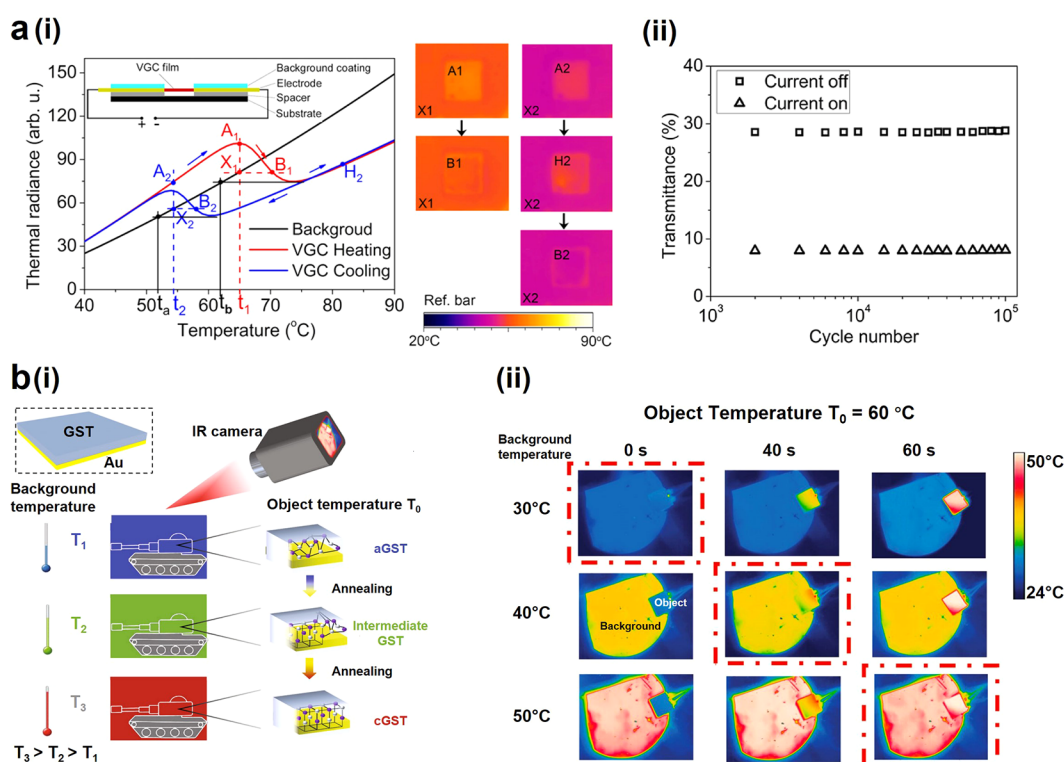


Figure 21. IR camouflage based on PCMs. (a) An adaptive thermal camouflage based on electrically heated VGC nanotechnology sandwich structure. (i) (left) The thermal radiance of the background coating (black line) and the VGC film (heating, red curve; cooling, blue curve). (inset) The structure of the electrically tunable VGC-based device. (right) Thermal images of camouflage processes by direct (A1–B1) and hysteretic (A2–H2–B2) heating strategies. (ii) Transmittance change of the VGC film over 100 000 cycles.⁹⁶ Reproduced with permission from ref 96. Copyright 2015 American Chemical Society. (b) Thermal camouflage based on GST film. (i) Schematic showing the thermal camouflage. Perfect camouflage can be achieved by changing the GST phase on a GST–Au bilayer film-covered tank surface. (ii) Thermal images of background and object at different temperatures and annealing times. The object is annealed at 200 °C for 0, 40, and 60 s to obtain various GST crystallization depths. The three conditions on the diagonal line show adaptive thermal camouflage at different temperatures.⁴⁷ Reproduced with permission from ref 47. Copyright 2018 The Author(s).

with high thermal absorption, such as sapphire, mica, or polymer materials. When VO_2 is in the insulator state, it is basically transparent to the thermal IR spectra with wavelength ranging from 5 to 20 μm , so the surface shows high absorption to thermal IR by the substrate material. When VO_2 switches to the metal state, the surface becomes much more reflective to IR³⁸⁵ because the plasmonic energy of free electrons in the metal state is ~ 1 eV,⁷⁶ much higher than the energy of thermal IR photons (~ 0.1 eV). Therefore, the thermal emissivity in the metal state is smaller than that in the insulator state, which is suitable for thermal camouflage. For instance, Xiao et al. fabricated an adaptive thermal camouflage system consisting of a VO_2 /graphene/CNT (VGC) sandwich structure.⁹⁶ Thanks to the great electrical conductivity of graphene/CNT substrate, it is efficient to use an electrothermal method to stimulate the phase transition. By using a layer of silver thermal glue (average emissivity ≈ 0.67) in a two-terminal current-controlled structure, the thermal camouflaging behavior of the VGC film is investigated (Figure 21a(i), inset). The thermal radiance of the surface demonstrates an abrupt decrease when the temperature rises above T_{MIT} , allowing regulation of the apparent IR temperature to the same as that of the background. For example, during the heating process, the detected temperature difference (ΔT_1) between the VGC film and the background decreases from 5.1 to 0.7 °C (the background remains at X1 point but the VGC film change from A1 to B1 point through heating). Also, the VGC film can blend into the

background when it is shifted from H2 to B2 point (Figure 21a(i)). The reliability of the VGC structure is also explored by measuring the transmittance change. It is shown that the nanotechnology sandwich structure design enables fast switching by electrical Joule heating, and the system exhibits excellent cyclability over 100 000 cycles (Figure 21a(ii)).

An alternative material for camouflage is the widely used PCM GST. In the MIR range from 6–14 μm , the average thermal emissivity increases dramatically due to the phase transition from amorphous (transparent) to crystalline (absorptive) state.⁴⁷ Therefore, GST film can be blended into the background with different temperatures by controlling its crystalline depth (Figure 21b(i)). Qu et al. demonstrated that the GST thin film can be used as an effective coating to achieve thermal camouflage from 30 to 50 °C via modulating its annealing time (Figure 21b(ii)).

5.1.2. Self-Adaptive Radiative Cooling. For a comfortable living environment for humans, more than half of the household energy is consumed on heating and cooling in countries like the United States.³⁸⁶ To cut this portion of energy consumption and reduce the greenhouse effect, the radiative heat exchange between households and the 3K outer space has been extensively investigated for an energy-free approach of building cooling.^{387–389} Daytime radiative cooling was developed in the past few years by using roof coatings with high thermal emissivity and low solar absorption.^{390–392} This technique with fixed, cooling-optimized properties, although

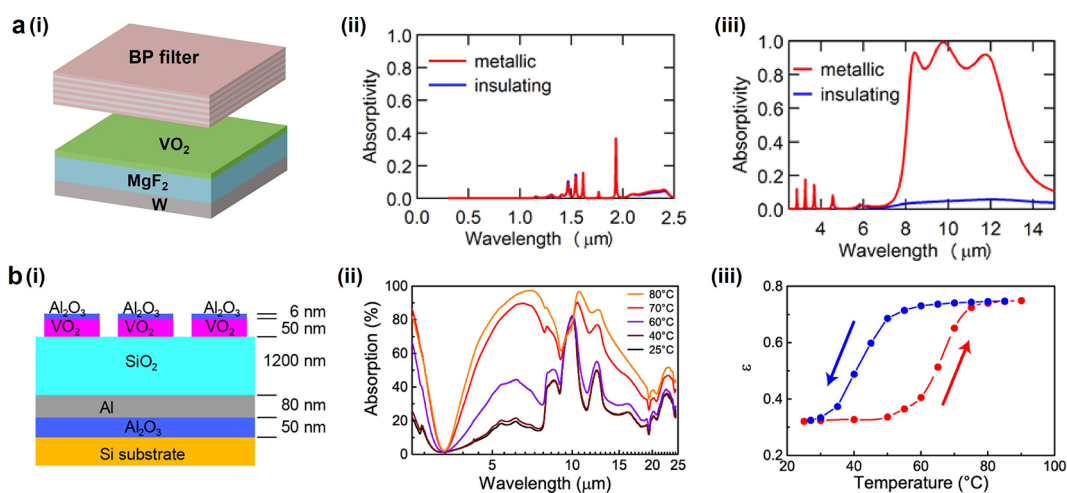


Figure 22. Self-adaptive radiative coolers based on VO₂. (a) A proposed Fabry–Perot cavity structure based on VO₂/MgF₂/W, which is integrated with the top bandpass filter. (i) Schematic of the combined system of the Fabry–Perot cavity and bandpass filter. (ii) Solar and mid-IR (iii) absorptivity for M and I states are calculated.³⁷⁷ Reproduced with permission from ref 377. Copyright 2018 Optical Society of America under the terms of the OSA Open Access Publishing Agreement. (b) A fabricated smart radiator by meta-surface of VO₂. (i) Schematic showing the proposed VO₂ based meta-surface for adaptive radiative cooling. (ii) Absorption spectra of the meta-reflector measured at 25, 40, 60, 70, and 80 °C. (iii) Emissivity change of the meta-reflector when the device is heated from 25 to 90 °C (blue) and then cooled down (red). A modulation magnitude of 0.43 can be measured for emissivity between the metal state and the insulator state.³⁹⁴ Reproduced with permission from ref 394. Copyright 2018 American Chemical Society.

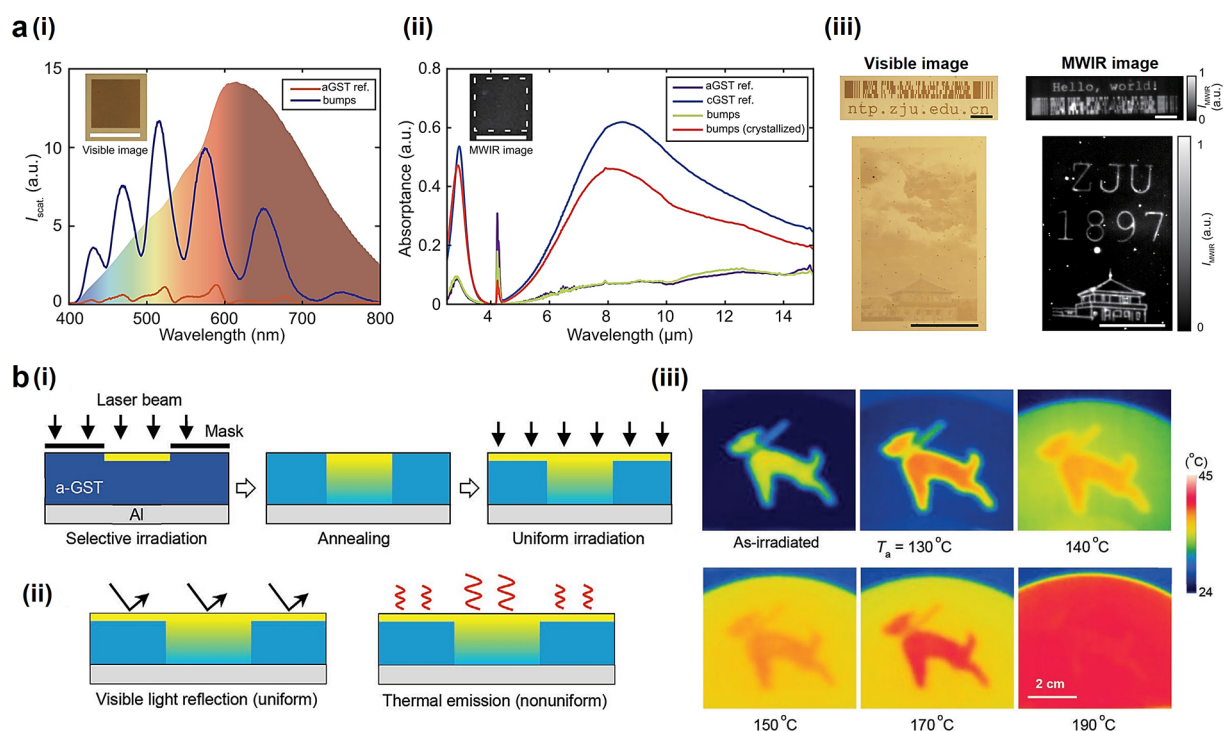


Figure 23. Dynamic spatial control of thermal emission. (a) Reconfigurable metasurface for pattern coding in visible and IR range in the overlapped region. (i) Scattering spectra in the visible band for original amorphous GST (red) and bumped (blue) region. Colored region: the illuminating spectrum of the white light source. Scale bar: 100 μm . (ii) Absorption spectra in IR band for the bump array (green), a-GST region (purple), c-GST reference (blue), and the bump array after crystallization (red). Scale bar: 100 μm . (iii) Visible and MWIR images of the binary anticounterfeiting label. Scale bar: 100 μm (top) and 500 μm (bottom).³⁷⁶ Reproduced with permission from ref 376. Copyright 2021 American Chemical Society. (b) Spatially controlled emitter using an expanded laser beam. (i) Schematic showing the printing process of the thermal pattern. (ii) Schematic showing that the pattern is invisible to the naked eye but can be recognized by IR camera. (iii) Thermal images of a “dog” pattern after annealing at different temperatures T_a .⁶⁰ Reproduced with permission from ref 60. Copyright 2022 Wiley-VCH.

successful in reducing the cooling energy in hot summer daytime, continues to efficiently radiate heat during cold nights and winter and thus increases the energy cost in heating. The issue of overcooling is a critical limitation for conventional static

thermal regulation.³⁹³ Therefore, it is a timely demand to develop a coating material with dynamic emissivity that automatically shuts off or reduces the radiative cooling power at low temperatures.

VO₂ is an ideal candidate for this dynamic emissivity property due to its temperature-driven MIT. Effective emissivity modulation can be achieved by integrating VO₂ with various optical resonant structures. The design of the Fabry–Perot cavity is a relatively simple approach to building a surface with high emissivity exclusively at high temperature based on the mechanism described in section 5.2. In 2018, Ono et al. proposed a self-adaptive radiative cooling design using the VO₂/MgF₂/W cavity structure (Figure 22a(i)).³⁷⁷ An 11-layer bandpass filter consisting of Ge/MgF₂ stack structure is integrated on the top surface of the reported cavity structure to eliminate the absorption in the solar wavelength range (Figure 22a(ii)). Theoretical calculations indicate a significant increase of the thermal emissivity in the MIR region driven by the insulator-to-metal transition of VO₂ (Figure 22a(iii)). Therefore, when the ambient temperature is higher than the critical point of phase transition, the adaptive radiative cooling is turned on with high emissivity. On the contrary, the radiative cooling will be much reduced when the ambient temperature is lower than the critical point.

In addition to the Fabry–Perot cavity, metamaterial surfaces can also enhance the emissivity of the metal state via plasmonic resonance of adjacent blocks. Sun et al. fabricated a smart radiator that consists of a bottom aluminum reflector, a SiO₂ spacer layer, and VO₂ block arrays (Figure 22b(i)).³⁹⁴ When the metasurface is heated from 25 to 80 °C, the absorptivity within the MIR range increases gradually (Figure 22b(ii)). The insulator state and metal state emissivity are measured at 25 and 90 °C, respectively, showing a modulation depth of $\epsilon_M - \epsilon_I = 0.43$ (Figure 22b(iii)).

5.1.3. Dynamic Spatial Control of Thermal Emission. In addition to the spectral control, how to spatially modulate thermal emission is another crucial yet challenging issue as it is highly demanded for information applications, such as IR target simulation,³⁹⁵ combat recognition,³⁹⁶ and encryption.³⁷⁶ To achieve active control of spatial patterning, many technologies have been proposed including utilizing thermoelectric method,^{397,398} light-sensitive materials,³⁹⁹ and metamaterial based on MEMS.³⁹⁶ Nevertheless, large thickness (~ 5 mm) is required in the thermoelectric devices; the modulation range of emissivity is very limited (~ 0.12) by using UV illumination to generate light-induced carrier; the MEMS-based metamaterial increases the complexity of fabrication. Consequently, spatially resolved active control of thermal emission for further applications is still elusive.

The advent of PCMs opens a new direction to realize reconfigurable and spatial control of thermal radiation.¹¹³ The phase transition of VO₂ at precise locations can be achieved through a highly focused laser spot, leading to spatially resolved emission control. Also, by controlling the duration of laser pulses, nine levels of thermal emission at the same temperature are demonstrated. However, maintaining the thermal pattern requires sustaining power supply to keep the sample at a desired temperature and the motif will be erased in about 9 s after removing the device from the heat stage. Recently, Xu et al. developed a nonvolatile reconfigurable metasurface with independent coding in both visible and IR range.³⁷⁶ The metasurface consist of a stack of Au/ZnS/GST and a capping layer. When illuminated by a focused high-power ns laser pulse, submicrometer-sized bumps are created due to the evaporation of GST, which can efficiently scatter the incident white light (Figure 23a(i)). Simultaneously, ms laser pulse can be focused to stimulate local crystallization, causing modulation of thermal

emissivity in the midwave infrared (MWIR, ~ 3 μm) and LWIR (~ 8.3 μm) regions (Figure 23a(ii)). Hence, simultaneously generating different patterns in visible and IR bands is achieved on the same sample, which can be used in practical applications such as optical data storage, encryption, and anticounterfeiting (Figure 23a(iii)).

One possible limitation of the method discussed above is the requirement of a tightly focused laser source, which blocks its scalability for further applications. To this end, spatial thermal emission control via an expanded beam is demonstrated by Kim et al.⁶⁰ First, the GST film is illuminated by a spatially modulated laser beam and then annealed at an appropriate temperature. Then the GST layer is irradiated uniformly, which causes crystallization (Figure 23b(i)). As the reflectance in visible light only depends on the near-surface structure, the pattern cannot be recognized by the naked eye. However, the measured emission of a film is affected by the ratio of the thickness between the crystalline and amorphous states. Therefore, the designed pattern can be captured by an IR camera (Figure 23b(ii)). To illustrate, thermal images of a “dog” figure are obtained by annealing the sample at different temperatures T_a (Figure 23b(iii)). It can be noticed that the overall emissivity of the sample increases with the value of T_a , which is due to the improved proportion of materials in the crystalline state. Furthermore, when the sample is annealed at 190 °C, the color contrast fades away because it is fully crystallized.

5.2. Thermal Properties and Applications of W-doped VO₂ (W-VO₂)

With the dramatic change of thermal emissivity across the MIT at $T_{\text{MIT}} = 67$ °C, VO₂ has been widely used for dynamic thermal radiation control.¹² As we discussed above, the modulation of thermal emissivity roots from the optical property changes during the phase transition, which causes the regulation of absorptivity in the IR range. In the metallic state, the complex permittivity of VO₂ is expressed by the Drude model as^{385,400}

$$\epsilon = \epsilon_{\infty} - \frac{\omega_p^2}{\omega^2 + i\omega\Gamma} \quad (5)$$

where ω , ϵ_{∞} , ω_p , and Γ represent the angular frequency, the high-frequency dielectric constant, the plasma and the collision frequency, respectively. In the insulating state, VO₂ is a dielectric medium and the permittivity is usually described by the Lorentz model as⁴⁰⁰

$$\epsilon_i = \epsilon_{\infty} + \sum_{j=1}^N \frac{S_j \omega_p^2}{\omega_j^2 - i\omega\gamma_j - \omega^2} \quad (6)$$

where ω_p , S_j , j , and γ_j refer to phonon vibration frequency, the oscillation strength, the phonon mode index, and the scattering rate, respectively.

However, the thermal conductivity of VO₂ was found to show only insignificant variation across its MIT, limiting its thermal conduction applications in a wider temperature range.³⁸¹ One possible method to deal with this problem is to adjust its phase transition temperature via doping impurities. For example, T_{MIT} of VO₂ can be effectively lowered down to -100 °C through doping tungsten (W) following $dT_{\text{MIT}}/dx = -25$ °C, in which x is the atomic fraction of the W dopant.^{380,381,401} The ability to regulate the thermal properties of VO₂ expands its application range in the field of optics, information technology, and energy. Examples of such applications include IR camouflage, thermal

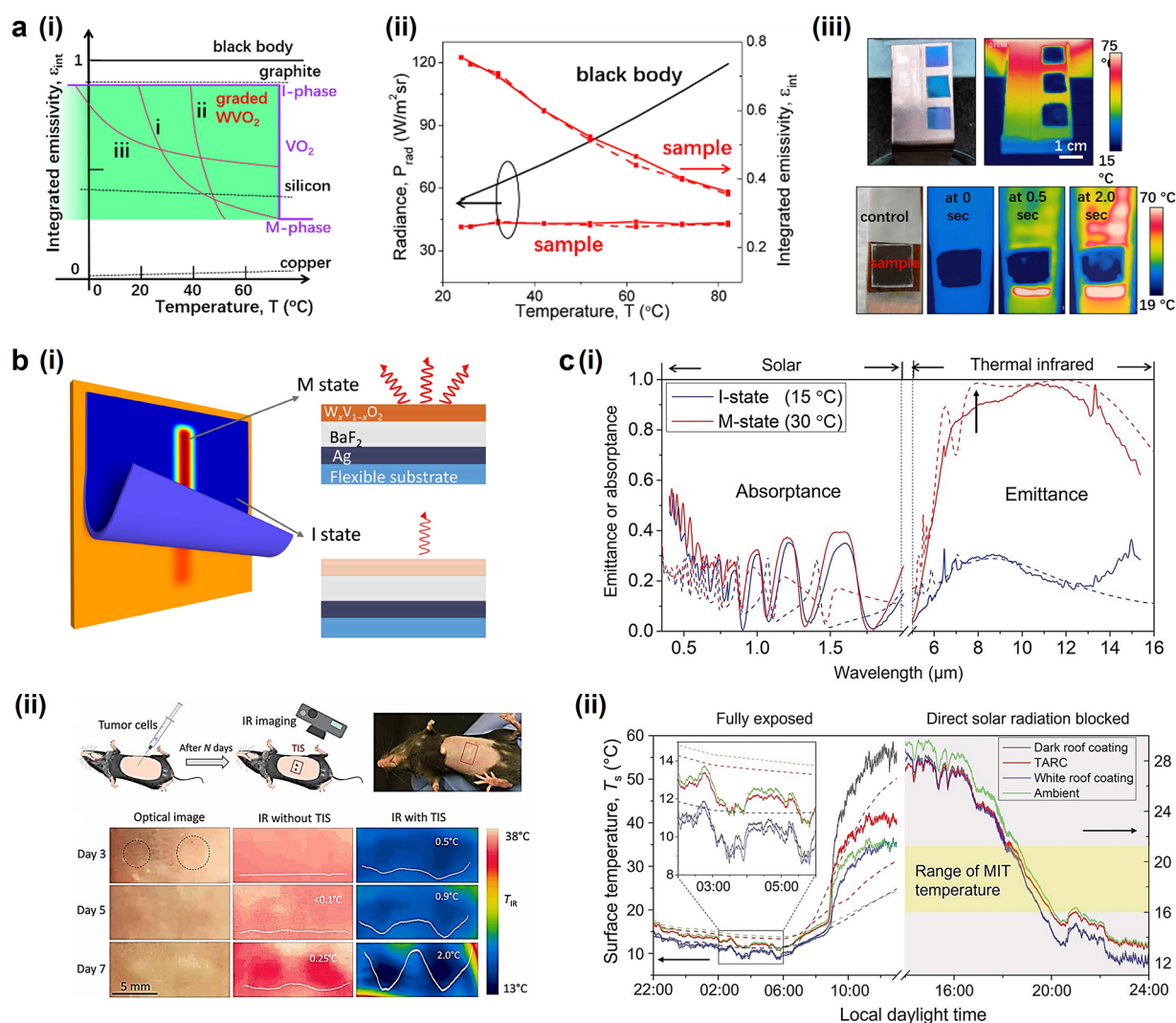


Figure 24. Thermal applications of $W\text{-VO}_2$. (a) A thermal radiance modulation platform for advanced camouflage applications. (i) Schematics illustrating arbitrary realization of $\epsilon(T)$ by graded doped $W\text{-VO}_2$. (ii) Design of the $\epsilon(T)$ to counteract the T^4 law, generating a temperature-independent thermal radiation power. (iii) Experiments demonstrating immunity of the camouflage to large spatial variation and a temporal surge of the surface temperature.²⁶ Reproduced with permission from ref 26. Copyright 2020 Wiley-VCH. (b) TIS based on $W\text{-VO}_2$. (i) Schematic illustration of boosted temperature resolution of thermography by TIS and its working mechanism. (ii) TIS applied to medical thermography, revealing early stage tumors that are otherwise undetectable by conventional methods.²⁹ Reproduced with permission from ref 29. Copyright 2020 The Authors. (c) A TARC for all-season household thermal regulation. (i) Solar spectral absorbance and part of the thermal spectral emissivity of TARC at I-state and M-state. (ii) Surface temperature of a TARC, a commercial dark roof coating ($A = 0.70$, $\epsilon_w = 0.90$) and a commercial white roof coating ($A = 0.15$, $\epsilon_w = 0.90$) in an open-space outdoor environment recorded over a day–night cycle.³¹ Reproduced with permission from ref 31. Copyright 2021 The American Association for the Advancement of Science.

imaging sensitizers, and temperature-adaptive radiative coolers, which will be discussed separately in the following subsections.

The formation of $W_xV_{1-x}O_2$ alloy provides a new opportunity to regulate T_{MIT} effectively. For instance, Liu et al. used aqueous sol–gel method to process thin VO_2 films with W doping ratio up to 4%.³⁸⁰ A consistent decrease of T_{MIT} was observed with an increase in W doping ratio, and emissivity modulation is available at lower temperatures down to 30 °C. In another work, Mao et al. prepared a thermochromic $W\text{-VO}_2$ coating on cotton fabrics, demonstrating its potential for practical IR stealth applications.⁴⁰¹ However, most IR camouflage based on $W\text{-VO}_2$ is active that requires external heating for emissivity modulation. Pixelated energy inputs are needed for the operation of such camouflage, which is typically limited to objects with uniform and slow-varying temperature profiles. In light of this limitation, Tang et al. developed a novel, energy-free IR camouflage using a

meta-material platform with graded doped W doping in VO_2 .²⁶ By judiciously designing the W profile, the temperature dependence of integrated emissivity $\epsilon(T)$ can be engineered in a nearly arbitrary manner near room temperature, and unprecedented manipulation of IR radiance can be achieved (Figure 24a(i)). When $\epsilon(T)$ is programmed as inversely proportional to T ,⁴ thermal radiance from the surface becomes temperature independent (Figure 24a(ii)), leading to the development of a unique camouflage that is mechanically flexible, power-free, and immune to spatial and temporal perturbations (Figure 24a(iii)). Furthermore, an IR decoy based on the material platform is demonstrated, which can intentionally deceive the IR camera with a counterfeited image, achieving a more advanced stage of counter-IR detection.

The MIT of VO_2 can be utilized to develop another application named TIS, which is based on the same principle

of thermal radiance modulation, while the temperature dependence of emissivity is engineered to be positive rather than negative as in the case of camouflage. In IR imaging, the temperature reading (T_{IR}) is obtained by assuming that the object surface has a constant wavelength-integrated emissivity (ϵ_0). For a general case, the T_{IR} deviates from the actual temperature T via $P_{\text{rad}} = \epsilon_0 \sigma T_{\text{IR}}^4 = \epsilon \sigma T^4$, in which ϵ is the actual emissivity of the surface. The deviation can be shown from the equation:

$$\frac{dT_{\text{IR}}}{dT} = \left(\frac{\epsilon}{\epsilon_0}\right)^{1/4} \left(1 + \frac{1}{4} \frac{d \ln \epsilon}{d \ln T}\right) \quad (7)$$

and this differentiation would be equal to $(\epsilon/\epsilon_0)^{1/4}$ for conventional materials with T -independent ϵ .⁴⁰² In contrast, if ϵ can be engineered to have a strong and positive dependence on T , the large $d \ln \epsilon/d \ln T$ would contribute to a significant amplification of dT_{IR}/dT , thus enhancing the sensitivity of thermal imaging.

The desired T -dependence of ϵ can be realized by combining the MIT property of VO_2 with a Fabry–Perot cavity structure. This photonic structure consists of an IR transparent dielectric layer (spacer) sandwiched between a bottom metal mirror and a top VO_2 layer. The top VO_2 layer is typically thinner than 50 nm. The thickness of the dielectric spacer d follows the equation⁴⁰³

$$d = \frac{N\lambda}{4n} \quad (8)$$

in which λ , n , and N represent the resonance wavelength (8–13 μm for thermal IR), the refractive index of the spacer and an odd integer, respectively. The insulating state of VO_2 is transparent to thermal IR, and incoming IR radiation will be reflected by the bottom metal mirror with little absorption. In contrast, when the VO_2 switches to the metal state, a photonic resonance peak at a wavelength between 8 and 13 μm will form in the cavity structure, greatly enhancing IR absorption. This abrupt increase of the absorption by MIT indicates strong and positive T -dependence of ϵ according to Kirchhoff's law of radiation.

Although many previous works have theoretically and experimentally demonstrated this VO_2 -based photonic structures,^{377,404,405} the study is limited to material and optical property characterization, with little relevant to the application of TIS. Such an idea was first proposed and experimentally realized by Tang et al., and an unprecedented 15 times refinement of thermal sensitivity was achieved based on a $\text{W-VO}_2/\text{BaF}_2/\text{Ag}$ structure (Figure 24b(i)).²⁹ Two key techniques were developed as an indispensable support to this innovated application: One is the fabrication of the nanoscale photonic resonance structure on thin flexible substrates instead of thick rigid ones, allowing attachability of the membrane to the target surface and quick surface temperature equilibration; the other is the delicate engineering of MIT temperature via W doping, which effectively adapts the MIT temperature (e.g., to human skin temperature) depending on the scenario of the applications. TIS enables noise equivalent differential temperature (NEDT) down to 3 mK in an uncooled bolometer for the first time. This millikelvin NEDT breaks the long-existing bottleneck in bolometer sensitivity²⁹ and greatly improves imaging quality. Many promising applications based on TIS, including in operando electrical analysis, early stage cancer screening, and building structure defects detection were demonstrated (Figure 24b(ii)).

As we discussed in section 5.1.2, nanocavities and metasurfaces based on VO_2 have been reported for adaptive radiative cooling.^{377,394} These preliminary works indicate the feasibility of self-adaptive emissivity switching based on the MIT of VO_2 . However, such studies are either purely theoretical or mostly limited to material property characterization, lacking focus to develop and test the technology for practical applications. Several issues need to be addressed for actual household thermal regulation. First, the emissivity contrast between the insulating state and metallic state is typically 0.3–0.5, which should be improved for more effective radiative power management. Second, the solar absorption property is a critical factor that needs to be optimized for all-season energy reduction, while this issue is either overlooked or not satisfactorily solved in existing works. The solar absorption, if not optimized, would overwhelm the radiative cooling effect. Third, to regulate the building temperature close to the human comfort zone, the emissivity switching temperature needs to be set at around 22 °C, which cannot be achieved using VO_2 due to its MIT temperature at 67 °C. Lastly, existing dynamic radiative coolers are mostly produced on small and rigid substrates like Si, while the development of a new fabrication process for high production scalability and mechanical flexibility is clearly needed for practical rooftop applications.

In this regard, Tang et al. recently made a major breakthrough in the realization of a temperature-adaptive radiative coating (TARC), effectively addressing all of the above issues and advancing the technology close to practical household applications.³¹ By integrating W doped VO_2 with a plasmonic enhanced metamaterial design, the thermal emissivity of TARC automatically switches from 0.20 for ambient temperatures lower than 15 °C to 0.90 for temperatures above 30 °C. From a holistic perspective of energy saving through the year, the solar absorption coefficient of TARC is optimized to around 0.25, which maximizes the source energy saving for most climates (Figure 24c(i)). The capability of TARC to self-adaptively modulate radiative power is fully characterized both in a cryogen cooled vacuum chamber and in an actual outdoor environment. The outdoor tested surface temperature regulation results of TARC are highly consistent with theoretical calculations based on physical modeling and the local weather database (Figure 24c(ii)). Simulations show TARC saves more energy than all existing roof coatings in most climates, especially those with strong seasonal variations. In addition, TARC was produced with high mechanical flexibility, can be upgraded to achieve high durability, and is promising for large-scale production. The wide application of TARC will notably benefit energy savings and environmental preservation by cutting greenhouse gas emissions.

6. CONCLUSION REMARKS AND OUTLOOK

In this review, we focus on research of TMO and chalcogenide PCMs, including their material chemistry and physics and related applications in the nanotechnologies. Because of their exotic characteristics including multiple excitation methods, fast switching, and dramatic change of physical properties, PCMs have been proved to achieve dynamically tunable nanodevices in electronics, nanophotonics, and thermotics. The basis for all applications is the dramatic change in physical properties (e.g., electrical conductivity, dielectric constant, and thermal emissivity) across the phase transition. Similar to their industrial applications in earlier optical storage (e.g., CD, DVD, blu-ray disks, and HD DVD), electrical nonvolatile memories have been

developed based on the electrical resistance contrast of chalcogenide PCMs. The technology to stepwise control the crystallization/amorphization process further lays the foundation for its construction of neural network devices. In nanophotonics, PCMs can be embedded in various metasurfaces and metamaterials to achieve multifunctionality via both phase and intensity control. Additional functionalities and novel integrated devices can be obtained by designing the nanostructures and precisely controlling the degree and the spatial location of phase transition. While the PCMs can be exploited to modulate the thermal radiation spectrally or spatially, wider applications including imaging sensitizer and temperature-independent thermal camouflage can be realized by regulating the T_{MIT} of VO_2 . In the following, we outlook the challenges and next-step developments of PCMs for multiphysical nanotechnologies.

6.1. Future Tunable Electronic Devices

With the ability of nonvolatility, lower power consumption, high thermal reliability, and cyclability, nonvolatile memories based on chalcogenides have been demonstrated, providing a new way to break through the bottleneck of current computing architecture. However, during the process of device design and optimization, some parameters may conflict with each other. For example, data retention temperature can be improved by doping PCMs with impurities, which however causes an increase in crystallization temperature, leading to a longer switching time to accumulate the increased activation energy.⁵⁵ One potential solution is exploiting growth-based materials rather than nucleation-based materials. Alternatively, using heterostructures instead of homogeneous alloy in memory cells can introduce additional interface energy generated by the interface layer, which can also help improve the crystallization speed. Besides, the interface between two different materials in heterostructures can prevent atomic diffusion in the amorphous state, which contributes to lower resistance drift. As for the issue of power consumption, most attention is focused on the RESET process due to the high amplitude required for material melting. In section 3.2.3, we summarized several novel designs with smaller BEC to reduce the RESET current. Nevertheless, it has been claimed that the lower contact size can result in a high RESET current density, which is not desired for industrial applications.⁴⁰⁶ Therefore, how to balance these device performances and produce remarkable PCM nonvolatile memories still needs to be explored in future studies.

Applying electrical pulses in various manners makes it possible to realize a gradual crystallization/amorphization process, causing chalcogenides to be a promising candidate for neuromorphic and arithmetical devices. The fundamental requirements for a perfect electronic device for computing tasks are fast, reliable, accurate, scalable, and have low power consumption.⁵⁸ Fast and reliable switching for data storage has been demonstrated in NVM applications. The PCM-based memory cells can switch in subnanoseconds and retain information for more than 10 years. Moreover, after decades of intense investigation, PCMs have become the most mature technology, and some manufacturing companies have paid continuous attention to developing chips based on PCMs. These endeavors promote the integration of PCMs with today's complementary metal-oxide semiconductor (CMOS) technology for scalable production, which also decreases the cost. As in the early stage, two crucial problems are important for further development of electrical neuromorphic devices. First, the

electrical resistance drops suddenly, leading to a nonlinear change in different intermediate states. This may be solved by screening appropriate dopants to modulate material fragility.⁵⁸ Alternatively, this problem can be tackled by slowing down the amorphization process and choosing a suitable initial level.³⁶ In addition, ultralow resistance drift is also needed for accurate operations. Introducing appropriate impurities and SLL structures have been proved to be effective ways to reduce drift,^{181,196,243,247} and it is expected to realize further modulation on the aging process and even achieve rejuvenation.⁴⁰⁷

6.2. Reconfigurable Active Nanophotonics

The high contrast of dielectric constant before and after phase transition provides an effective way to dynamically modulate the phase, intensity, and polarization of light at the nanoscale. To date, many reconfigurable active metasurfaces and metamaterials with multiple functionalities have been presented.^{25,281} In addition, benefiting from the highly confined property of SPPs, more applications have been realized such as tunable nano-antenna,³⁵⁰ color display,⁴³ beam steering,⁴⁵ OAM modulation,³⁶⁷ nonvolatile photonic memory,³⁷⁰ and so on. While SPPs face the problem of intrinsic optical loss due to Joule heat, strongly confined PhPs in polar crystals emerge as a counterpart with low loss and longer lifetimes.^{308–311} Therefore, more tunable complex functionalities in the IR spectrum are anticipated to be realized by integrating PCMs with PhPs.

For tunable metasurfaces and metamaterials, future research direction is to realize in situ, pixel-by-pixel control of the amplitude and phase either via electrical^{282,350} or optical^{25,281} switching method, which can provide large freedom for multifunctionality design. In this regard, the visible spectrum is the most challenging waveband.³⁵⁷ One reason is the resonant damping rooting from both plasmonic and dielectric losses from PCMs, which may affect the device efficiency and phase coverage. Besides, the geometrical parameters of nanostructures are typically small due to the short operation wavelength, causing the difficulty of focusing the laser spot small enough for pixel-by-pixel switching. To solve these problems, research on novel PCMs with low loss should be a potential direction for future work.¹³⁵ Another approach is to decrease the thickness of the PCM. What is more, developing electrically addressable metasurfaces could be a promising approach to promote the realization of pixel-by-pixel switching.

Until now, the tunability of PCM-based metadevices has been mostly limited to optical writing and thermal annealing. Now, the electrically driven tunable metasurface is technologically important because it enables the development of more convenient, miniaturized, and electrically controlled reconfigurable optical functionalities. However, there are still some challenges of electrically driven PCM-based metasurface: (1) The bottom integrated resistive microheater forbids operation in the transmission regime, which may be limiting for some applications. (2) Although the crystallization process requires a long low-voltage pulse through Joule heating, a short high voltage is required to reamorphize the PCM through melt-quench process. Creating such pulses is not achievable in small electronic devices which limit their possible applications. (3) The integrated photonic metadevices and metasurfaces require independent control of all unit cells; however, the electrical tuning of these unit cells is quite hard due to challenges such as heat crosstalk between neighboring unit cells and complicated and sophisticated circuitry are required to provide such short high voltage for many unit cells. (4) Another important

limitation on electrical tuning of such metadevices would be high power consumption and heat generation, which are not ideal conditions for many consumer electronics.

So far, the majority of research on PCMs is in the UV, visible, and infrared spectrum. This is due to the large refractive index change of these materials in these spectrum ranges. Another reason could be huge interest of industry and researchers in the novel applications in these spectra, such as optical communication, waveguides, sensors for gas detections, optical displays, holograms, and much more. However, the use of these materials in terahertz and microwave spectrum is an attractive topic that could be investigated.^{408–410}

In terms of integrated photonic devices, the research focus is now shifting toward all-optical neuromorphic devices, the ultimate object of which is to produce large-scale compact photonic neural networks for data storage and computing tasks.^{411–414} The advantages of ultrafast speed, parallelism, broad bandwidth, and low loss make the optical approach appropriate for implementations for hardware construction of neural networks. Although the development of ONNs is still in its early stage, PCMs are very promising for photonic neuromorphic computing due to their large contrast, multilevel control, and nonvolatility. However, some challenges still need to be addressed, such as the integration between the light sources and on-chip devices, implantation of PCM patches array on the electrode array, and the design of the electrically/optically driven and addressable techniques. Future development of integrated tunable devices requires the advancement of all the fields relating to optical nanodevices, including on-chip micro-/nanolasers, transparent electrical electrodes, high power supply with a small footprint, and the novel PCMs with low power consumption.

On all accounts, dynamic reconfigurable nanophotonic devices should meet the requirement of fast switching, high endurance and stability, lower power consumption, and good cyclability for practical applications and large-scale production. However, only a few works demonstrated reversible switching over multiple cycles,^{45,351,370,415} and the cyclability of PCM-based active photonic devices needs to be explored and verified in depth. Toward practical applications, more device performances including stability, efficiency, reliability, and power consumption are suggested to be investigated in terms of materials evolution and optimization of the practicable device in the future.

6.3. Dynamic Thermal Radiation Control

In the thermal IR spectrum, the thermal emissivity can have drastic variation during the phase transition, leading to the realization of various functions such as thermal camouflage,^{47,96} anticounterfeiting,³⁷⁶ radiative cooling of buildings,³⁷⁷ and much more.^{30,378} However, the thermal radiation modulation that only occurs near the phase transition point blocks its further applications to a wide range of temperatures. Besides, for some specific applications such as thermal camouflage, a continuous power supply is needed to sustain the VO₂ sample at the desired temperature, which is power-hungry.⁹⁶ The emergence of doping in PCMs to modulate their thermal properties has opened new horizons to break these limitations. T_{MIT} of VO₂ can be effectively decreased to -100 °C via doping.^{380,381,401} Furthermore, by judiciously designing the dopant profile in VO₂ films, the integrated emissivity $\epsilon(T)$ as a function of temperature can be nearly arbitrarily modulated around room temperature (e.g., inversely proportional to T^4 or positively dependent on T),

leading to more fascinating functionalities including temperature-independent thermal camouflage, thermal decoy, and TIS.^{26,29} For future developments, more materials such as conventional GST and other chalcogenides could be investigated following the doping method. Because of their sharp transformation and nonvolatility, these materials with modulated thermal emissivity may have the potential to be exploited in more fields such as high-temperature IR camouflage and thermal signal processing.⁴¹⁶

In addition, a tightly focused laser can be used to precisely control the position and depth of phase transition, enabling spatially resolved, dynamic multilevel control of thermal radiation.^{113,376} As the coded patterns are only visible in the IR region, this reconfigurable thermal coding technology is promising for energy harvesting, thermal management,^{416–418} and encryption.⁴¹⁹ Furthermore, the independent tunability with dual-mode in the visible and IR bands further improves the information density, which is potential to ulteriorly extend the applications in anticounterfeiting, camouflage,^{420–422} and thermal data storage.

AUTHOR INFORMATION

Corresponding Author

Cheng-Wei Qiu – Department of Electrical and Computer Engineering, National University of Singapore, Singapore 117583, Singapore; orcid.org/0000-0002-6605-500X; Email: eleqc@nus.edu.sg

Authors

Chunqi Zheng – Department of Electrical and Computer Engineering, National University of Singapore, Singapore 117583, Singapore; NUS Graduate School, National University of Singapore, Singapore 119077, Singapore

Robert E. Simpson – Engineering Product Development, Singapore University of Technology and Design (SUTD), Singapore 487372, Singapore

Kechao Tang – Key Laboratory of Microelectronic Devices and Circuits (MOE), School of Integrated Circuits, Peking University, Beijing 100871, China

Yujie Ke – Engineering Product Development, Singapore University of Technology and Design (SUTD), Singapore 487372, Singapore

Arash Nemati – Institute of Materials Research and Engineering, Agency for Science, Technology and Research (A*STAR), Singapore 138634, Singapore

Qing Zhang – School of Physics, University of Electronic Science and Technology of China, Chengdu 611731, China

Guangwei Hu – Department of Electrical and Computer Engineering, National University of Singapore, Singapore 117583, Singapore; orcid.org/0000-0002-3023-9632

Chengkuo Lee – Department of Electrical and Computer Engineering, National University of Singapore, Singapore 117583, Singapore; orcid.org/0000-0002-8886-3649

Jinghua Teng – Institute of Materials Research and Engineering, Agency for Science, Technology and Research (A*STAR), Singapore 138634, Singapore; orcid.org/0000-0001-5331-3092

Joel K.W. Yang – Engineering Product Development, Singapore University of Technology and Design (SUTD), Singapore 487372, Singapore; Institute of Materials Research and Engineering, Agency for Science, Technology and Research (A*STAR), Singapore 138634, Singapore; orcid.org/0000-0003-3301-1040

Junqiao Wu – Department of Materials Science and Engineering, University of California, Berkeley, and Lawrence Berkeley National Laboratory, California 94720, United States; orcid.org/0000-0002-1498-0148

Complete contact information is available at:
<https://pubs.acs.org/10.1021/acs.chemrev.2c00171>

Author Contributions

C.Z., R.E.S., and K.T. contributed equally to this work. C.W.Q. conceived and initiated the ideas of this collaborative work, and supervised the project overall. All authors contribute significantly to the paper.

Notes

The authors declare no competing financial interest.

Biographies

Chunqi Zheng is a Ph.D. student in the Department of Electrical and Computer Engineering at the National University of Singapore. She received her B. Eng. degree in Optoelectronics Information Science and Engineering from Zhejiang University (2017). Then she participated in the joint Master program and obtained the M.Sc. degree with distinction in Optics & Photonics from Imperial College London and M.Eng. in Optical Engineering from Zhejiang University. Her current research interests include light–matter interactions and light modulation at nanoscale such as polaritonics, PCM-based metasurfaces, and the topological transitions in photonics.

Robert E. Simpson is an Associate Professor within the Engineering Product Development Pillar and codirector of the Innovation by Design program at the Singapore University of Technology and Design (SUTD). Robert is also an Associate Editor for the Optical Society of America (OSA) Journal, *Optical Materials Express*. Robert received his Ph.D. from the Optoelectronics Research Centre (ORC) at the University of Southampton in the UK in 2008. After his Ph.D., Robert was awarded Marie Curie and Japanese Society for the Promotion of Science (JSPS) fellowships. His JSPS fellowship was spent at the Japanese National Institute for Applied Industrial Science and Technology (AIST), where Robert researched phase change data storage materials. Whilst the Marie Curie fellowship was held at the Institute of Photonic Sciences (ICFO) in Barcelona, where he developed phase change material-tunable photonics devices. In 2012, Robert formed the Advanced Chalcogenides Technologies & Applications Lab (www.actalab.com) at SUTD. ACTA lab's remit is to exploit the exotic properties of chalcogenide materials to design high performance electronics, photonics, and sensing devices.

Kechao Tang is currently an assistant professor in the Department of Integrated Circuits, Peking University, China. He received his B.S. degree from Peking University, China, in 2012, and his Ph.D. degree from Stanford University, USA, in 2017. Dr. Tang worked as a postdoctoral researcher in University of California, Berkeley, USA, from 2017 to 2020. His current research interest includes emerging nonvolatile memory devices, especially ferroelectrics memories based on hafnium oxide and phase transition materials for novel electrical applications. Dr. Tang has authored more than 50 papers in scientific journals and conferences including *Science*, *Science Advances*, *Advanced Materials*, and IEEE IEDM etc., with a total citation over 2200. He serves as a guest editor for the international journal *Frontiers of Neuroscience*. He is a recipient of 2018 Chinese Government Award for Outstanding Self-financed Students Abroad, 2017 Stanford University Robert A. Huggins Award, and 2014 Stanford University Hewlett-Packard Award.

Yujie Ke is a research fellow at the Singapore University of Technology and Design (SUTD). He received his Ph.D. from Nanyang Technological University (NTU) in 2019 and his master's degree from the University at Buffalo (SUNY-Buffalo) in 2015. Before joining SUTD, he has been working in NTU as a research fellow for ~2 years. He is interested in nanofabrication, 3D printing, phase-changed materials, plasmonics and photonic crystals, mechanical reconfigurable structures, mechano-/thermochromics, and related applications.

Arash Nemati received his B.S. degree at University of Mazandaran (2011), Iran, M.S. degree at Babol Noshirvani University of Technology (2014), Iran, and Ph.D. at the National University of Singapore (2020), Singapore, supported by Singapore International Graduate Award (SINGA) scholarship from A*STAR. He joined A*STAR in 2020 as a scientist I. His current research interests include active and passive metasurfaces and their applications in optics and nanophotonics.

Qing Zhang received his M.S. (2013) degree in optical information science and technology from University of Electronic Science and Technology of China (UESTC), Chengdu, China. He obtained his Ph.D. (2019) degree in optical engineering from the China Academy of Engineering Physics, Mianyang, China. He worked as a postdoctoral fellow at National University of Singapore from 2019 to 2021. Currently, he is an associate professor at the Department of Physics, UESTC. His research interests include nanophotonics, light–matter interactions in hybrid systems with metasurfaces and 2D materials, and controlling polaritons in van der Waals materials.

Guangwei Hu finished his Ph.D. in the Department of Electrical and Computer Engineering, National University of Singapore, and obtained a B.Sc. from the Department of Applied Physics in Harbin Institute of Technology, China, in 2016. His current research interests include fundamental light–matter interactions at nanoscale with promising applications such as the multifunctional electromagnetic metamaterials and metasurfaces, the optical engineering of 2D materials, polaritonics (plasmon, phonon, and exciton), and topological transitions in photonics, among many others.

Chengkuo Lee received his Ph.D. degree from The University of Tokyo, Tokyo, Japan, in 1996. Currently, he is the director of the Center for Intelligent Sensors and MEMS and the Global Foundries Chair Professor in Engineering at the National University of Singapore, Singapore. He cofounded Asia Pacific Microsystems, Inc. (APM) in 2001, where he was Vice President of R&D from 2001 to 2005. From 2006 to 2009, he was a Senior Member of the Technical Staff at the Institute of Microelectronics (IME), A-STAR, Singapore. His research interests include Mid IR Photonics, Metamaterials, Sensors, and AIoT.

Jinghua Teng is a Principal Scientist and Senior Group Leader in the Institute of Materials Research and Engineering (IMRE), A*STAR, and an Adjunct Professor in the Nanyang Technological University, Singapore. He has published over 230 journal papers and filed 29 primary patents. He is a Fellow of SPIE and an editorial board member of the *Journal of Optics*, *Optoelectronic Advances*, *Photonix*, *Journal of Molecular and Engineering Materials*, and A*STAR Research Publications. His research interests include nanophotonics, metamaterials, and metasurfaces, 2D optoelectronics, plasmonics, THz technology, and semiconductor materials and devices.

Joel K. W. Yang received his Master of Science (2005) and Ph.D. (2009) degrees from the Massachusetts Institute of Technology, Department of Electrical Engineering and Computer Science. He is Provost's Chair Professor and Associate Professor in the Engineering Product Development pillar at Singapore University of Technology and Design (SUTD) and holds a joint appointment as Principal Scientist I at the Institute of Materials Research and Engineering (IMRE) of

A*STAR. He is recognized for pioneering work in plasmonic color printing, achieving record-level printing resolution at 100 000 dpi and for the widely used “salty-developer” to improve the resolution of electron beam lithography. His research interests include Nanoplasmonics, 2D and 3D printed nano optical design elements (NODE), and sub-10 nm resolution lithography. He serves as Associate Editor of *Science Advances*, *Optics Express*, and member of the Editorial Advisory Board of *ACS Photonics*. He is Fellow of OSA The Optical Society, NRF Investigator (class of 2020), and A*STAR Investigator (2010). His accolades include the IPS Nanotechnology Medal and Prize (Institute of Physics Singapore), MIT Technology Review TR35 award, and the Singapore Young Scientist Award.

Junqiao Wu received a B.S. from Fudan University and a M.S. from Peking University, China, both in Physics. He obtained a Ph.D. degree in Applied Physics from the University of California, Berkeley, and did postdoctoral research in chemistry at Harvard University. He began his faculty appointment in the Department of Materials Science and Engineering at UC Berkeley in 2006. His honors include the 29th Ross N. Tucker Memorial Award, the US-NSF Career Award, the US-DOE Early Career Award, the Presidential Early Career Award for Scientists and Engineers (PECASE) from the White House, elected Fellow of the American Physical Society (APS), and the title of Clarivate Highly Cited Researcher. He is currently the Chair of the Applied Science and Technology Graduate Group at UC Berkeley (the largest interdisciplinary Ph.D.-level research program on campus) and also holds a joint appointment at the Lawrence Berkeley National Laboratory. The Wu group explores physics and applications of electronic materials. Prof. Wu has published over 200 widely cited papers in these fields.

Cheng-Wei Qiu received the B.Eng. degree from the University of Science and Technology of China, Hefei, China, in 2003 and the Ph.D. degree from the National University of Singapore (NUS), Singapore, in 2007. He was a Postdoctoral Fellow with the Physics Department, Massachusetts Institute of Technology (MIT), Cambridge, MA, USA, until 2009. In 2009, he joined the NUS as an Assistant Professor and was promoted to Associate Professor with tenure in 2017. Prof. Qiu currently holds Dean's Chair Professor in National University of Singapore. He has received many awards like MIT TR35@Singapore Award, Young Scientist Award by Singapore National Academy of Science, Faculty Young Research Award in NUS, SPIE Rising Researcher Award, Young Engineering Research Award, Engineering Researcher Award in NUS, World Scientific Medal by Institute of Physics, Singapore, etc. He is known for metasurfaces and optical manipulation. He has published over 380 peer-reviewed journal papers. He was a Highly Cited Researcher in 2019, 2020, and 2021 by Web of Science, and a Fellow of The Electromagnetics Academy, US. He has been serving in Associate Editor for various journals such as *JOSA B*, *Photonix*, *Photonics Research*, and Editor-in-Chief for *eLight*. He is in Editorial Advisory Board for *Laser and Photonics Review*, *Advanced Optical Materials*, and *ACS Photonics*.

ACKNOWLEDGMENTS

C.W.Q. acknowledges the support by Ministry of Education, Singapore, via the grant A-8000107-01-00 and the partial support by the grant A-0005947-02-00 from Advanced Research and Technology Innovation Centre (ARTIC) in National University of Singapore. K.T. acknowledges the support from National Key R&D Program of China (2019YFB2205401), NSFC (61834001 and 61927901), and 111 Project (B18001). J.W. acknowledges support from the U.S. NSF grant no. ECCS-1953803. J.H.T. acknowledges the support from A*STAR under grants H19H6a0025, A20E5c0084, and A2083c0058. J.K.W.Y. acknowledges support from A*STAR AME IRG

(A20E5C0093) and NRF CRP (CRP20-2017-0004). R.E.S. is thankful for funding from A-STAR (A18A7b0058), the ONRG (N62909-19-1-2005), and Intel corporation. G.H. acknowledges the support from A*STAR under its AME Young Individual Research Grants (YIRG, no. A2084c0172). This research / project is also supported by the National Research Foundation, Singapore (NRF) under NRF's Medium Sized Centre: Singapore Hybrid-Integrated Next-Generation μ -Electronics (SHINE) Centre funding programme. The authors thank Dr. Hao Wang (SUTD) and Dr. Hao Luo (Zhejiang University) for helpful discussions.

ABBREVIATIONS

1D	= one-dimensional
2D	= two-dimensional
3D	= three-dimensional
AFM	= atomic force microscope
a-GST	= amorphous GST
AI	= artificial intelligence
ALD	= atomic layer deposition
BEC	= bottom electrode contact
BP	= black phosphorus
CD	= compact disk
C-GST	= carbon-doped GST
c-GST	= crystalline GST
CMOS	= complementary metal-oxide semiconductor
CNT	= carbon nanotube
CVD	= chemical vapor deposition
DC	= direct current
DP	= depression pulse
DVD	= digital video disk
ED	= electric dipole
ELF	= electron localization function
EXAFS	= extended X-ray absorption fine structure
FCC	= face-centered cubic
FEM	= finite element method
FOM	= figure-of-merit
GSST	= $\text{Ge}_2\text{Sb}_2\text{Se}_4\text{Te}_1$
GST	= $\text{Ge}_2\text{Sb}_2\text{Te}_5$
HD DVD	= high-definition digital versatile disk
HEV	= high-energy visible
iPCM	= interfacial phase-change memory
IR	= infrared
ITO	= indium tin oxide
I–V	= current–voltage
LCP	= left-handed circular polarization
LSPR	= localized surface plasmon resonance
LTD	= long-term depression
LTP	= long-term potentiation
LWIR	= long-wave infrared
MBE	= molecular beam epitaxy
MEMS	= microelectromechanical system
Mg-VO ₂	= Mg-doped VO ₂
MIM	= metal–insulator–metal
MIR	= mid-infrared
MIT	= metal-to-insulator transition
MLC	= multiple level cell
MVB	= metavalent bonding
MVM	= matrix-vector multiplication
MWIR	= midwave infrared
NEDT	= noise equivalent differential temperature
N-GST	= N doped GST
NIR	= near-infrared

NVM = nonvolatile memory
 OAM = orbital angular momenta
 ONN = optical neural network
 PCM = phase change material
 PCRAM = phase-change random-access memory
 PF = Poole–Frenkel
 PhP = phonon polariton
 PLD = pulsed laser deposition
 PMMA = poly(methyl methacrylate)
 PMMC = programmable metasurface mode converter
 PP = potentiation pulse
 PRP = presynaptic pulse
 PSOI = photonic spin–orbit interaction
 PSP = postsynaptic potential pulse
 RAM = random access memory
 RCP = right-handed circular polarization
 SEM = scanning electron microscope
 SLL = superlattice-like
 SPhP = surface phonon polariton
 SPP = surface plasmon polariton
 s-SNOM = scattering-type scanning near-field microscopes
 STDP = spike-timing-dependent plasticity
 TARC = temperature-adaptive radiative coating
 TCAM = Ti-centered atomic motif
 TEM = transmission electron microscope
 THG = third-harmonic generation
 TiO₂ = titanium dioxide
 Ti–Sb–Te = titanium doped Sb–Te
 TMDC = transition metal dichalcogenide
 TMO = transition metal oxide
 UV = ultraviolet
 vdW = van der Waal
 VGC = VO₂/graphene/CNT
 Vis-to-NIR = visible-to-near-infrared
 WO₃ = tungsten trioxide
 W-VO₂ = W-doped VO₂

REFERENCES

- (1) Shaltout, A. M.; Shalae, V. M.; Brongersma, M. L. Spatiotemporal Light Control with Active Metasurfaces. *Science* **2019**, *364*, No. eaat3100.
- (2) Hiraya, W.; Mishima, N.; Shima, T.; Tai, S.; Tsuruoka, T.; Valov, I.; Hasegawa, T. Resistivity Control by the Electrochemical Removal of Dopant Atoms from a Nanodot. *Faraday Discuss.* **2019**, *213*, 29–40.
- (3) Sunku, S. S.; Ni, G. X.; Jiang, B. Y.; Yoo, H.; Sternbach, A.; McLeod, A. S.; Stauber, T.; Xiong, L.; Taniguchi, T.; Watanabe, K.; et al. Photonic Crystals for Nano-Light in Moiré Graphene Superlattices. *Science* **2018**, *362*, 1153–1156.
- (4) Kim, J.; Baik, S. S.; Ryu, S. H.; Sohn, Y.; Park, S.; Park, B. G.; Denlinger, J.; Yi, Y.; Choi, H. J.; Kim, K. S. Observation of Tunable Band Gap and Anisotropic Dirac Semimetal State in Black Phosphorus. *Science* **2015**, *349*, 723–726.
- (5) Kang, L.; Cui, Y.; Lan, S.; Rodrigues, S. P.; Brongersma, M. L.; Cai, W. Electrifying Photonic Metamaterials for Tunable Nonlinear Optics. *Nat. Commun.* **2014**, *5*, 4680.
- (6) Rahmani, M.; Xu, L.; Miroshnichenko, A. E.; Komar, A.; Camacho-Morales, R.; Chen, H.; Zárate, Y.; Kruk, S.; Zhang, G.; Neshev, D. N.; Kivshar, Y. S. Reversible Thermal Tuning of All-Dielectric Metasurfaces. *Adv. Funct. Mater.* **2017**, *27*, 1700580.
- (7) Decker, M.; Kremers, C.; Minovich, A.; Staude, I.; Miroshnichenko, A. E.; Chigrin, D.; Neshev, D. N.; Jagdish, C.; Kivshar, Y. S. Electro-Optical Switching by Liquid-Crystal Controlled Metasurfaces. *Opt. Express* **2013**, *21*, 8879–8885.
- (8) Kamali, S. M.; Arbabi, E.; Arbabi, A.; Horie, Y.; Faraon, A. Highly Tunable Elastic Dielectric Metasurface Lenses. *Laser Photonics Rev.* **2016**, *10*, 1002–1008.
- (9) Ee, H.-S.; Agarwal, R. Tunable Metasurface and Flat Optical Zoom Lens on a Stretchable Substrate. *Nano Lett.* **2016**, *16*, 2818–2823.
- (10) She, A.; Zhang, S.; Shian, S.; Clarke, D. R.; Capasso, F. Adaptive Metalenses with Simultaneous Electrical Control of Focal Length, Astigmatism, and Shift. *Sci. Adv.* **2018**, *4*, No. eaap9957.
- (11) Arbabi, E.; Arbabi, A.; Kamali, S. M.; Horie, Y.; Faraji-Dana, M.; Faraon, A. MEMS-Tunable Dielectric Metasurface Lens. *Nat. Commun.* **2018**, *9*, 812.
- (12) Morin, F. J. Oxides Which Show a Metal-to-Insulator Transition at the Neel Temperature. *Phys. Rev. Lett.* **1959**, *3*, 34–36.
- (13) Mohn, P.; Wohlfarth, E. The Curie Temperature of the Ferromagnetic Transition Metals and Their Compounds. *J. Phys. F: Met. Phys.* **1987**, *17*, 2421–2430.
- (14) Chen, M.; Rubin, K. A.; Barton, R. W. Compound Materials for Reversible, Phase-Change Optical Data Storage. *Appl. Phys. Lett.* **1986**, *49*, 502–504.
- (15) Wuttig, M.; Yamada, N. Phase-Change Materials for Rewriteable Data Storage. *Nat. Mater.* **2007**, *6*, 824–832.
- (16) Kato, T.; Hirata, H.; Komaki, T.; Inoue, H.; Shingai, H.; Hayashida, N.; Utsunomiya, H. The Phase Change Optical Disc with the Data Recording Rate of 140 Mbps. *Jpn. J. Appl. Phys.* **2002**, *41*, 1664–1667.
- (17) Iwasaki, H.; Ide, Y.; Harigaya, M.; Kageyama, Y.; Fujimura, I. Completely Erasable Phase Change Optical Disk. *Jpn. J. Appl. Phys.* **1992**, *31*, 461–465.
- (18) Yamada, N.; Ohno, E.; Nishiuchi, K.; Akahira, N.; Takao, M. Rapid-Phase Transitions of GeTe–Sb₂Te₃ Pseudobinary Amorphous Thin Films for an Optical Disk Memory. *J. Appl. Phys.* **1991**, *69*, 2849–2856.
- (19) Ohno, E.; Yamada, N.; Kurumizawa, T.; Kimura, K.; Takao, M. Tegegnau Alloys for Phase Change Type Optical Disk Memories. *Jpn. J. Appl. Phys.* **1989**, *28*, 1235–1240.
- (20) Ma, T.; Yang, H.; Zhang, Y.; Lu, L.; Wang, X. Using Phase Change Materials in Photovoltaic Systems for Thermal Regulation and Electrical Efficiency Improvement: A Review and Outlook. *Renewable Sustainable Energy Rev.* **2015**, *43*, 1273–1284.
- (21) Mofijur, M.; Mahlia, T. M. I.; Silitonga, A. S.; Ong, H. C.; Silakhori, M.; Hasan, M. H.; Putra, N.; Rahman, S. Phase Change Materials (PCM) for Solar Energy Usages and Storage: An Overview. *Energies* **2019**, *12*, 3167.
- (22) Pandey, A.; Hossain, M.; Tyagi, V.; Abd Rahim, N.; Jeyraj, A.; Selvaraj, L.; Sari, A. Novel Approaches and Recent Developments on Potential Applications of Phase Change Materials in Solar Energy. *Renewable Sustainable Energy Rev.* **2018**, *82*, 281–323.
- (23) Pielichowska, K.; Pielichowski, K. Phase Change Materials for Thermal Energy Storage. *Prog. Mater. Sci.* **2014**, *65*, 67–123.
- (24) Fan, L.; Khodadadi, J. M. Thermal Conductivity Enhancement of Phase Change Materials for Thermal Energy Storage: A Review. *Renewable Sustainable Energy Rev.* **2011**, *15*, 24–46.
- (25) Dong, K.; Hong, S.; Deng, Y.; Ma, H.; Li, J.; Wang, X.; Yeo, J.; Wang, L.; Lou, S.; Tom, K. B.; et al. A Lithography-Free and Field-Programmable Photonic Metacanvas. *Adv. Mater.* **2018**, *30*, 1703878.
- (26) Tang, K.; Wang, X.; Dong, K.; Li, Y.; Li, J.; Sun, B.; Zhang, X.; Dames, C.; Qiu, C.; Yao, J.; et al. A Thermal Radiation Modulation Platform by Emissivity Engineering with Graded Metal-Insulator Transition. *Adv. Mater.* **2020**, *32*, 1907071.
- (27) Schrecongost, D.; Xiang, Y.; Chen, J.; Ying, C.; Zhang, H.-T.; Yang, M.; Gajurel, P.; Dai, W.; Engel-Herbert, R.; Cen, C. Rewritable Nanoplasmonics through Room-Temperature Phase Manipulations of Vanadium Dioxide. *Nano Lett.* **2020**, *20*, 7760–7766.
- (28) Abedini Dereshgi, S.; Larciprete, M. C.; Centini, M.; Murthy, A. A.; Tang, K.; Wu, J.; Dravid, V. P.; Aydin, K. Tuning of Optical Phonons in α -MoO₃-VO₂ Multilayers. *ACS Appl. Mater. Interfaces* **2021**, *13*, 48981–48987.

- (29) Tang, K.; Dong, K.; Nicolai, C. J.; Li, Y.; Li, J.; Lou, S.; Qiu, C. W.; Raulet, D. H.; Yao, J.; Wu, J. Millikelvin-Resolved Ambient Thermography. *Sci. Adv.* **2020**, *6*, No. eabd8688.
- (30) Du, Z.; Li, M.; Xu, S.; Li, K.; Zou, F.; Zhang, R.; Li, G. VO₂-Based Intelligent Thermal Control Coating for Spacecraft by Regulating Infrared Emittance. *J. Alloys Compd.* **2022**, *895*, 162679.
- (31) Tang, K.; Dong, K.; Li, J.; Gordon, M. P.; Reichertz, F. G.; Kim, H.; Rho, Y.; Wang, Q.; Lin, C.-Y.; Grigoropoulos, C. P.; et al. Temperature-Adaptive Radiative Coating for All-Season Household Thermal Regulation. *Science* **2021**, *374*, 1504–1509.
- (32) Raoux, S.; Welnic, W.; Ielmini, D. Phase Change Materials and Their Application to Nonvolatile Memories. *Chem. Rev.* **2010**, *110*, 240–267.
- (33) Burr, G. W.; BrightSky, M. J.; Sebastian, A.; Cheng, H.-Y.; Wu, J.-Y.; Kim, S.; Sosa, N. E.; Papandreou, N.; Lung, H.-L.; Pozidis, H.; et al. Recent Progress in Phase-Change Memory Technology. *IEEE J. Emerging Sel. Top. Circuits Syst.* **2016**, *6*, 146–162.
- (34) Cobley, R.; Hayat, H.; Wright, C. A Self-Resetting Spiking Phase-Change Neuron. *Nanotechnology* **2018**, *29*, 195202.
- (35) Tuma, T.; Pantazi, A.; Le Gallo, M.; Sebastian, A.; Eleftheriou, E. Stochastic Phase-Change Neurons. *Nat. Nanotechnol.* **2016**, *11*, 693–699.
- (36) La Barbera, S.; Ly, D. R.; Navarro, G.; Castellani, N.; Cueto, O.; Bourgeois, G.; De Salvo, B.; Nowak, E.; Querlioz, D.; Vianello, E. Narrow Heater Bottom Electrode-Based Phase Change Memory as a Bidirectional Artificial Synapse. *Adv. Electron. Mater.* **2018**, *4*, 1800223.
- (37) Wright, C. D.; Hosseini, P.; Diosdado, J. A. V. Beyond von-Neumann Computing with Nanoscale Phase-Change Memory Devices. *Adv. Funct. Mater.* **2013**, *23*, 2248–2254.
- (38) Li, Y.; Zhong, Y.; Xu, L.; Zhang, J.; Xu, X.; Sun, H.; Miao, X. Ultrafast Synaptic Events in a Chalcogenide Memristor. *Sci. Rep.* **2013**, *3*, 1619.
- (39) Kuzum, D.; Jeyasingh, R. G.; Lee, B.; Wong, H.-S. P. Nanoelectronic Programmable Synapses Based on Phase Change Materials for Brain-Inspired Computing. *Nano Lett.* **2012**, *12*, 2179–2186.
- (40) Yu, N.; Capasso, F. Flat Optics with Designer Metasurfaces. *Nat. Mater.* **2014**, *13*, 139–150.
- (41) Ruiz de Galarreta, C.; Carrillo, S. G. C.; Au, Y. Y.; Gemo, E.; Trimby, L.; Shields, J.; Humpheys, E.; Faneca, J.; Cai, L.; Baldycheva, A.; et al. Tunable Optical Metasurfaces Enabled by Chalcogenide Phase-Change Materials: From the Visible to the THz. *J. Opt.* **2020**, *22*, 114001.
- (42) Chaudhary, K.; Tamagnone, M.; Yin, X.; Spagele, C. M.; Oscurato, S. L.; Li, J.; Persch, C.; Li, R.; Rubin, N. A.; Jauregui, L. A.; et al. Polariton Nanophotonics Using Phase-Change Materials. *Nat. Commun.* **2019**, *10*, 4487.
- (43) Carrillo, S. G. C.; Trimby, L.; Au, Y. Y.; Nagareddy, V. K.; Rodriguez-Hernandez, G.; Hosseini, P.; Rios, C.; Bhaskaran, H.; Wright, C. D. A Nonvolatile Phase-Change Metamaterial Color Display. *Adv. Opt. Mater.* **2019**, *7*, 1801782.
- (44) Folland, T. G.; Fali, A.; White, S. T.; Matson, J. R.; Liu, S.; Aghamiri, N. A.; Edgar, J. H.; Haglund, R. F., Jr.; Abate, Y.; Caldwell, J. D. Reconfigurable Infrared Hyperbolic Metasurfaces Using Phase Change Materials. *Nat. Commun.* **2018**, *9*, 4371.
- (45) de Galarreta, C. R.; Alexeev, A. M.; Au, Y. Y.; Lopez-Garcia, M.; Klemm, M.; Cryan, M.; Bertolotti, J.; Wright, C. D. Nonvolatile Reconfigurable Phase-Change Metadevices for Beam Steering in the Near Infrared. *Adv. Funct. Mater.* **2018**, *28*, 1704993.
- (46) Tian, J.; Luo, H.; Yang, Y.; Ding, F.; Qu, Y.; Zhao, D.; Qiu, M.; Bozhevolnyi, S. I. Active Control of Anapole States by Structuring the Phase-Change Alloy Ge₂Sb₂Te₅. *Nat. Commun.* **2019**, *10*, 396.
- (47) Qu, Y.; Li, Q.; Cai, L.; Pan, M.; Ghosh, P.; Du, K.; Qiu, M. Thermal Camouflage Based on the Phase-Changing Material GST. *Light Sci. Appl.* **2018**, *7*, 26.
- (48) Du, K.; Cai, L.; Luo, H.; Lu, Y.; Tian, J.; Qu, Y.; Ghosh, P.; Lyu, Y.; Cheng, Z.; Qiu, M.; et al. Wavelength-Tunable Mid-Infrared Thermal Emitters with a Non-Volatile Phase Changing Material. *Nanoscale* **2018**, *10*, 4415–4420.
- (49) Qu, Y.; Li, Q.; Du, K.; Cai, L.; Lu, J.; Qiu, M. Dynamic Thermal Emission Control Based on Ultrathin Plasmonic Metamaterials Including Phase-Changing Material GST. *Laser Photonics Rev.* **2017**, *11*, 1700091.
- (50) Du, K. K.; Li, Q.; Lyu, Y. B.; Ding, J. C.; Lu, Y.; Cheng, Z. Y.; Qiu, M. Control over Emissivity of Zero-Static-Power Thermal Emitters Based on Phase-Changing Material GST. *Light Sci. Appl.* **2017**, *6*, No. e16194.
- (51) Wuttig, M.; Bhaskaran, H.; Taubner, T. Phase-Change Materials for Non-Volatile Photonic Applications. *Nat. Photonics* **2017**, *11*, 465–476.
- (52) Simpson, R. E.; Cao, T. Phase Change Material Photonics. *arXiv* **2020**, arXiv:2006.14441.
- (53) Meng, Y.; Cao, T.; Long, Y. Progress in Metasurfaces Based on Ge-Sb-Te Phase-Change Materials. *J. Appl. Phys.* **2020**, *128*, 140904.
- (54) Raeis-Hosseini, N.; Rho, J. Metasurfaces Based on Phase-Change Material as a Reconfigurable Platform for Multifunctional Devices. *Materials* **2017**, *10*, 1046.
- (55) Yang, W.; Hur, N.; Lim, D.-H.; Jeong, H.; Suh, J. Heterogeneously Structured Phase-Change Materials and Memory. *J. Appl. Phys.* **2021**, *129*, 050903.
- (56) Fantini, P. Phase Change Memory Applications: The History, the Present and the Future. *J. Phys. D: Appl. Phys.* **2020**, *53*, 283002.
- (57) Lotnyk, A.; Behrens, M.; Rauschenbach, B. Phase Change Thin Films for Non-Volatile Memory Applications. *Nanoscale Adv.* **2019**, *1*, 3836–3857.
- (58) Xu, M.; Mai, X.; Lin, J.; Zhang, W.; Li, Y.; He, Y.; Tong, H.; Hou, X.; Zhou, P.; Miao, X. Recent Advances on Neuromorphic Devices Based on Chalcogenide Phase-Change Materials. *Adv. Funct. Mater.* **2020**, *30*, 2003419.
- (59) Zhang, W.; Mazzarello, R.; Wuttig, M.; Ma, E. Designing Crystallization in Phase-Change Materials for Universal Memory and Neuro-Inspired Computing. *Nat. Rev. Mater.* **2019**, *4*, 150–168.
- (60) Kim, C.; Kim, Y.; Lee, M. Laser-Induced Tuning and Spatial Control of the Emissivity of Phase-Changing Ge₂Sb₂Te₅ Emitter for Thermal Camouflage. *Adv. Mater. Technol.* **2022**, 2101349.
- (61) Sámson, Z. L.; MacDonald, K. F.; De Angelis, F.; Gholipour, B.; Knight, K.; Huang, C. C.; Di Fabrizio, E.; Hewak, D. W.; Zheludev, N. I. Metamaterial Electro-Optic Switch of Nanoscale Thickness. *Appl. Phys. Lett.* **2010**, *96*, 143105.
- (62) Cao, T.; Wei, C. W.; Simpson, R. E.; Zhang, L.; Cryan, M. J. Rapid Phase Transition of a Phase-Change Metamaterial Perfect Absorber. *Opt. Mater. Express* **2013**, *3*, 1101–1110.
- (63) Cao, T.; Zhang, L.; Simpson, R. E.; Cryan, M. J. Mid-Infrared Tunable Polarization-Independent Perfect Absorber Using a Phase-Change Metamaterial. *J. Opt. Soc. Am. B: Opt. Phys.* **2013**, *30*, 1580–1585.
- (64) Rudé, M.; Pello, J.; Simpson, R. E.; Osmond, J.; Roelkens, G.; van der Tol, J. J. G. M.; Pruneri, V. Optical Switching at 1.55 μm in Silicon Racetrack Resonators Using Phase Change Materials. *Appl. Phys. Lett.* **2013**, *103*, 141119.
- (65) Rios, C.; Hosseini, P.; Wright, C. D.; Bhaskaran, H.; Pernice, W. H. On-Chip Photonic Memory Elements Employing Phase-Change Materials. *Adv. Mater.* **2014**, *26*, 1372–1377.
- (66) Wu, S. H.; Chen, M. K.; Barako, M. T.; Jankovic, V.; Hon, P. W. C.; Sweatlock, L. A.; Povinelli, M. L. Thermal Homeostasis Using Microstructured Phase-Change Materials. *Optica* **2017**, *4*, 1390–1396.
- (67) Hosseini, P.; Wright, C. D.; Bhaskaran, H. An Optoelectronic Framework Enabled by Low-Dimensional Phase-Change Films. *Nature* **2014**, *511*, 206–211.
- (68) Wright, C. D.; Liu, Y.; Kohary, K. I.; Aziz, M. M.; Hicken, R. J. Arithmetic and Biologically-Inspired Computing Using Phase-Change Materials. *Adv. Mater.* **2011**, *23*, 3408–3413.
- (69) Rudé, M.; Simpson, R. E.; Quidant, R.; Pruneri, V.; Renger, J. Active Control of Surface Plasmon Waveguides with a Phase Change Material. *ACS Photonics* **2015**, *2*, 669–674.
- (70) Champlain, J. G.; Ruppalt, L. B.; Guyette, A. C.; El-Hinnawy, N.; Borodulin, P.; Jones, E.; Young, R. M.; Nichols, D. Examination of the

Temperature Dependent Electronic Behavior of GeTe for Switching Applications. *J. Appl. Phys.* **2016**, *119*, 244501.

(71) Ríos, C.; Stegmaier, M.; Hosseini, P.; Wang, D.; Scherer, T.; Wright, C. D.; Bhaskaran, H.; Pernice, W. H. Integrated All-Photonic Non-Volatile Multi-Level Memory. *Nat. Photonics* **2015**, *9*, 725–732.

(72) Soma, R.; Nakayama, B.; Kuwahara, M.; Yamamoto, E.; Saiki, T. Phase-Change Janus Particles with Switchable Dual Properties. *Appl. Phys. Lett.* **2020**, *117*, 221601.

(73) Hummel, G.; Hui, Y.; Rinaldi, M. Phase Change Material Programmable Vias for Switching and Reconfiguration of Aluminum Nitride Piezoelectric MEMS Resonators. *2014 IEEE International Frequency Control Symposium (FCS)* **2014**, 549–551.

(74) Simpson, R. E.; Yang, J. K. W.; Hu, J. Are Phase Change Materials Ideal for Programmable Photonics?: Opinion. *Opt. Mater. Express* **2022**, *12*, 2368–2373.

(75) Heckingbottom, R.; Linnett, J. Structure of Vanadium Dioxide. *Nature* **1962**, *194*, 678.

(76) Qazilbash, M. M.; Brehm, M.; Chae, B.-G.; Ho, P.-C.; Andreev, G. O.; Kim, B.-J.; Yun, S. J.; Balatsky, A.; Maple, M.; Keilmann, F.; et al. Mott Transition in VO₂ Revealed by Infrared Spectroscopy and Nano-Imaging. *Science* **2007**, *318*, 1750–1753.

(77) Jeong, J.; Aetukuri, N.; Graf, T.; Schladt, T. D.; Samant, M. G.; Parkin, S. S. Suppression of Metal-Insulator Transition in VO₂ by Electric Field-Induced Oxygen Vacancy Formation. *Science* **2013**, *339*, 1402–1405.

(78) Rao, M.; Ravindranadh, K.; Kasturi, A.; Shekhawat, M. Structural Stoichiometry and Phase Transitions of MoO₃ Thin Films for Solid State Microbatteries. *Res. J. Recent Sci.* **2013**, *2*, 67–73.

(79) Chudnovskii, F.; Odynets, L.; Pergament, A.; Stefanovich, G. Electroforming and Switching in Oxides of Transition Metals: The Role of Metal-Insulator Transition in the Switching Mechanism. *J. Solid State Chem.* **1996**, *122*, 95–99.

(80) Whittaker, L.; Patridge, C. J.; Banerjee, S. Microscopic and Nanoscale Perspective of the Metal-Insulator Phase Transitions of VO₂: Some New Twists to an Old Tale. *J. Phys. Chem. Lett.* **2011**, *2*, 745–758.

(81) Goodenough, J. B. The Two Components of the Crystallographic Transition in VO₂. *J. Solid State Chem.* **1971**, *3*, 490–500.

(82) Mott, N. F. Metal-Insulator Transition. *Rev. Mod. Phys.* **1968**, *40*, 677–683.

(83) Zylbersztein, A.; Mott, N. F. Metal-Insulator Transition in Vanadium Dioxide. *Phys. Rev. B* **1975**, *11*, 4383–4395.

(84) Ke, Y.; Wang, S.; Liu, G.; Li, M.; White, T. J.; Long, Y. Vanadium Dioxide: The Multistimuli Responsive Material and Its Applications. *Small* **2018**, *14*, 1802025.

(85) Cui, Y.; Ke, Y.; Liu, C.; Chen, Z.; Wang, N.; Zhang, L.; Zhou, Y.; Wang, S.; Gao, Y.; Long, Y. Thermochromic VO₂ for Energy-Efficient Smart Windows. *Joule* **2018**, *2*, 1707–1746.

(86) Liu, K.; Lee, S.; Yang, S.; Delaire, O.; Wu, J. Recent Progresses on Physics and Applications of Vanadium Dioxide. *Mater. Today* **2018**, *21*, 875–896.

(87) Wei, J.; Wang, Z.; Chen, W.; Cobden, D. H. New Aspects of the Metal-Insulator Transition in Single-Domain Vanadium Dioxide Nanobeams. *Nat. Nanotechnol.* **2009**, *4*, 420–424.

(88) Ke, Y. J.; Chen, J. W.; Lin, C. J.; Wang, S. C.; Zhou, Y.; Yin, J.; Lee, P. S.; Long, Y. Smart Windows: Electro-, Thermo-, Mechano-, Photochromics, and Beyond. *Adv. Energy Mater.* **2019**, *9*, 1902066.

(89) Ke, Y.; Zhou, C.; Zhou, Y.; Wang, S.; Chan, S. H.; Long, Y. Emerging Thermal-Responsive Materials and Integrated Techniques Targeting the Energy-Efficient Smart Window Application. *Adv. Funct. Mater.* **2018**, *28*, 1800113.

(90) Cao, X.; Chang, T.; Shao, Z.; Xu, F.; Luo, H.; Jin, P. Challenges and Opportunities toward Real Application of VO₂-Based Smart Glazing. *Matter* **2020**, *2*, 862–881.

(91) Ke, Y.; Balin, I.; Wang, N.; Lu, Q.; Tok, A. I. Y.; White, T. J.; Magdassi, S.; Abdulhalim, I.; Long, Y. Two-Dimensional SiO₂/VO₂ Photonic Crystals with Statically Visible and Dynamically Infrared Modulated for Smart Window Deployment. *ACS Appl. Mater. Interfaces* **2016**, *8*, 33112–33120.

(92) Ke, Y.; Wen, X.; Zhao, D.; Che, R.; Xiong, Q.; Long, Y. Controllable Fabrication of Two-Dimensional Patterned VO₂ Nanoparticle, Nanodome, and Nanonet Arrays with Tunable Temperature-Dependent Localized Surface Plasmon Resonance. *ACS Nano* **2017**, *11*, 7542–7551.

(93) Ke, Y.; Yin, Y.; Zhang, Q.; Tan, Y.; Hu, P.; Wang, S.; Tang, Y.; Zhou, Y.; Wen, X.; Wu, S.; et al. Adaptive Thermochromic Windows from Active Plasmonic Elastomers. *Joule* **2019**, *3*, 858–871.

(94) Xu, Q.; Ke, Y.; Feng, C.; Chen, C.; Wen, Z.; Wang, H.; Sun, M.; Liu, X.; Liu, H.; Magdassi, S.; et al. Anisotropic Localized Surface Plasmon Resonance of Vanadium Dioxide Rods in Flexible Thermochromic Film Towards Multifunctionality. *Sol. Energy Mater. Sol. Cells* **2021**, *230*, 111163.

(95) Wang, S.; Liu, G.; Hu, P.; Zhou, Y.; Ke, Y.; Li, C.; Chen, J.; Cao, T.; Long, Y. Largely Lowered Transition Temperature of a VO₂/Carbon Hybrid Phase Change Material with High Thermal Emissivity Switching Ability and near Infrared Regulations. *Adv. Mater. Interfaces* **2018**, *5*, 1801063.

(96) Xiao, L.; Ma, H.; Liu, J.; Zhao, W.; Jia, Y.; Zhao, Q.; Liu, K.; Wu, Y.; Wei, Y.; Fan, S.; et al. Fast Adaptive Thermal Camouflage Based on Flexible VO₂/Graphene/CNT Thin Films. *Nano Lett.* **2015**, *15*, 8365–8370.

(97) Wang, S.; Jiang, T.; Meng, Y.; Yang, R.; Tan, G.; Long, Y. Scalable Thermochromic Smart Windows with Passive Radiative Cooling Regulation. *Science* **2021**, *374*, 1501–1504.

(98) Ke, Y.; Zhang, B.; Wang, T.; Zhong, Y.; Vu, T. D.; Wang, S.; Liu, Y.; Magdassi, S.; Ye, X.; Zhao, D.; et al. Manipulating Atomic Defects in Plasmonic Vanadium Dioxide for Superior Solar and Thermal Management. *Mater. Horiz.* **2021**, *8*, 1700–1710.

(99) Asayesh-Ardakani, H.; Nie, A.; Marley, P. M.; Zhu, Y.; Phillips, P. J.; Singh, S.; Mashayek, F.; Sambandamurthy, G.; Low, K.-b.; Klie, R. F.; et al. Atomic Origins of Monoclinic-Tetragonal (Rutile) Phase Transition in Doped VO₂ Nanowires. *Nano Lett.* **2015**, *15*, 7179–7188.

(100) Hong, W.-K.; Park, J. B.; Yoon, J.; Kim, B.-J.; Sohn, J. I.; Lee, Y. B.; Bae, T.-S.; Chang, S.-J.; Huh, Y. S.; Son, B.; et al. Hydrogen-Induced Morphotropic Phase Transformation of Single-Crystalline Vanadium Dioxide Nanobeams. *Nano Lett.* **2013**, *13*, 1822–1828.

(101) Yoon, H.; Choi, M.; Lim, T.-W.; Kwon, H.; Ihm, K.; Kim, J. K.; Choi, S.-Y.; Son, J. Reversible Phase Modulation and Hydrogen Storage in Multivalent VO₂ Epitaxial Thin Films. *Nat. Mater.* **2016**, *15*, 1113–1119.

(102) Muraoka, Y.; Hiroi, Z. Metal-Insulator Transition of VO₂ Thin Films Grown on TiO₂ (001) and (110) Substrates. *Appl. Phys. Lett.* **2002**, *80*, 583–585.

(103) Nagashima, K.; Yanagida, T.; Tanaka, H.; Kawai, T. Stress Relaxation Effect on Transport Properties of Strained Vanadium Dioxide Epitaxial Thin Films. *Phys. Rev. B* **2006**, *74*, 172106.

(104) Lee, D.; Lee, J.; Song, K.; Xue, F.; Choi, S.-Y.; Ma, Y.; Podkaminer, J.; Liu, D.; Liu, S.-C.; Chung, B.; et al. Sharp VO₂ Phase Transition via Controlled Release of Epitaxial Strain. *Nano Lett.* **2017**, *17*, 5614–5619.

(105) Cao, J.; Gu, Y.; Fan, W.; Chen, L. Q.; Ogletree, D. F.; Chen, K.; Tamura, N.; Kunz, M.; Barrett, C.; Seidel, J.; et al. Extended Mapping and Exploration of the Vanadium Dioxide Stress-Temperature Phase Diagram. *Nano Lett.* **2010**, *10*, 2667–2673.

(106) Li, M.; Magdassi, S.; Gao, Y.; Long, Y. Hydrothermal Synthesis of VO₂ Polymorphs: Advantages, Challenges and Prospects for the Application of Energy Efficient Smart Windows. *Small* **2017**, *13*, 1701147.

(107) Li, Y.; Ji, S.; Gao, Y.; Luo, H.; Kanehira, M. Core-Shell VO₂@TiO₂ Nanorods That Combine Thermochromic and Photocatalytic Properties for Application as Energy-Saving Smart Coatings. *Sci. Rep.* **2013**, *3*, 1370.

(108) Cao, J.; Ertekin, E.; Srinivasan, V.; Fan, W.; Huang, S.; Zheng, H.; Yim, J.; Khanal, D.; Ogletree, D.; Grossman, J.; et al. Strain Engineering and One-Dimensional Organization of Metal-Insulator Domains in Single-Crystal Vanadium Dioxide Beams. *Nat. Nanotechnol.* **2009**, *4*, 732–737.

- (109) Wei, J.; Ji, H.; Guo, W.; Nevidomskyy, A. H.; Natelson, D. Hydrogen Stabilization of Metallic Vanadium Dioxide in Single-Crystal Nanobeams. *Nat. Nanotechnol.* **2012**, *7*, 357–362.
- (110) Shi, R.; Cai, X.; Wang, W.; Wang, J.; Kong, D.; Cai, N.; Chen, P.; He, P.; Wu, Z.; Amini, A.; et al. Single-Crystalline Vanadium Dioxide Actuators. *Adv. Funct. Mater.* **2019**, *29*, 1900527.
- (111) Fu, D.; Liu, K.; Tao, T.; Lo, K.; Cheng, C.; Liu, B.; Zhang, R.; Bechtel, H. A.; Wu, J. Comprehensive Study of the Metal-Insulator Transition in Pulsed Laser Deposited Epitaxial VO₂ Thin Films. *J. Appl. Phys.* **2013**, *113*, 043707.
- (112) Quackenbush, N. F.; Tashman, J. W.; Mundy, J. A.; Sallis, S.; Paik, H.; Misra, R.; Moyer, J. A.; Guo, J. H.; Fischer, D. A.; Woicik, J. C.; et al. Nature of the Metal Insulator Transition in Ultrathin Epitaxial Vanadium Dioxide. *Nano Lett.* **2013**, *13*, 4857–4861.
- (113) Xu, Z.; Li, Q.; Du, K.; Long, S.; Yang, Y.; Cao, X.; Luo, H.; Zhu, H.; Ghosh, P.; Shen, W.; et al. Spatially Resolved Dynamically Reconfigurable Multilevel Control of Thermal Emission. *Laser Photonics Rev.* **2020**, *14*, 1900162.
- (114) Jensen, W. B. A Note on the Term "Chalcogen". *J. Chem. Educ.* **1997**, *74*, 1063–1064.
- (115) Fischer, W. A Second Note on the Term "Chalcogen". *J. Chem. Educ.* **2001**, *78*, 1333.
- (116) Elliott, S. R. Chalcogenide Glasses. *Mater. Sci. Technol.*; Wiley-VCH, 2006.
- (117) Kolobov, A. V.; Tominaga, J. *Chalcogenides: Metastability and Phase Change Phenomena*; Springer, 2012; pp 65–145.
- (118) Ovshinsky, S. R. Reversible Electrical Switching Phenomena in Disordered Structures. *Phys. Rev. Lett.* **1968**, *21*, 1450–1453.
- (119) Hoddeson, L.; Garrett, P. The Discovery of Ovshinsky Switching and Phase-Change Memory. *Phys. Today* **2018**, *71*, 44–51.
- (120) Shastri, B. J.; Tait, A. N.; Ferreira de Lima, T.; Pernice, W. H.; Bhaskaran, H.; Wright, C. D.; Prucnal, P. R. Photonics for Artificial Intelligence and Neuromorphic Computing. *Nat. Photonics* **2021**, *15*, 102–114.
- (121) Cao, T.; Wang, R. Z.; Simpson, R. E.; Li, G. X. Photonic Ge-Sb-Te Phase Change Metamaterials and Their Applications. *Prog. Quantum Electron.* **2020**, *74*, 100299.
- (122) Simpson, R. E.; Fons, P.; Kolobov, A. V.; Fukaya, T.; Krbal, M.; Yagi, T.; Tominaga, J. Interfacial Phase-Change Memory. *Nat. Nanotechnol.* **2011**, *6*, 501–505.
- (123) Chong, T. C.; Shi, L. P.; Qiang, W.; Tan, P. K.; Miao, X. S.; Hu, X. Superlattice-Like Structure for Phase Change Optical Recording. *J. Appl. Phys.* **2002**, *91*, 3981–3987.
- (124) Yamada, N. Origin, Secret, and Application of the Ideal Phase-Change Material GeSbTe. *Phys. Status Solidi B* **2012**, *249*, 1837–1842.
- (125) Bruns, G.; Merkelbach, P.; Schlockermann, C.; Salinga, M.; Wuttig, M.; Happ, T.; Philipp, J.; Kund, M. Nanosecond Switching in GeTe Phase Change Memory Cells. *Appl. Phys. Lett.* **2009**, *95*, 043108.
- (126) Robertson, J.; Xiong, K.; Peacock, P. W. Electronic and Atomic Structure of Ge₂Sb₂Te₅ Phase Change Memory Material. *Thin Solid Films* **2007**, *515*, 7538–7541.
- (127) Shportko, K.; Kremers, S.; Woda, M.; Lencer, D.; Robertson, J.; Wuttig, M. Resonant Bonding in Crystalline Phase-Change Materials. *Nat. Mater.* **2008**, *7*, 653–658.
- (128) Krbal, M.; Kolobov, A. V.; Fons, P.; Tominaga, J.; Elliott, S. R.; Hegedus, J.; Uruga, T. Intrinsic Complexity of the Melt-Quenched Amorphous Ge₂Sb₂Te₅ Memory Alloy. *Phys. Rev. B* **2011**, *83*, 054203.
- (129) Waldecker, L.; Miller, T. A.; Rude, M.; Bertoni, R.; Osmond, J.; Pruneri, V.; Simpson, R. E.; Ernstorfer, R.; Wall, S. Time-Domain Separation of Optical Properties from Structural Transitions in Resonantly Bonded Materials. *Nat. Mater.* **2015**, *14*, 991–995.
- (130) Kolobov, A. V.; Krbal, M.; Fons, P.; Tominaga, J.; Uruga, T. Distortion-Triggered Loss of Long-Range Order in Solids with Bonding Energy Hierarchy. *Nat. Chem.* **2011**, *3*, 311–316.
- (131) Wuttig, M.; Deringer, V. L.; Gonze, X.; Bichara, C.; Raty, J. Y. Incipient Metals: Functional Materials with a Unique Bonding Mechanism. *Adv. Mater.* **2018**, *30*, 1803777.
- (132) Lee, T. H.; Elliott, S. R. Chemical Bonding in Chalcogenides: The Concept of Multicenter Hyperbonding. *Adv. Mater.* **2020**, *32*, 2000340.
- (133) Martinez, J. C.; Lu, L.; Ning, J.; Dong, W.; Cao, T.; Simpson, R. E. The Origin of Optical Contrast in Sb₂Te₃-Based Phase-Change Materials. *Phys. Status Solidi B* **2020**, *257*, 1900289.
- (134) Michel, A. K. U.; Wuttig, M.; Taubner, T. Design Parameters for Phase-Change Materials for Nanostructure Resonance Tuning. *Adv. Opt. Mater.* **2017**, *5*, 1700261.
- (135) Dong, W.; Liu, H.; Behera, J. K.; Lu, L.; Ng, R. J.; Sreekanth, K. V.; Zhou, X.; Yang, J. K.; Simpson, R. E. Wide Bandgap Phase Change Material Tuned Visible Photonics. *Adv. Funct. Mater.* **2019**, *29*, 1806181.
- (136) Delaney, M.; Zeimpekis, I.; Lawson, D.; Hewak, D. W.; Muskens, O. L. A New Family of Ultralow Loss Reversible Phase-Change Materials for Photonic Integrated Circuits: Sb₂S₃ and Sb₂Se₃. *Adv. Funct. Mater.* **2020**, *30*, 2002447.
- (137) Zhang, Q.; Zhang, Y.; Li, J.; Soref, R.; Gu, T.; Hu, J. Broadband Nonvolatile Photonic Switching Based on Optical Phase Change Materials: Beyond the Classical Figure-of-Merit. *Opt. Lett.* **2018**, *43*, 94–97.
- (138) Gao, K.; Du, K.; Tian, S.; Wang, H.; Zhang, L.; Guo, Y.; Luo, B.; Zhang, W.; Mei, T. Intermediate Phase-Change States with Improved Cycling Durability of Sb₂S₃ by Femtosecond Multi-Pulse Laser Irradiation. *Adv. Funct. Mater.* **2021**, *31*, 2103327.
- (139) Ding, K.; Wang, J.; Zhou, Y.; Tian, H.; Lu, L.; Mazzarello, R.; Jia, C.; Zhang, W.; Rao, F.; Ma, E. Phase-Change Heterostructure Enables Ultralow Noise and Drift for Memory Operation. *Science* **2019**, *366*, 210–215.
- (140) Rao, F.; Ding, K.; Zhou, Y.; Zheng, Y.; Xia, M.; Lv, S.; Song, Z.; Feng, S.; Ronneberger, L.; Mazzarello, R. Reducing the Stochasticity of Crystal Nucleation to Enable Subnanosecond Memory Writing. *Science* **2017**, *358*, 1423–1427.
- (141) Orava, J.; Greer, A. L.; Gholipour, B.; Hewak, D. W.; Smith, C. E. Characterization of Supercooled Liquid Ge₂Sb₂Te₅ and Its Crystallization by Ultrafast-Heating Calorimetry. *Nat. Mater.* **2012**, *11*, 279–283.
- (142) Kolobov, A. V.; Fons, P.; Krbal, M.; Simpson, R. E.; Hosokawa, S.; Uruga, T.; Tanida, H.; Tominaga, J. Liquid Ge₂Sb₂Te₅ Studied by Extended X-Ray Absorption. *Appl. Phys. Lett.* **2009**, *95*, 241902.
- (143) Akola, J.; Jones, R. O. Density Functional Study of Amorphous, Liquid and Crystalline Ge₂Sb₂Te₅: Homopolar Bonds and/or Ab Alternation? *J. Phys.: Condens. Matter* **2008**, *20*, No. 465103.
- (144) Roscioni, O. M.; Branicio, P. S.; Kalikka, J.; Zhou, X.; Simpson, R. E. Local Structure of Ge₂Sb₂Te₅ During Crystallization under Pressure. *Appl. Phys. Lett.* **2018**, *112*, 151901.
- (145) Zhou, X.; Du, Y.; Behera, J. K.; Wu, L.; Song, Z.; Simpson, R. E. Oxygen Tuned Local Structure and Phase-Change Performance of Germanium Telluride. *ACS Appl. Mater. Interfaces* **2016**, *8*, 20185–20191.
- (146) Tominaga, J.; Shima, T.; Fons, P.; Simpson, R.; Kuwahara, M.; Kolobov, A. What Is the Origin of Activation Energy in Phase-Change Films? *Jpn. J. Appl. Phys.* **2009**, *48*, 03A053.
- (147) Lankhorst, M. H. R.; Ketelaars, B. W.; Wolters, R. Low-Cost and Nanoscale Non-Volatile Memory Concept for Future Silicon Chips. *Nat. Mater.* **2005**, *4*, 347–352.
- (148) Ahn, C.; Fong, S. W.; Kim, Y.; Lee, S.; Sood, A.; Neumann, C. M.; Asheghi, M.; Goodson, K. E.; Pop, E.; Wong, H.-S. P. Energy-Efficient Phase-Change Memory with Graphene as a Thermal Barrier. *Nano Lett.* **2015**, *15*, 6809–6814.
- (149) Xiong, F.; Liao, A. D.; Estrada, D.; Pop, E. Low-Power Switching of Phase-Change Materials with Carbon Nanotube Electrodes. *Science* **2011**, *332*, 568–570.
- (150) Neumann, C. M.; Okabe, K. L.; Yalon, E.; Grady, R. W.; Wong, H.-S. P.; Pop, E. Engineering Thermal and Electrical Interface Properties of Phase Change Memory with Monolayer MoS₂. *Appl. Phys. Lett.* **2019**, *114*, 082103.

- (151) Meyer, S.; Tan, Z. Y.; Chigrin, D. N. Multiphysics Simulations of Adaptive Metasurfaces at the Meta-Atom Length Scale. *Nanophotonics* **2020**, *9*, 675–681.
- (152) Wang, Y.; Ning, J.; Bosman, M.; Simpson, R. A Multi-Physics Cellular Automata Model for Simulating Phase Change Photonics Devices. *Active Photonic Platforms XIII* **2021**, 11796, 1179625.
- (153) Ritala, M.; Pore, V.; Hatanpaa, T.; Heikkila, M.; Leskela, M.; Mizohata, K.; Schrott, A.; Raoux, S.; Rossnagel, S. M. Atomic Layer Deposition of Ge₂Sb₂Te₅ Thin Films. *Microelectron. Eng.* **2009**, *86*, 1946–1949.
- (154) Choi, B. J.; Choi, S.; Shin, Y. C.; Hwang, C. S.; Lee, J. W.; Jeong, J.; Kim, Y. J.; Hwang, S. Y.; Hong, S. K. Cyclic PECVD of Ge₂Sb₂Te₅ Films Using Metallorganic Sources. *J. Electrochem. Soc.* **2007**, *154*, H318–H324.
- (155) Bartlett, P. N.; Benjamin, S. L.; Kees de Groot, C. H.; Hector, A. L.; Huang, R. M.; Jolleys, A.; Kissling, G. P.; Levason, W.; Pearce, S. J.; Reid, G.; Wang, Y. Non-Aqueous Electrodeposition of Functional Semiconducting Metal Chalcogenides: Ge₂Sb₂Te₅ Phase Change Memory. *Mater. Horiz.* **2015**, *2*, 420–426.
- (156) Zhou, X. L.; Dong, W. L.; Zhang, H.; Simpson, R. E. A Zero Density Change Phase Change Memory Material: GeTe-O Structural Characteristics Upon Crystallisation. *Sci. Rep.* **2015**, *5*, 11150.
- (157) Saito, Y.; Morota, M.; Makino, K.; Tominaga, J.; Kolobov, A. V.; Fons, P. Recent Developments Concerning the Sputter Growth of Chalcogenide-Based Layered Phase-Change Materials. *Mater. Sci. Semicond. Process.* **2021**, *135*, 106079.
- (158) Koma, A. Van der Waals Epitaxy—a New Epitaxial Growth Method for a Highly Lattice-Mismatched System. *Thin Solid Films* **1992**, *216*, 72–76.
- (159) Vasudevan, R.; Takeuchi, I.; Fessler, J. *21st Century Tools for Accelerating Scientific Research—from Combinatorial Synthesis to Text Mining to Artificial Intelligence*. Materials Research Society, 2017.
- (160) Boschker, J. E.; Tisbi, E.; Placidi, E.; Momand, J.; Redaelli, A.; Kooi, B. J.; Arciprete, F.; Calarco, R. Textured Sb₂Te₃ Films and GeTe/Sb₂Te₃ Superlattices Grown on Amorphous Substrates by Molecular Beam Epitaxy. *AIP Adv.* **2017**, *7*, 015106.
- (161) Hilmi, I.; Lotnyk, A.; Gerlach, J. W.; Schumacher, P.; Rauschenbach, B. Research Update: Van-Der-Waals Epitaxy of Layered Chalcogenide Sb₂Te₃ Thin Films Grown by Pulsed Laser Deposition. *APL Mater.* **2017**, *5*, 050701.
- (162) Ning, J.; Martinez, J. C.; Momand, J.; Zhang, H.; Tiwari, S. C.; Shimojo, F.; Nakano, A.; Kalia, R. K.; Vashishta, P.; Brancio, P. S.; et al. Differences in Sb₂Te₃ Growth by Pulsed Laser and Sputter Deposition. *Acta Mater.* **2020**, *200*, 811–820.
- (163) Lotnyk, A.; Ross, U.; Dankwort, T.; Hilmi, I.; Kienle, L.; Rauschenbach, B. Atomic Structure and Dynamic Reconfiguration of Layered Defects in Van Der Waals Layered Ge-Sb-Te Based Materials. *Acta Mater.* **2017**, *141*, 92–96.
- (164) Saito, Y.; Fons, P.; Bolotov, L.; Miyata, N.; Kolobov, A. V.; Tominaga, J. A Two-Step Process for Growth of Highly Oriented Sb₂Te₃ Using Sputtering. *AIP Adv.* **2016**, *6*, 045220.
- (165) Lee, S. H.; Jung, Y.; Agarwal, R. Highly Scalable Non-Volatile and Ultra-Low-Power Phase-Change Nanowire Memory. *Nat. Nanotechnol.* **2007**, *2*, 626–630.
- (166) Kato, T.; Tanaka, K. Electronic Properties of Amorphous and Crystalline Ge₂Sb₂Te₅ Films. *Jpn. J. Appl. Phys.* **2005**, *44*, 7340.
- (167) Pirovano, A.; Lacaita, A. L.; Benvenuti, A.; Pellizzer, F.; Hudgens, S.; Bez, R. Scaling Analysis of Phase-Change Memory Technology. *IEEE International Electron Devices Meeting 2003* **2003**, 29.6.1–29.6.4.
- (168) Lai, S. Current Status of the Phase Change Memory and Its Future. *IEEE International Electron Devices Meeting 2003* **2003**, 10.1.1–10.1.4.
- (169) Street, R.; Mott, N. States in the Gap in Glassy Semiconductors. *Phys. Rev. Lett.* **1975**, *35*, 1293–1296.
- (170) Hartke, J. The Three-Dimensional Poole-Frenkel Effect. *J. Appl. Phys.* **1968**, *39*, 4871–4873.
- (171) Wang, Y.; Wang, T.; Liu, G.; Guo, T.; Li, T.; Lv, S.; Cheng, Y.; Song, S.; Ren, K.; Song, Z. High Thermal Stability and Fast Speed Phase Change Memory by Optimizing GeSbTe with Scandium Doping. *Scr. Mater.* **2019**, *164*, 25–29.
- (172) Chen, S.; Yang, K.; Wu, W.; Zhai, J.; Song, Z. Superlattice-Like Sb-Ge Thin Films for High Thermal Stability and Low Power Phase Change Memory. *J. Alloys Compd.* **2018**, *738*, 145–150.
- (173) Sebastian, A.; Le Gallo, M.; Burr, G. W.; Kim, S.; BrightSky, M.; Eleftheriou, E. Tutorial: Brain-Inspired Computing Using Phase-Change Memory Devices. *J. Appl. Phys.* **2018**, *124*, 111101.
- (174) Zhang, W.; Mazzarello, R.; Ma, E. Phase-Change Materials in Electronics and Photonics. *MRS Bull.* **2019**, *44*, 686–690.
- (175) Yamada, N.; Ohno, E.; Akahira, N.; Nishiuchi, K. i.; Nagata, K. i.; Takao, M. High Speed Overwritable Phase Change Optical Disk Material. *Jpn. J. Appl. Phys.* **1987**, *26*, 61–66.
- (176) Schubert, E. F. *Doping in III-V Semiconductors*; Cambridge Studies in Semiconductor Physics and Microelectronic Engineering, Series Number 1; Cambridge University Press, 1993.
- (177) Beneventi, G. B.; Perniola, L.; Fantini, A.; Blachier, D.; Toffoli, A.; Gourvest, E.; Maitrejean, S.; Sousa, V.; Jahan, C.; Nodin, J. Carbon-Doped GeTe Phase-Change Memory Featuring Remarkable Reset Current Reduction. *2010 Proceedings of the European Solid State Device Research Conference*, 2010; p 313–316.
- (178) Hubert, Q.; Jahan, C.; Toffoli, A.; Navarro, G.; Chandrashekar, S.; Noe, P.; Blachier, D.; Sousa, V.; Perniola, L.; Nodin, J.-F. Lowering the Reset Current and Power Consumption of Phase-Change Memories with Carbon-Doped Ge₂Sb₂Te₅. *2012 4th IEEE International Memory Workshop* **2012**, 1–4.
- (179) Zhou, X.; Wu, L.; Song, Z.; Rao, F.; Zhu, M.; Peng, C.; Yao, D.; Song, S.; Liu, B.; Feng, S. Carbon-Doped Ge₂Sb₂Te₅ Phase Change Material: A Candidate for High-Density Phase Change Memory Application. *Appl. Phys. Lett.* **2012**, *101*, 142104.
- (180) Song, Z.; Cai, D.; Li, X.; Wang, L.; Chen, Y.; Chen, H.; Wang, Q.; Zhan, Y.; Ji, M. High Endurance Phase Change Memory Chip Implemented Based on Carbon-Doped Ge₂Sb₂Te₅ in 40 nm Node for Embedded Application. *2018 IEEE International Electron Devices Meeting (IEDM)* **2019**, 27.5.1–27.5.4.
- (181) Han, J. H.; Jeong, H.; Park, H.; Kwon, H.; Kim, D.; Lim, D.; Baik, S. J.; Kwon, Y.-K.; Cho, M.-H. Enhanced Reliability of Phase-Change Memory via Modulation of Local Structure and Chemical Bonding by Incorporating Carbon in Ge₂Sb₂Te₅. *RSC Adv.* **2021**, *11*, 22479–22488.
- (182) Horii, H.; Yi, J.; Park, J.; Ha, Y.; Baek, I.; Park, S.; Hwang, Y.; Lee, S.; Kim, Y.; Lee, K.; Moon, J. A Novel Cell Technology Using N-Doped GeSbTe Films for Phase Change RAM. *2003 Symposium on VLSI Technology*, 2003; p 177–178.
- (183) Fantini, A.; Sousa, V.; Perniola, L.; Gourvest, E.; Bastien, J.; Maitrejean, S.; Braga, S.; Pashkov, N.; Bastard, A.; Hyot, B.; et al. N-Doped GeTe as Performance Booster for Embedded Phase-Change Memories. *2010 International Electron Devices Meeting* **2010**, 29.1.1–29.1.4.
- (184) Cheng, H.; Wu, J.; Cheek, R.; Raoux, S.; BrightSky, M.; Garbin, D.; Kim, S.; Hsu, T.; Zhu, Y.; Lai, E.; et al. A Thermally Robust Phase Change Memory by Engineering the Ge/N Concentration in (Ge, N)_xSb_yTe_z Phase Change Material. *2012 International Electron Devices Meeting* **2012**, 31.1.1–31.1.4.
- (185) Raeis-Hosseini, N.; Lim, S.; Hwang, H.; Rho, J. Reliable Ge₂Sb₂Te₅-Integrated High-Density Nanoscale Conductive Bridge Random Access Memory Using Facile Nitrogen-Doping Strategy. *Adv. Electron. Mater.* **2018**, *4*, 1800360.
- (186) Zhang, Z.; Peng, C.; Song, S.; Song, Z.; Cheng, Y.; Ren, K.; Li, X.; Rao, F.; Liu, B.; Feng, S. Characterization of Cu Doping on GeTe for Phase Change Memory Application. *J. Appl. Phys.* **2013**, *114*, 244311.
- (187) Ding, K.; Ren, K.; Rao, F.; Song, Z.; Wu, L.; Liu, B.; Feng, S. Study on the Cu-Doped Ge₂Sb₂Te₅ for Low-Power Phase Change Memory. *Mater. Lett.* **2014**, *125*, 143–146.
- (188) Hu, Y.; Lai, T.; Zou, H.; Zhu, X. Simultaneously High Thermal Stability and Low Power Based on Cu-Doped GeTe Phase Change Material. *Mater. Res. Express* **2019**, *6*, 025907.
- (189) Cao, L.; Wu, L.; Zhu, W.; Ji, X.; Zheng, Y.; Song, Z.; Rao, F.; Song, S.; Ma, Z.; Xu, L. High Thermal Stable and Fast Switching Ni-Ge

Te Alloy for Phase Change Memory Applications. *Appl. Phys. Lett.* **2015**, *107*, 242101.

(190) Zhang, Z.; Song, S.; Song, Z.; Cheng, Y.; Gu, Y.; Wu, L.; Liu, B.; Feng, S. Study on Gegasbte Film for Long Data Retention Phase Change Memory Application. *J. Non-Cryst. Solids* **2013**, *381*, 54–57.

(191) Xu, Y.; Song, S.; Yuan, Z.; Zhao, J.; Song, Z. High Thermal Stability and Fast Speed Phase Change Memory by Optimizing GeTe Alloys with Ru Doping. *ECS J. Solid State Sci. Technol.* **2021**, *10*, 055009.

(192) Wang, Y.; Zheng, Y.; Liu, G.; Li, T.; Guo, T.; Cheng, Y.; Lv, S.; Song, S.; Ren, K.; Song, Z. Scandium Doped Ge₂Sb₂Te₃ for High-Speed and Low-Power-Consumption Phase Change Memory. *Appl. Phys. Lett.* **2018**, *112*, 133104.

(193) Jang, M. H.; Park, S. J.; Ahn, M.; Jeong, K. S.; Park, S. J.; Cho, M.-H.; Song, J. Y.; Jeong, H. Ultrafast Phase Change and Long Durability of BN-Incorporated GeSbTe. *J. Mater. Chem. C* **2015**, *3*, 1707–1715.

(194) Guo, T.; Song, S.; Song, Z.; Ji, X.; Xue, Y.; Chen, L.; Cheng, Y.; Liu, B.; Wu, L.; Qi, M.; et al. SiC-Doped Ge₂Sb₂Te₃ Phase-Change Material: A Candidate for High-Density Embedded Memory Application. *Adv. Electron. Mater.* **2018**, *4*, 1800083.

(195) Navarro, G.; Coue, M.; Kiouseloglou, A.; Noe, P.; Fillot, F.; Delaye, V.; Persico, A.; Roule, A.; Bernard, M.; Sabbione, C.; et al. Trade-Off between SET and Data Retention Performance Thanks to Innovative Materials for Phase-Change Memory. *2013 IEEE International Electron Devices Meeting* **2013**, 21.5.1–21.5.4.

(196) Fugazza, D.; Ielmini, D.; Montemurro, G.; Lacaita, A. L. Temperature- and Time-Dependent Conduction Controlled by Activation Energy in PCM. *2010 International Electron Devices Meeting* **2010**, 29.3.1–29.3.4.

(197) Cheng, H.; Hsu, T.; Raoux, S.; Wu, J.; Du, P.; Breitwisch, M.; Zhu, Y.; Lai, E.; Joseph, E.; Mittal, S.; et al. A High Performance Phase Change Memory with Fast Switching Speed and High Temperature Retention by Engineering the Ge₂Sb₂Te₃ Phase Change Material. *2011 International Electron Devices Meeting* **2011**, 3.4.1–3.4.4.

(198) Luckas, J.; Olk, A.; Jost, P.; Volker, H.; Alvarez, J.; Jaffré, A.; Zalden, P.; Piarristeguy, A.; Pradel, A.; Longeaud, C.; Wuttig, M. Impact of Maxwell Rigidity Transitions on Resistance Drift Phenomena in Ge₂Te_{1-x} Glasses. *Appl. Phys. Lett.* **2014**, *105*, 092108.

(199) Zhu, M.; Wu, L.; Song, Z.; Rao, F.; Cai, D.; Peng, C.; Zhou, X.; Ren, K.; Song, S.; Liu, B.; et al. Ti₁₀Sb₆₀Te₃₀ for Phase Change Memory with High-Temperature Data Retention and Rapid Crystallization Speed. *Appl. Phys. Lett.* **2012**, *100*, 122101.

(200) Xia, M.; Zhu, M.; Wang, Y.; Song, Z.; Rao, F.; Wu, L.; Cheng, Y.; Song, S. Ti-Sb-Te Alloy: A Candidate for Fast and Long-Life Phase-Change Memory. *ACS Appl. Mater. Interfaces* **2015**, *7*, 7627–7634.

(201) Zhu, M.; Xia, M.; Rao, F.; Li, X.; Wu, L.; Ji, X.; Lv, S.; Song, Z.; Feng, S.; Sun, H.; Zhang, S. One Order of Magnitude Faster Phase Change at Reduced Power in Ti-Sb-Te. *Nat. Commun.* **2014**, *5*, 4086.

(202) Zhu, M.; Wu, L.; Rao, F.; Song, Z.; Ren, K.; Ji, X.; Song, S.; Yao, D.; Feng, S. Uniform Ti-Doped Sb₂Te₃ Materials for High-Speed Phase Change Memory Applications. *Appl. Phys. Lett.* **2014**, *104*, 053119.

(203) Zhu, M.; Wu, L.; Rao, F.; Song, Z.; Ji, X.; Yao, D.; Cheng, Y.; Lv, S.; Song, S.; Liu, B.; Xu, L. The Effect of Titanium Doping on the Structure and Phase Change Characteristics of Sb₄Te. *J. Appl. Phys.* **2013**, *114*, 124302.

(204) Liu, Y.-G.; Chen, Y.-F.; Cai, D.-L.; Lu, Y.-Y.; Wu, L.; Yan, S.; Li, Y.; Song, Z.-T. Fast Switching and Low Drift of TiSbTe Thin Films for Phase Change Memory Applications. *Mater. Sci. Semicond. Process.* **2019**, *91*, 399–403.

(205) Peng, C.; Song, Z.; Rao, F.; Wu, L.; Zhu, M.; Song, H.; Liu, B.; Zhou, X.; Yao, D.; Yang, P.; Chu, J. Al₃Sb₃Te Material for Phase Change Memory Application. *Appl. Phys. Lett.* **2011**, *99*, 043105.

(206) Chen, X.; Zheng, Y.; Zhu, M.; Ren, K.; Wang, Y.; Li, T.; Liu, G.; Guo, T.; Wu, L.; Liu, X.; et al. Scandium Doping Brings Speed Improvement in Sb₂Te Alloy for Phase Change Random Access Memory Application. *Sci. Rep.* **2018**, *8*, 6839.

(207) Zou, H.; Hu, Y.; Zhu, X.; Sun, Y.; Zheng, L.; Sui, Y.; Wu, S.; Song, Z. Improvement in Reliability and Power Consumption Based on

Ge₁₀Sb₉₀ Films through Erbium Doping. *J. Mater. Sci.* **2017**, *52*, 5216–5222.

(208) Hwang, S.; Park, H.; Kim, D.; Lim, H.; Lee, C.; Han, J. H.; Kwon, Y.-K.; Cho, M.-H. Ultra-Low Energy Phase Change Memory with Improved Thermal Stability by Tailoring the Local Structure through Ag Doping. *ACS Appl. Mater. Interfaces* **2020**, *12*, 37285–37294.

(209) Liu, R.; Hu, A.; Zhao, Z.; Zhou, H.; Zhai, J.; Zhou, X.; Song, S.; Song, Z. Zn-Doped Sb₇₀Se₃₀ Thin Films with Multiple Phase Transition for High Storage Density and Low Power Consumption Phase Change Memory Applications. *Scr. Mater.* **2020**, *178*, 324–328.

(210) Wu, L.; Li, T.; Ji, X.; Song, S.; Song, Z. Investigation on Thermal Stability of Vanadium-Doped Sb₂Te Phase Change Material. *J. Mater. Sci.: Mater. Electron.* **2020**, *8*, 5879–5885.

(211) Liu, W.; Chen, Y.; Li, T.; Song, Z.; Wu, L. Effect of Mo Doping on Phase Change Performance of Sb₂Te₃. *Chin. Phys. B* **2021**, *30*, 086801.

(212) Xue, Y.; Yan, S.; Lv, S.; Song, S.; Song, Z. Ta-Doped Sb₂Te Allows Ultrafast Phase-Change Memory with Excellent High-Temperature Operation Characteristics. *Nano-Micro Lett.* **2021**, *13*, 33.

(213) Ren, K.; Li, R.; Chen, X.; Wang, Y.; Shen, J.; Xia, M.; Lv, S.; Ji, Z.; Song, Z. Controllable SET Process in O-Ti-Sb-Te Based Phase Change Memory for Synaptic Application. *Appl. Phys. Lett.* **2018**, *112*, 073106.

(214) Ren, K.; Wang, Y.; Lv, S.; Zhu, S.; Xin, T.; Song, Z. Reducing Structural Change in the Phase Transition of Ge-Doped Bi_{0.5}Sb_{1.5}Te₃ to Enable High-Speed and Low-Energy Memory Switching. *J. Mater. Chem. C* **2019**, *7*, 11813–11823.

(215) Ren, K.; Xia, M.; Zhu, S.; Wang, G.; Xin, T.; Lv, S.; Song, Z. Crystal-Like Glassy Structure in Sc-Doped Bisbte Ensuring Excellent Speed and Power Efficiency in Phase Change Memory. *ACS Appl. Mater. Interfaces* **2020**, *12*, 16601–16608.

(216) Zhang, S.; Wu, L.; Song, W.; Zhou, X.; Song, Z.; Shi, J.; Zhang, J.; Feng, S. High Performance Al₃Sc Alloy Doped Al₃Sc-Sb₂Te Chalcogenides for Phase Change Memory Application. *J. Mater. Chem. C* **2018**, *6*, 4177–4182.

(217) Hu, S.; Xiao, J.; Zhou, J.; Elliott, S. R.; Sun, Z. Synergy Effect of Co-Doping Sc and Y in Sb₂Te₃ for Phase-Change Memory. *J. Mater. Chem. C* **2020**, *8*, 6672–6679.

(218) Xu, Y.; Wang, X.; Zhang, W.; Schafer, L.; Reindl, J.; Vom Bruch, F.; Zhou, Y.; Evans, V.; Wang, J. J.; Deringer, V. L.; et al. Materials Screening for Disorder-Controlled Chalcogenide Crystals for Phase-Change Memory Applications. *Adv. Mater.* **2021**, *33*, 2006221.

(219) Liu, Y. T.; Li, X. B.; Zheng, H.; Chen, N. K.; Wang, X. P.; Zhang, X. L.; Sun, H. B.; Zhang, S. High-Throughput Screening for Phase-Change Memory Materials. *Adv. Funct. Mater.* **2021**, *31*, 2009803.

(220) Xue, Y.; Cheng, Y.; Zheng, Y.; Yan, S.; Song, W.; Lv, S.; Song, S.; Song, Z. Phase Change Memory Based on Ta-Sb-Te Alloy -Towards a Universal Memory. *Mater. Today Phys.* **2020**, *15*, 100266.

(221) Ha, Y.; Yi, J.; Horii, H.; Park, J.; Joo, S.; Park, S.; Chung, U.-I.; Moon, J. An Edge Contact Type Cell for Phase Change RAM Featuring Very Low Power Consumption. *2003 Symposium on VLSI Technology*, 2003; pp 175–176.

(222) Hwang, Y.; Lee, S.; Ahn, S.; Lee, S.; Ryoo, K.; Hong, H.; Koo, H. C.; Yeung, F.; Oh, J.; Kim, H.; et al. Writing Current Reduction for High-Density Phase-Change RAM. *IEEE International Electron Devices Meeting 2003* **2003**, 37.1.1–37.1.4.

(223) Kim, W.; BrightSky, M.; Masuda, T.; Sosa, N.; Kim, S.; Bruce, R.; Carta, F.; Fraczak, G.; Cheng, H.; Ray, A.; et al. ALD-Based Confined PCM with a Metallic Liner toward Unlimited Endurance. *2016 IEEE International Electron Devices Meeting (IEDM)* **2016**, 4.2.1–4.2.4.

(224) Lai, S.; Kim, S.; BrightSky, M.; Zhu, Y.; Joseph, E.; Bruce, R.; Cheng, H.; Ray, A.; Raoux, S.; Wu, J. A Scalable Volume-Confined Phase Change Memory Using Physical Vapor Deposition. *2013 Symposium on VLSI Technology*, 2013; pp T132–T133.

(225) Im, D.; Lee, J.; Cho, S.; An, H.; Kim, D.; Kim, I.; Park, H.; Ahn, D.; Horii, H.; Park, S.; et al. A Unified 7.5 nm Dash-Type Confined Cell

for High Performance PRAM Device. *2008 IEEE International Electron Devices Meeting* **2008**, 1–4.

(226) Pellizzer, F.; Pirovano, A.; Ottogalli, F.; Magistretti, M.; Scaravaggi, M.; Zuliani, P.; Tosi, M.; Benvenuti, A.; Besana, P.; Cadeo, S. Novel/spl mu/Trench Phase-Change Memory Cell for Embedded and Stand-Alone Non-Volatile Memory Applications. *2004 Symposium on VLSI Technology*, 2004; pp 18–19.

(227) Pellizzer, F.; Benvenuti, A.; Gleixner, B.; Kim, Y.; Johnson, B.; Magistretti, M.; Marangon, T.; Pirovano, A.; Bez, R.; Atwood, G. A 90 nm Phase Change Memory Technology for Stand-Alone Non-Volatile Memory Applications. *2006 Symposium on VLSI Technology*, 2006; p 122–123.

(228) Yin, Y.; Hosaka, S. Low-Reset-Current Ring-Confined-Chalcogenide Phase Change Memory. *Jpn. J. Appl. Phys.* **2012**, *51*, 104202.

(229) Jeong, C.-W.; Ahn, S.-J.; Hwang, Y.-N.; Song, Y.-J.; Oh, J.-H.; Lee, S.-Y.; Lee, S.-H.; Ryoo, K.-C.; Park, J.-H.; Park, J.-H.; et al. Highly Reliable Ring-Type Contact for High-Density Phase Change Memory. *Jpn. J. Appl. Phys.* **2006**, *45*, 3233.

(230) Kim, C.; Suh, D.-S.; Kim, K. H.; Kang, Y.-S.; Lee, T.-Y.; Khang, Y.; Cahill, D. G. Fullerene Thermal Insulation for Phase Change Memory. *Appl. Phys. Lett.* **2008**, *92*, 013109.

(231) Rao, F.; Song, Z.; Gong, Y.; Wu, L.; Feng, S.; Chen, B. Programming Voltage Reduction in Phase Change Memory Cells with Tungsten Trioxide Bottom Heating Layer/Electrode. *Nanotechnology* **2008**, *19*, 445706.

(232) Xu, C.; Song, Z.; Liu, B.; Feng, S.; Chen, B. Lower Current Operation of Phase Change Memory Cell with a Thin TiO₂ Layer. *Appl. Phys. Lett.* **2008**, *92*, 062103.

(233) Choi, B. J.; Oh, S. H.; Choi, S.; Eom, T.; Shin, Y. C.; Kim, K. M.; Yi, K.-W.; Hwang, C. S.; Kim, Y. J.; Park, H. C.; et al. Switching Power Reduction in Phase Change Memory Cell Using CVD Ge₂Sb₂Te₃ and Ultrathin TiO₂ Films. *J. Electrochem. Soc.* **2009**, *156*, H59.

(234) Song, S.; Song, Z.; Peng, C.; Gao, L.; Gu, Y.; Zhang, Z.; Lv, Y.; Yao, D.; Wu, L.; Liu, B. Performance Improvement of Phase-Change Memory Cell Using ALSb₃Te and Atomic Layer Deposition TiO₂ Buffer Layer. *Nanoscale Res. Lett.* **2013**, *8*, 77.

(235) Koh, Y. K.; Bae, M.-H.; Cahill, D. G.; Pop, E. Heat Conduction across Monolayer and Few-Layer Graphenes. *Nano Lett.* **2010**, *10*, 4363–4368.

(236) Zhu, C.; Ma, J.; Ge, X.; Rao, F.; Ding, K.; Lv, S.; Wu, L.; Song, Z. Low-Energy Phase Change Memory with Graphene Confined Layer. *Appl. Phys. Lett.* **2016**, *108*, 252102.

(237) Chong, T.; Shi, L.; Zhao, R.; Tan, P.; Li, J.; Lee, H.; Miao, X.; Du, A.; Tung, C. Phase Change Random Access Memory Cell with Superlattice-Like Structure. *Appl. Phys. Lett.* **2006**, *88*, 122114.

(238) Ohyanagi, T.; Kitamura, M.; Araidai, M.; Kato, S.; Takaura, N.; Shiraishi, K. GeTe Sequences in Superlattice Phase Change Memories and Their Electrical Characteristics. *Appl. Phys. Lett.* **2014**, *104*, 252106.

(239) Ohyanagi, T.; Takaura, N.; Tai, M.; Kitamura, M.; Kinoshita, M.; Akita, K.; Morikawa, T.; Kato, S.; Araidai, M.; Kamiya, K.; et al. Charge-Injection Phase Change Memory with High-Quality GeTe/Sb₂Te₃ Superlattice Featuring 70- μ A Reset, 10-ns SET and 100M Endurance Cycles Operations. *2013 IEEE International Electron Devices Meeting* **2013**, 30.5.1–30.5.4.

(240) Ohyanagi, T.; Takaura, N. Investigation of Switching Region in Superlattice Phase Change Memories. *AIP Adv.* **2016**, *6*, 105104.

(241) Chia Tan, C.; Shi, L.; Zhao, R.; Guo, Q.; Li, Y.; Yang, Y.; Chong, T.; Malen, J. A.; Ong, W.-L.; Schlesinger, T. E.; et al. Compositionally Matched Nitrogen-Doped Ge₂Sb₂Te₅/Ge₂Sb₂Te₃ Superlattice-Like Structures for Phase Change Random Access Memory. *Appl. Phys. Lett.* **2013**, *103*, 133507.

(242) Hu, Y.; You, H.; Zhu, X.; Zou, H.; Zhang, J.; Song, S.; Song, Z. Superlattice-Like GeTe/Sb Thin Film for Ultra-High Speed Phase Change Memory Applications. *J. Non-Cryst. Solids* **2017**, *457*, 141–144.

(243) Liu, R.; Zhou, X.; Zhai, J.; Song, J.; Wu, P.; Lai, T.; Song, S.; Song, Z. Multilayer Snsb₄Sbse Thin Films for Phase Change Materials

Possessing Ultrafast Phase Change Speed and Enhanced Stability. *ACS Appl. Mater. Interfaces* **2017**, *9*, 27004–27013.

(244) Kalikka, J.; Zhou, X.; Dilcher, E.; Wall, S.; Li, J.; Simpson, R. E. Strain-Engineered Diffusive Atomic Switching in Two-Dimensional Crystals. *Nat. Commun.* **2016**, *7*, 11983.

(245) Zhou, X.; Kalikka, J.; Ji, X.; Wu, L.; Song, Z.; Simpson, R. E. Phase-Change Memory Materials by Design: A Strain Engineering Approach. *Adv. Mater.* **2016**, *28*, 3007–3016.

(246) Okabe, K. L.; Sood, A.; Yalon, E.; Neumann, C. M.; Asheghi, M.; Pop, E.; Goodson, K. E.; Wong, H. S. P. Understanding the Switching Mechanism of Interfacial Phase Change Memory. *J. Appl. Phys.* **2019**, *125*, 184501.

(247) Zhou, L.; Yang, Z.; Wang, X.; Qian, H.; Xu, M.; Cheng, X.; Tong, H.; Miao, X. Resistance Drift Suppression Utilizing GeTe/Sb₂Te₃ Superlattice-Like Phase-Change Materials. *Adv. Electron. Mater.* **2020**, *6*, 1900781.

(248) Xu, Y.; Hu, Y.; Sun, S.; Zhu, X.; Lai, T.; Song, S.; Song, Z. Study on the Performance of Superlattice-Like Thin Film V₂O₅/Sb in Phase Change Memory. *ECS J. Solid State Sci. Technol.* **2020**, *9*, 033003.

(249) Saito, Y.; Mitrofanov, K. V.; Makino, K.; Fons, P.; Kolobov, A. V.; Tominaga, J.; Uesugi, F.; Takeguchi, M. Chalcogenide Materials Engineering for Phase-Change Memory and Future Electronics Applications: From Sb-Te to Bi-Te. *Phys. Status Solidi RRL* **2021**, *15*, 2000414.

(250) Stark, P.; Horst, F.; Dangel, R.; Weiss, J.; Offrein, B. J. Opportunities for Integrated Photonic Neural Networks. *Nanophotonics* **2020**, *9*, 4221–4232.

(251) Wang, J.; Long, Y. On-Chip Silicon Photonic Signaling and Processing: A Review. *Sci. Bull.* **2018**, *63*, 1267–1310.

(252) Yu, N.; Genevet, P.; Kats, M. A.; Aieta, F.; Tetienne, J.-P.; Capasso, F.; Gaburro, Z. Light Propagation with Phase Discontinuities: Generalized Laws of Reflection and Refraction. *Science* **2011**, *334*, 333–337.

(253) Arbabi, A.; Horie, Y.; Bagheri, M.; Faraon, A. Dielectric Metasurfaces for Complete Control of Phase and Polarization with Subwavelength Spatial Resolution and High Transmission. *Nat. Nanotechnol.* **2015**, *10*, 937–943.

(254) Xu, H. X.; Hu, G.; Han, L.; Jiang, M.; Huang, Y.; Li, Y.; Yang, X.; Ling, X.; Chen, L.; Zhao, J.; et al. Chirality-Assisted High-Efficiency Metasurfaces with Independent Control of Phase, Amplitude, and Polarization. *Adv. Opt. Mater.* **2018**, *7*, 1801479.

(255) Zheludev, N. I. Obtaining Optical Properties on Demand. *Science* **2015**, *348*, 973–974.

(256) Makarov, S. V.; Zalogina, A. S.; Tajik, M.; Zuev, D. A.; Rybin, M. V.; Kuchmizhak, A. A.; Juodkakis, S.; Kivshar, Y. Light-Induced Tuning and Reconfiguration of Nanophotonic Structures. *Laser Photonics Rev.* **2017**, *11*, 1700108.

(257) Nemat, A.; Wang, Q.; Hong, M.; Teng, J. Tunable and Reconfigurable Metasurfaces and Metadevices. *Opto-Electron. Adv.* **2018**, *1*, 180009.

(258) Kauranen, M.; Zayats, A. V. Nonlinear Plasmonics. *Nat. Photonics* **2012**, *6*, 737–748.

(259) Huang, Y.-W.; Lee, H. W. H.; Sokhoyan, R.; Pala, R. A.; Thyagarajan, K.; Han, S.; Tsai, D. P.; Atwater, H. A. Gate-Tunable Conducting Oxide Metasurfaces. *Nano Lett.* **2016**, *16*, 5319–5325.

(260) Park, J.; Kang, J.-H.; Kim, S. J.; Liu, X.; Brongersma, M. L. Dynamic Reflection Phase and Polarization Control in Metasurfaces. *Nano Lett.* **2017**, *17*, 407–413.

(261) Alam, M. Z.; De Leon, I.; Boyd, R. W. Large Optical Nonlinearity of Indium Tin Oxide in Its Epsilon-near-Zero Region. *Science* **2016**, *352*, 795–797.

(262) Clerici, M.; Kinsey, N.; DeVault, C.; Kim, J.; Carnemolla, E. G.; Caspani, L.; Shaltout, A.; Faccio, D.; Shalaev, V.; Boltasseva, A.; et al. Controlling Hybrid Nonlinearities in Transparent Conducting Oxides via Two-Colour Excitation. *Nat. Commun.* **2017**, *8*, 15829.

(263) Sherrott, M. C.; Hon, P. W.; Fountaine, K. T.; Garcia, J. C.; Ponti, S. M.; Brar, V. W.; Sweatlock, L. A.; Atwater, H. A. Experimental Demonstration of > 230° Phase Modulation in Gate-Tunable

- Graphene-Gold Reconfigurable Mid-Infrared Metasurfaces. *Nano Lett.* **2017**, *17*, 3017–3034.
- (264) Dabidian, N.; Dutta-Gupta, S.; Kholmanov, I.; Lai, K.; Lu, F.; Lee, J.; Jin, M.; Trendafilov, S.; Khanikaev, A.; Fallahzad, B.; et al. Experimental Demonstration of Phase Modulation and Motion Sensing Using Graphene-Integrated Metasurfaces. *Nano Lett.* **2016**, *16*, 3607–3615.
- (265) Lee, S. H.; Choi, M.; Kim, T.-T.; Lee, S.; Liu, M.; Yin, X.; Choi, H. K.; Lee, S. S.; Choi, C.-G.; Choi, S.-Y.; et al. Switching Terahertz Waves with Gate-Controlled Active Graphene Metamaterials. *Nat. Mater.* **2012**, *11*, 936–941.
- (266) Gao, W.; Shu, J.; Reichel, K.; Nickel, D. V.; He, X.; Shi, G.; Vajtai, R.; Ajayan, P. M.; Kono, J.; Mittleman, D. M.; et al. High-Contrast Terahertz Wave Modulation by Gated Graphene Enhanced by Extraordinary Transmission through Ring Apertures. *Nano Lett.* **2014**, *14*, 1242–1248.
- (267) Ou, J.-Y.; Plum, E.; Jiang, L.; Zheludev, N. I. Reconfigurable Photonic Metamaterials. *Nano Lett.* **2011**, *11*, 2142–2144.
- (268) Holsteen, A. L.; Raza, S.; Fan, P.; Kik, P. G.; Brongersma, M. L. Purcell Effect for Active Tuning of Light Scattering from Semiconductor Optical Antennas. *Science* **2017**, *358*, 1407–1410.
- (269) Malek, S. C.; Ee, H.-S.; Agarwal, R. Strain Multiplexed Metasurface Holograms on a Stretchable Substrate. *Nano Lett.* **2017**, *17*, 3641–3645.
- (270) Gutruf, P.; Zou, C.; Withayachumnankul, W.; Bhaskaran, M.; Sriram, S.; Fumeaux, C. Mechanically Tunable Dielectric Resonator Metasurfaces at Visible Frequencies. *ACS Nano* **2016**, *10*, 133–141.
- (271) Tittel, A.; Mai, P.; Taubert, R.; Dregely, D.; Liu, N.; Giessen, H. Palladium-Based Plasmonic Perfect Absorber in the Visible Wavelength Range and Its Application to Hydrogen Sensing. *Nano Lett.* **2011**, *11*, 4366–4369.
- (272) Duan, X.; Kamin, S.; Liu, N. Dynamic Plasmonic Colour Display. *Nat. Commun.* **2017**, *8*, 14606.
- (273) Wang, M.; Krasnok, A.; Lepeshov, S.; Hu, G.; Jiang, T.; Fang, J.; Korgel, B. A.; Alù, A.; Zheng, Y. Suppressing Material Loss in the Visible and near-Infrared Range for Functional Nanophotonics Using Bandgap Engineering. *Nat. Commun.* **2020**, *11*, 5055.
- (274) Jang, J.; Jeong, H.; Hu, G.; Qiu, C. W.; Nam, K. T.; Rho, J. Kerker-Conditioned Dynamic Cryptographic Nanoprints. *Adv. Opt. Mater.* **2019**, *7*, 1801070.
- (275) Ruiz de Galarreta, C.; Sinev, I.; Alexeev, A. M.; Trofimov, P.; Ladutenko, K.; Garcia-Cuevas Carrillo, S.; Gemo, E.; Baldycheva, A.; Bertolotti, J.; David Wright, C. Reconfigurable Multilevel Control of Hybrid All-Dielectric Phase-Change Metasurfaces. *Optica* **2020**, *7*, 476–484.
- (276) Gholipour, B.; Piccinotti, D.; Karvounis, A.; MacDonald, K. F.; Zheludev, N. I. Reconfigurable Ultraviolet and High-Energy Visible Dielectric Metamaterials. *Nano Lett.* **2019**, *19*, 1643–1648.
- (277) Rensberg, J.; Zhang, S.; Zhou, Y.; McLeod, A. S.; Schwarz, C.; Goldflam, M.; Liu, M.; Kerbusch, J.; Nawrodt, R.; Ramanathan, S.; et al. Active Optical Metasurfaces Based on Defect-Engineered Phase-Transition Materials. *Nano Lett.* **2016**, *16*, 1050–1055.
- (278) Antonellis, N.; Thomas, R.; Kats, M. A.; Vitebskiy, I.; Kottos, T. Nonreciprocity in Photonic Structures with Phase-Change Components. *Phys. Rev. Appl.* **2019**, *11*, 024046.
- (279) Karvounis, A.; Gholipour, B.; MacDonald, K. F.; Zheludev, N. I. All-Dielectric Phase-Change Reconfigurable Metasurface. *Appl. Phys. Lett.* **2016**, *109*, 051103.
- (280) Wang, Q.; Yuan, G.; Kiang, K.; Sun, K.; Gholipour, B.; Rogers, E.; Huang, K.; Ang, S.; Zheludev, N. I.; Teng, J. Reconfigurable Phase-Change Photomask for Grayscale Photolithography. *Appl. Phys. Lett.* **2017**, *110*, 201110.
- (281) Wang, Q.; Rogers, E. T. F.; Gholipour, B.; Wang, C.-M.; Yuan, G.; Teng, J.; Zheludev, N. I. Optically Reconfigurable Metasurfaces and Photonic Devices Based on Phase Change Materials. *Nat. Photonics* **2016**, *10*, 60–65.
- (282) Zhang, Y.; Fowler, C.; Liang, J.; Azhar, B.; Shalaginov, M. Y.; Deckoff-Jones, S.; An, S.; Chou, J. B.; Roberts, C. M.; Liberman, V.; et al. Electrically Reconfigurable Non-Volatile Metasurface Using Low-Loss Optical Phase-Change Material. *Nat. Nanotechnol.* **2021**, *16*, 661–666.
- (283) Chu, C. H.; Tseng, M. L.; Chen, J.; Wu, P. C.; Chen, Y. H.; Wang, H. C.; Chen, T. Y.; Hsieh, W. T.; Wu, H. J.; Sun, G.; et al. Active Dielectric Metasurface Based on Phase-Change Medium. *Laser Photonics Rev.* **2016**, *10*, 986–994.
- (284) Nemati, A.; Yuan, G.; Deng, J.; Huang, A.; Wang, W.; Toh, Y. T.; Teng, J.; Wang, Q. Controllable Polarization-Insensitive and Large-Angle Beam Switching with Phase-Change Metasurfaces. *Adv. Opt. Mater.* **2022**, *10*, 2101847.
- (285) Xiong, J.; Wu, S.-T. Planar Liquid Crystal Polarization Optics for Augmented Reality and Virtual Reality: From Fundamentals to Applications. *eLight* **2021**, *1*, 3.
- (286) Shalaginov, M. Y.; An, S.; Zhang, Y.; Yang, F.; Su, P.; Liberman, V.; Chou, J. B.; Roberts, C. M.; Kang, M.; Rios, C.; et al. Reconfigurable All-Dielectric Metalens with Diffraction-Limited Performance. *Nat. Commun.* **2021**, *12*, 1225.
- (287) Li, S.; Zhou, C.; Ban, G.; Wang, H.; Lu, H.; Wang, Y. Active All-Dielectric Bifocal Metalens Assisted by Germanium Antimony Telluride. *J. Phys. D: Appl. Phys.* **2019**, *52*, 095106.
- (288) Bai, W.; Yang, P.; Wang, S.; Huang, J.; Chen, D.; Zhang, Z.; Yang, J.; Xu, B. Actively Tunable Metalens Array Based on Patterned Phase Change Materials. *Appl. Sci.* **2019**, *9*, 4927.
- (289) Bai, W.; Yang, P.; Wang, S.; Huang, J.; Chen, D.; Zhang, Z.; Yang, J.; Xu, B. Tunable Duplex Metalens Based on Phase-Change Materials in Communication Range. *Nanomater.* **2019**, *9*, 993.
- (290) Yue, F.; Piccoli, R.; Shalaginov, M. Y.; Gu, T.; Richardson, K. A.; Morandotti, R.; Hu, J.; Razzari, L. Nonlinear Mid-Infrared Metasurface Based on a Phase-Change Material. *Laser Photonics Rev.* **2021**, *15*, 2000373.
- (291) Loke, D.; Lee, T.; Wang, W.; Shi, L.; Zhao, R.; Yeo, Y.; Chong, T.; Elliott, S. Breaking the Speed Limits of Phase-Change Memory. *Science* **2012**, *336*, 1566–1569.
- (292) Zhang, Y.; Chou, J. B.; Li, J.; Li, H.; Du, Q.; Yadav, A.; Zhou, S.; Shalaginov, M. Y.; Fang, Z.; Zhong, H.; et al. Broadband Transparent Optical Phase Change Materials for High-Performance Nonvolatile Photonics. *Nat. Commun.* **2019**, *10*, 4279.
- (293) Zhang, T.; Mei, S.; Wang, Q.; Liu, H.; Lim, C. T.; Teng, J. Reconfigurable Optical Manipulation by Phase Change Material Waveguides. *Nanoscale* **2017**, *9*, 6895–6900.
- (294) Zheng, J.; Khanolkar, A.; Xu, P.; Colburn, S.; Deshmukh, S.; Myers, J.; Frantz, J.; Pop, E.; Hendrickson, J.; Doyle, J.; et al. GST-on-Silicon Hybrid Nanophotonic Integrated Circuits: A Non-Volatile Quasi-Continuously Reprogrammable Platform. *Opt. Mater. Express* **2018**, *8*, 1551–1561.
- (295) Stegmaier, M.; Ríos, C.; Bhaskaran, H.; Wright, C. D.; Pernice, W. H. Nonvolatile All-Optical 1×2 Switch for Chipscale Photonic Networks. *Adv. Opt. Mater.* **2017**, *5*, 1600346.
- (296) Kato, K.; Kuwahara, M.; Kawashima, H.; Tsuruoka, T.; Tsuda, H. Current-Driven Phase-Change Optical Gate Switch Using Indium-Tin-Oxide Heater. *Appl. Phys. Express* **2017**, *10*, 072201.
- (297) Wu, C.; Yu, H.; Lee, S.; Peng, R.; Takeuchi, I.; Li, M. Programmable Phase-Change Metasurfaces on Waveguides for Multimode Photonic Convolutional Neural Network. *Nat. Commun.* **2021**, *12*, 96.
- (298) Feldmann, J.; Stegmaier, M.; Gruhler, N.; Ríos, C.; Bhaskaran, H.; Wright, C.; Pernice, W. Calculating with Light Using a Chip-Scale All-Optical Abacus. *Nat. Commun.* **2017**, *8*, 1256.
- (299) Wang, Y.; Zhang, J.; Jin, H.; Xu, P. Reconfigurable and Dual-Polarization Bragg Grating Filter with Phase Change Materials. *Appl. Opt.* **2021**, *60*, 9989–9993.
- (300) Landry, A.; Son, T. V.; Martucci, A.; Haché, A. Color Switching by Polarization Effects in Phase Change Materials. *Opt. Commun.* **2020**, *459*, 124957.
- (301) Zhu, W.; Yang, R.; Fan, Y.; Fu, Q.; Wu, H.; Zhang, P.; Shen, N.-H.; Zhang, F. Controlling Optical Polarization Conversion with Ge₂Sb₂Te₃-Based Phase-Change Dielectric Metamaterials. *Nanoscale* **2018**, *10*, 12054–12061.

- (302) Peng, X.-Y.; Wang, B.; Teng, J.; Kana Kana, J. B.; Zhang, X. Active Near Infrared Linear Polarizer Based on VO₂ Phase Transition. *J. Appl. Phys.* **2013**, *114*, 163103.
- (303) Cao, T.; Zhang, L.; Simpson, R. E.; Wei, C.; Cryan, M. J. Strongly Tunable Circular Dichroism in Gammadion Chiral Phase-Change Metamaterials. *Opt. Express* **2013**, *21*, 27841–27851.
- (304) Xu, P.; Zheng, J.; Doylend, J. K.; Majumdar, A. Low-Loss and Broadband Nonvolatile Phase-Change Directional Coupler Switches. *ACS Photonics* **2019**, *6*, 553–557.
- (305) Luo, Y.; Zhao, Y.; Li, J.; Çetintaş, E.; Rivenson, Y.; Jarrahi, M.; Ozcan, A. Computational Imaging without a Computer: Seeing through Random Diffusers at the Speed of Light. *eLight* **2022**, *2*, 4.
- (306) Zhang, J.; Zhang, L.; Xu, W. Surface Plasmon Polaritons: Physics and Applications. *J. Phys. D: Appl. Phys.* **2012**, *45*, 113001.
- (307) Zayats, A. V.; Smolyaninov, I. I.; Maradudin, A. A. Nano-Optics of Surface Plasmon Polaritons. *Phys. Rep.* **2005**, *408*, 131–314.
- (308) Hillenbrand, R.; Taubner, T.; Keilmann, F. Phonon-Enhanced Light-Matter Interaction at the Nanometre Scale. *Nature* **2002**, *418*, 159–162.
- (309) Dai, S.; Fei, Z.; Ma, Q.; Rodin, A.; Wagner, M.; McLeod, A.; Liu, M.; Gannett, W.; Regan, W.; Watanabe, K.; et al. Tunable Phonon Polaritons in Atomically Thin Van der Waals Crystals of Boron Nitride. *Science* **2014**, *343*, 1125–1129.
- (310) Li, P.; Yang, X.; Maß, T. W.; Hanss, J.; Lewin, M.; Michel, A.-K. U.; Wuttig, M.; Taubner, T. Reversible Optical Switching of Highly Confined Phonon-Polaritons with an Ultrathin Phase-Change Material. *Nat. Mater.* **2016**, *15*, 870–875.
- (311) Ma, W.; Hu, G.; Hu, D.; Chen, R.; Sun, T.; Zhang, X.; Dai, Q.; Zeng, Y.; Alù, A.; Qiu, C.-W.; Li, P. Ghost Hyperbolic Surface Polaritons in Bulk Anisotropic Crystals. *Nature* **2021**, *596*, 362–366.
- (312) Hu, D.; Yang, X.; Li, C.; Liu, R.; Yao, Z.; Hu, H.; Corder, S. N. G.; Chen, J.; Sun, Z.; Liu, M.; Dai, Q. Probing Optical Anisotropy of Nanometer-Thin Van Der Waals Microcrystals by Near-Field Imaging. *Nat. Commun.* **2017**, *8*, 1471.
- (313) Hu, F.; Luan, Y.; Scott, M.; Yan, J.; Mandrus, D.; Xu, X.; Fei, Z. Imaging Excitonpolariton Transport in MoSe₂ Waveguides. *Nat. Photonics* **2017**, *11*, 356–360.
- (314) Babicheva, V. E.; Gamage, S.; Zhen, L.; Cronin, S. B.; Yakovlev, V. S.; Abate, Y. Near-Field Surface Waves in Few-Layer MoS₂. *ACS Photonics* **2018**, *5*, 2106–2112.
- (315) Mrejin, M.; Yadgarov, L.; Levanon, A.; Suchowski, H. Transient Exciton-Polariton Dynamics in WSe₂ by Ultrafast near-Field Imaging. *Sci. Adv.* **2019**, *5*, No. eaat9618.
- (316) Hu, F.; Luan, Y.; Speltz, J.; Zhong, D.; Liu, C.; Yan, J.; Mandrus, D.; Xu, X.; Fei, Z. Imaging Propagative Exciton Polaritons in Atomically Thin WSe₂ Waveguides. *Phys. Rev. B* **2019**, *100*, 121301.
- (317) Sternbach, A. J.; Latini, S.; Chae, S.; Hübener, H.; De Giovannini, U.; Shao, Y.; Xiong, L.; Sun, Z.; Shi, N.; Kissin, P.; et al. Femtosecond Exciton Dynamics in WSe₂ Optical Waveguides. *Nat. Commun.* **2020**, *11*, 3567.
- (318) Hu, D.; Chen, K.; Chen, X.; Guo, X.; Liu, M.; Dai, Q. Tunable Modal Birefringence in a Low-Loss Van der Waals Waveguide. *Adv. Mater.* **2019**, *31*, 1807788.
- (319) Khurgin, J. B. How to Deal with the Loss in Plasmonics and Metamaterials. *Nat. Nanotechnol.* **2015**, *10*, 2–6.
- (320) Alfaro-Mozaz, F.; Alonso-González, P.; Vélez, S.; Dolado, I.; Autore, M.; Mastel, S.; Casanova, F.; Hueso, L.; Li, P.; Nikitin, A. Y.; Hillenbrand, R. Nanoimaging of Resonating Hyperbolic Polaritons in Linear Boron Nitride Antennas. *Nat. Commun.* **2017**, *8*, 15624.
- (321) Giles, A. J.; Dai, S.; Vurgaftman, I.; Hoffman, T.; Liu, S.; Lindsay, L.; Ellis, C. T.; Assefa, N.; Chatzakis, I.; Reinecke, T. L.; et al. Ultralow-Loss Polaritons in Isotopically Pure Boron Nitride. *Nat. Mater.* **2018**, *17*, 134–139.
- (322) Caldwell, J. D.; Kretinin, A. V.; Chen, Y.; Giannini, V.; Fogler, M. M.; Francescato, Y.; Ellis, C. T.; Tischler, J. G.; Woods, C. R.; Giles, A. J.; et al. Sub-Diffractive Volume-Confined Polaritons in the Natural Hyperbolic Material Hexagonal Boron Nitride. *Nat. Commun.* **2014**, *5*, 5221.
- (323) Dubrovkin, A. M.; Qiang, B.; Krishnamoorthy, H. N.; Zheludev, N. I.; Wang, Q. J. Ultra-Confined Surface Phonon Polaritons in Molecular Layers of Van der Waals Dielectrics. *Nat. Commun.* **2018**, *9*, 1762.
- (324) Caldwell, J. D.; Lindsay, L.; Giannini, V.; Vurgaftman, I.; Reinecke, T. L.; Maier, S. A.; Glembocki, O. J. Low-Loss, Infrared and Terahertz Nanophotonics Using Surface Phonon Polaritons. *Nanophotonics* **2015**, *4*, 44–68.
- (325) Basov, D. N.; Fogler, M. M.; Garcia de Abajo, F. J. Polaritons in Van der Waals Materials. *Science* **2016**, *354*, aag1992.
- (326) Low, T.; Chaves, A.; Caldwell, J. D.; Kumar, A.; Fang, N. X.; Avouris, P.; Heinz, T. F.; Guinea, F.; Martin-Moreno, L.; Koppens, F. Polaritons in Layered Two-Dimensional Materials. *Nat. Mater.* **2017**, *16*, 182–194.
- (327) Zhang, Q.; Hu, G.; Ma, W.; Li, P.; Krasnok, A.; Hillenbrand, R.; Alù, A.; Qiu, C.-W. Interface Nano-Optics with Van der Waals Polaritons. *Nature* **2021**, *597*, 187–195.
- (328) Dai, Z.; Hu, G.; Si, G.; Ou, Q.; Zhang, Q.; Balendhran, S.; Rahman, F.; Zhang, B. Y.; Ou, J. Z.; Li, G.; et al. Edge-Oriented and Steerable Hyperbolic Polaritons in Anisotropic Van der Waals Nanocavities. *Nat. Commun.* **2020**, *11*, 6086.
- (329) Chen, J.; Badioli, M.; Alonso-González, P.; Thongrattanasiri, S.; Huth, F.; Osmond, J.; Spasenović, M.; Centeno, A.; Pesquera, A.; Godignon, P.; et al. Optical Nano-Imaging of Gate-Tunable Graphene Plasmons. *Nature* **2012**, *487*, 77–81.
- (330) Fei, Z.; Rodin, A.; Andreev, G. O.; Bao, W.; McLeod, A.; Wagner, M.; Zhang, L.; Zhao, Z.; Thiemens, M.; Dominguez, G.; et al. Gate-Tuning of Graphene Plasmons Revealed by Infrared Nano-Imaging. *Nature* **2012**, *487*, 82–85.
- (331) Huber, M. A.; Mooshammer, F.; Plankl, M.; Viti, L.; Sandner, F.; Kastner, L. Z.; Frank, T.; Fabian, J.; Vitiello, M. S.; Cocker, T. L.; Hiber, R. Femtosecond Photo-Switching of Interface Polaritons in Black Phosphorus Heterostructures. *Nat. Nanotechnol.* **2017**, *12*, 207–211.
- (332) Rodrigo, D.; Limaj, O.; Janner, D.; Etezadi, D.; Garcia De Abajo, F. J.; Pruneri, V.; Altug, H. Mid-Infrared Plasmonic Biosensing with Graphene. *Science* **2015**, *349*, 165–168.
- (333) Sun, Z.; Martinez, A.; Wang, F. Optical Modulators with 2D Layered Materials. *Nat. Photonics* **2016**, *10*, 227–238.
- (334) Yao, B.; Liu, Y.; Huang, S.-W.; Choi, C.; Xie, Z.; Flores, J. F.; Wu, Y.; Yu, M.; Kwong, D.-L.; Huang, Y.; et al. Broadband Gate-Tunable Terahertz Plasmons in Graphene Heterostructures. *Nat. Photonics* **2018**, *12*, 22–28.
- (335) Kurman, Y.; Rivera, N.; Christensen, T.; Tsesses, S.; Orenstein, M.; Soljačić, M.; Joannopoulos, J. D.; Kaminer, I. Control of Semiconductor Emitter Frequency by Increasing Polariton Momenta. *Nat. Photonics* **2018**, *12*, 423–429.
- (336) Li, P.; Lewin, M.; Kretinin, A. V.; Caldwell, J. D.; Novoselov, K. S.; Taniguchi, T.; Watanabe, K.; Gaussmann, F.; Taubner, T. Hyperbolic Phonon-Polaritons in Boron Nitride for Near-Field Optical Imaging and Focusing. *Nat. Commun.* **2015**, *6*, 7507.
- (337) Ma, W.; Alonso-Gonzalez, P.; Li, S.; Nikitin, A. Y.; Yuan, J.; Martin-Sanchez, J.; Taboada-Gutierrez, J.; Amenabar, I.; Li, P.; Velez, S.; et al. In-Plane Anisotropic and Ultra-Low-Loss Polaritons in a Natural Van der Waals Crystal. *Nature* **2018**, *562*, 557–562.
- (338) Zheng, Z.; Chen, J.; Wang, Y.; Wang, X.; Chen, X.; Liu, P.; Xu, J.; Xie, W.; Chen, H.; Deng, S.; et al. Highly Confined and Tunable Hyperbolic Phonon Polaritons in Van der Waals Semiconducting Transition Metal Oxides. *Adv. Mater.* **2018**, *30*, 1705318.
- (339) Hu, G.; Ou, Q.; Si, G.; Wu, Y.; Wu, J.; Dai, Z.; Krasnok, A.; Mazor, Y.; Zhang, Q.; Bao, Q.; et al. Topological Polaritons and Photonic Magic Angles in Twisted α -MoO₃ Bilayers. *Nature* **2020**, *582*, 209–213.
- (340) Taboada-Gutiérrez, J.; Álvarez-Pérez, G.; Duan, J.; Ma, W.; Crowley, K.; Prieto, I.; Bylinkin, A.; Autore, M.; Volkova, H.; Kimura, K.; et al. Broad Spectral Tuning of Ultra-Low-Loss Polaritons in a Van der Waals Crystal by Intercalation. *Nat. Mater.* **2020**, *19*, 964–968.

- (341) Lee, D.; So, S.; Hu, G.; Kim, M.; Badloe, T.; Cho, H.; Kim, J.; Kim, H.; Qiu, C.-W.; Rho, J. Hyperbolic Metamaterials: Fusing Artificial Structures to Natural 2D Materials. *eLight* **2022**, *2*, 1.
- (342) Zheng, Z.; Sun, F.; Huang, W.; Jiang, J.; Zhan, R.; Ke, Y.; Chen, H.; Deng, S. Phonon Polaritons in Twisted Double-Layers of Hyperbolic Van der Waals Crystals. *Nano Lett.* **2020**, *20*, 5301–5308.
- (343) Hu, G.; Krasnok, A.; Mazon, Y.; Qiu, C. W.; Alu, A. Moire Hyperbolic Metasurfaces. *Nano Lett.* **2020**, *20*, 3217–3224.
- (344) Duan, J.; Capote-Robayna, N.; Taboada-Gutierrez, J.; Alvarez-Perez, G.; Prieto, I.; Martin-Sanchez, J.; Nikitin, A. Y.; Alonso-Gonzalez, P. Twisted Nano-Optics: Manipulating Light at the Nanoscale with Twisted Phonon Polaritonic Slabs. *Nano Lett.* **2020**, *20*, 5323–5329.
- (345) Hu, G.; Zheng, C.; Ni, J.; Qiu, C.-W.; Alu, A. Enhanced Light-Matter Interactions at Photonic Magic-Angle Topological Transitions. *Appl. Phys. Lett.* **2021**, *118*, 211101.
- (346) Hu, G.; Qiu, C.-W.; Alu, A. Twistronics for Photons: Opinion. *Opt. Mater. Express* **2021**, *11*, 1377–1382.
- (347) Aghamiri, N. A.; Hu, G.; Fali, A.; Zhang, Z.; Li, J.; Balendhran, S.; Walia, S.; Sri, S.; Edgar, J.; Ramanathan, S.; Abate, A. Reconfigurable Hyperbolic Polaritonics with Correlated Oxide Metasurfaces. *Research Square* **2021**. PPR417247.
- (348) Wu, Y.; Ou, Y.; Yin, Y.; Li, Y.; Ma, W.; Yu, W.; Liu, G.; Cui, X.; Bao, X.; Duan, J.; et al. Chemical Switching of Low-Loss Phonon Polaritons in α -MoO₃ by Hydrogen Intercalation. *Nat. Commun.* **2020**, *11*, 2646.
- (349) Sternbach, A.; Chae, S.; Latini, S.; Rikhter, A.; Shao, Y.; Li, B.; Rhodes, D.; Kim, B.; Schuck, P. J.; Xu, X.; et al. Programmable Hyperbolic Polaritons in Van der Waals Semiconductors. *Science* **2021**, *371*, 617–620.
- (350) Wang, Y.; Landreman, P.; Schoen, D.; Okabe, K.; Marshall, A.; Celano, U.; Wong, H.-S. P.; Park, J.; Brongersma, M. L. Electrical Tuning of Phase-Change Antennas and Metasurfaces. *Nat. Nanotechnol.* **2021**, *16*, 667–672.
- (351) Gholipour, B.; Zhang, J.; MacDonald, K. F.; Hewak, D. W.; Zheludev, N. I. An All-Optical, Non-Volatile, Bidirectional, Phase-Change Meta-Switch. *Adv. Mater.* **2013**, *25*, 3050–3054.
- (352) Michel, A. K. U.; Meyer, S.; Essing, N.; Lassaline, N.; Lightner, C. R.; Bisig, S.; Norris, D. J.; Chigrin, D. N. The Potential of Combining Thermal Scanning Probes and Phase-Change Materials for Tunable Metasurfaces. *Adv. Opt. Mater.* **2021**, *9*, 2001243.
- (353) Michel, A. K. U.; Heßler, A.; Meyer, S.; Pries, J.; Yu, Y.; Kalix, T.; Lewin, M.; Hans, J.; De Rose, A.; Maß, T. W.; et al. Advanced Optical Programming of Individual Meta-Atoms Beyond the Effective Medium Approach. *Adv. Mater.* **2019**, *31*, 1901033.
- (354) Polking, M. J.; Jain, P. K.; Bekenstein, Y.; Banin, U.; Millo, O.; Ramesh, R.; Alivisatos, A. P. Controlling Localized Surface Plasmon Resonances in GeTe Nanoparticles Using an Amorphous-to-Crystalline Phase Transition. *Phys. Rev. Lett.* **2013**, *111*, 037401.
- (355) Tittel, A.; Michel, A. K. U.; Schäferling, M.; Yin, X.; Gholipour, B.; Cui, L.; Wuttig, M.; Taubner, T.; Neubrech, F.; Giessen, H. A Switchable Mid-Infrared Plasmonic Perfect Absorber with Multi-spectral Thermal Imaging Capability. *Adv. Mater.* **2015**, *27*, 4597–4603.
- (356) Michel, A.-K. U.; Chigrin, D. N.; Maß, T. W.; Schönauer, K.; Salinga, M.; Wuttig, M.; Taubner, T. Using Low-Loss Phase-Change Materials for Mid-Infrared Antenna Resonance Tuning. *Nano Lett.* **2013**, *13*, 3470–3475.
- (357) Pitchappa, P.; Kumar, A.; Prakash, S.; Jani, H.; Venkatesan, T.; Singh, R. Chalcogenide Phase Change Material for Active Terahertz Photonics. *Adv. Mater.* **2019**, *31*, 1808157.
- (358) Yin, X.; Schäferling, M.; Michel, A.-K. U.; Tittel, A.; Wuttig, M.; Taubner, T.; Giessen, H. Active Chiral Plasmonics. *Nano Lett.* **2015**, *15*, 4255–4260.
- (359) Kim, Y.; Wu, P. C.; Sokhoyan, R.; Mauser, K.; Glauddell, R.; Kafaie Shirmanesh, G.; Atwater, H. A. Phase Modulation with Electrically Tunable Vanadium Dioxide Phase-Change Metasurfaces. *Nano Lett.* **2019**, *19*, 3961–3968.
- (360) Yin, X.; Steinle, T.; Huang, L.; Taubner, T.; Wuttig, M.; Zentgraf, T.; Giessen, H. Beam Switching and Bifocal Zoom Lensing Using Active Plasmonic Metasurfaces. *Light Sci. Appl.* **2017**, *6*, No. e17016.
- (361) Ha, Y.; Guo, Y.; Pu, M.; Li, X.; Ma, X.; Luo, X. Tunable Beam Manipulation Based on Phase-Change Metasurfaces. *Appl. Opt.* **2019**, *58*, 7996–8001.
- (362) Deng, Z.-L.; Deng, J.; Zhuang, X.; Wang, S.; Li, K.; Wang, Y.; Chi, Y.; Ye, X.; Xu, J.; Wang, G. P.; et al. Diatomic Metasurface for Vectorial Holography. *Nano Lett.* **2018**, *18*, 2885–2892.
- (363) Devlin, R. C.; Ambrosio, A.; Rubin, N. A.; Mueller, J. B.; Capasso, F. Arbitrary Spin-to-Orbital Angular Momentum Conversion of Light. *Science* **2017**, *358*, 896–901.
- (364) Pu, M.; Li, X.; Ma, X.; Wang, Y.; Zhao, Z.; Wang, C.; Hu, C.; Gao, P.; Huang, C.; Ren, H.; et al. Catenary Optics for Achromatic Generation of Perfect Optical Angular Momentum. *Sci. Adv.* **2015**, *1*, No. e1500396.
- (365) Tsai, W. Y.; Sun, Q.; Hu, G.; Wu, P. C.; Lin, R. J.; Qiu, C. W.; Ueno, K.; Misawa, H.; Tsai, D. P. Twisted Surface Plasmons with Spin-Controlled Gold Surfaces. *Adv. Opt. Mater.* **2019**, *7*, 1801060.
- (366) Jin, Z.; Janoschka, D.; Deng, J.; Ge, L.; Dreher, P.; Frank, B.; Hu, G.; Ni, J.; Yang, Y.; Li, J.; et al. Phyllotaxis-Inspired Nanosieves with Multiplexed Orbital Angular Momentum. *eLight* **2021**, *1*, 5.
- (367) Zhang, F.; Xie, X.; Pu, M.; Guo, Y.; Ma, X.; Li, X.; Luo, J.; He, Q.; Yu, H.; Luo, X. Multistate Switching of Photonic Angular Momentum Coupling in Phase-Change Metadevices. *Adv. Mater.* **2020**, *32*, 1908194.
- (368) Zhang, M.; Pu, M.; Zhang, F.; Guo, Y.; He, Q.; Ma, X.; Huang, Y.; Li, X.; Yu, H.; Luo, X. Plasmonic Metasurfaces for Switchable Photonic Spin-Orbit Interactions Based on Phase Change Materials. *Adv. Sci.* **2018**, *5*, 1800835.
- (369) Zhang, F.; Zhang, M.; Ou, Y.; Cai, J.; Yu, H. Metasurfaces for Independent Manipulation of the Wavefronts in the Different States of Phase Change Materials. *Appl. Phys. Express* **2019**, *12*, 012003.
- (370) Farmakidis, N.; Youngblood, N.; Li, X.; Tan, J.; Swett, J. L.; Cheng, Z.; Wright, C. D.; Pernice, W. H. P.; Bhaskaran, H. Plasmonic Nanogap Enhanced Phase-Change Devices with Dual Electrical-Optical Functionality. *Sci. Adv.* **2019**, *5*, No. eaaw2687.
- (371) Sumikura, H.; Wang, T.; Li, P.; Michel, A.-K. U.; Heßler, A.; Jung, L.; Lewin, M.; Wuttig, M.; Chigrin, D. N.; Taubner, T. Highly Confined and Switchable Mid-Infrared Surface Phonon Polariton Resonances of Planar Circular Cavities with a Phase Change Material. *Nano Lett.* **2019**, *19*, 2549–2554.
- (372) Fali, A.; White, S. T.; Folland, T. G.; He, M.; Aghamiri, N. A.; Liu, S.; Edgar, J. H.; Caldwell, J. D.; Haglund, R. F.; Abate, Y. Refractive Index-Based Control of Hyperbolic Phonon-Polariton Propagation. *Nano Lett.* **2019**, *19*, 7725–7734.
- (373) Dai, S.; Zhang, J.; Ma, Q.; Kittiwatanakul, S.; McLeod, A.; Chen, X.; Corder, S. G.; Watanabe, K.; Taniguchi, T.; Lu, J.; et al. Phase-Change Hyperbolic Heterostructures for Nanopolaritonics: A Case Study of hBN/VO₂. *Adv. Mater.* **2019**, *31*, 1900251.
- (374) Alonso-González, P.; Nikitin, A. Y.; Golmar, F.; Centeno, A.; Pesquera, A.; Vélez, S.; Chen, J.; Navickaite, G.; Koppens, F.; Zurutuza, A.; et al. Controlling Graphene Plasmons with Resonant Metal Antennas and Spatial Conductivity Patterns. *Science* **2014**, *344*, 1369–1373.
- (375) Agassi, J. The Kirchhoff-Planck Radiation Law. *Science* **1967**, *156*, 30–37.
- (376) Xu, Z.; Luo, H.; Zhu, H.; Hong, Y.; Shen, W.; Ding, J.; Kaur, S.; Ghosh, P.; Qiu, M.; Li, Q. Nonvolatile Optically Reconfigurable Radiative Metasurface with Visible Tunability for Anticounterfeiting. *Nano Lett.* **2021**, *21*, 5269–5276.
- (377) Ono, M.; Chen, K.; Li, W.; Fan, S. Self-Adaptive Radiative Cooling Based on Phase Change Materials. *Opt. Express* **2018**, *26*, A777–A787.
- (378) Wu, X.; Yuan, L.; Weng, X.; Qi, L.; Wei, B.; He, W. Passive Smart Thermal Control Coatings Incorporating CaF₂/VO₂ Core-Shell Microsphere Structures. *Nano Lett.* **2021**, *21*, 3908–3914.

- (379) Fan, S.; Li, W. Photonics and Thermodynamics Concepts in Radiative Cooling. *Nat. Photonics* **2022**, *16*, 182–190.
- (380) Liu, D.; Cheng, H.; Xing, X.; Zhang, C.; Zheng, W. Thermo-chromic Properties of W-Doped VO₂ Thin Films Deposited by Aqueous Sol-Gel Method for Adaptive Infrared Stealth Application. *Infrared Phys. Technol.* **2016**, *77*, 339–343.
- (381) Lee, S.; Hippalgaonkar, K.; Yang, F.; Hong, J.; Ko, C.; Suh, J.; Liu, K.; Wang, K.; Urban, J. J.; Zhang, X.; et al. Anomalous Low Electronic Thermal Conductivity in Metallic Vanadium Dioxide. *Science* **2017**, *355*, 371–374.
- (382) Modi, G.; Stach, E. A.; Agarwal, R. Low-Power Switching through Disorder and Carrier Localization in Bismuth-Doped Germanium Telluride Phase Change Memory Nanowires. *ACS Nano* **2020**, *14*, 2162–2171.
- (383) Ito, K.; Nishikawa, K.; Iizuka, H.; Toshiyoshi, H. Experimental Investigation of Radiative Thermal Rectifier Using Vanadium Dioxide. *Appl. Phys. Lett.* **2014**, *105*, 253503.
- (384) Boyd, R. W. *Radiometry and the Detection of Optical Radiation*; John Wiley and Sons, 1983; pp 1–254.
- (385) Barker Jr, A.; Verleur, H.; Guggenheim, H. Infrared Optical Properties of Vanadium Dioxide above and Below the Transition Temperature. *Phys. Rev. Lett.* **1966**, *17*, 1286–1289.
- (386) 2015 Residential Energy Consumption Survey; U.S. Energy Information Administration: Washington, DC, 2015.
- (387) Gentle, A. R.; Smith, G. B. A Subambient Open Roof Surface under the Mid-Summer Sun. *Adv. Sci.* **2015**, *2*, 1500119.
- (388) Dong, M.; Chen, N.; Zhao, X.; Fan, S.; Chen, Z. Nighttime Radiative Cooling in Hot and Humid Climates. *Opt. Express* **2019**, *27*, 31587–31598.
- (389) Orel, B.; Gunde, M. K.; Krainer, A. Radiative Cooling Efficiency of White Pigmented Paints. *Sol. Energy* **1993**, *50*, 477–482.
- (390) Zhai, Y.; Ma, Y.; David, S. N.; Zhao, D.; Lou, R.; Tan, G.; Yang, R.; Yin, X. Scalable-Manufactured Randomized Glass-Polymer Hybrid Metamaterial for Daytime Radiative Cooling. *Science* **2017**, *355*, 1062–1066.
- (391) Mandal, J.; Fu, Y.; Overvig, A. C.; Jia, M.; Sun, K.; Shi, N. N.; Zhou, H.; Xiao, X.; Yu, N.; Yang, Y. Hierarchically Porous Polymer Coatings for Highly Efficient Passive Daytime Radiative Cooling. *Science* **2018**, *362*, 315–319.
- (392) Li, T.; Zhai, Y.; He, S.; Gan, W.; Wei, Z.; Heidarinejad, M.; Dalgo, D.; Mi, R.; Zhao, X.; Song, J.; et al. A Radiative Cooling Structural Material. *Science* **2019**, *364*, 760–763.
- (393) Ulpiani, G.; Ranzi, G.; Shah, K. W.; Feng, J.; Santamouris, M. On the Energy Modulation of Daytime Radiative Coolers: A Review on Infrared Emissivity Dynamic Switch against Overcooling. *Sol. Energy* **2020**, *209*, 278–301.
- (394) Sun, K.; Riedel, C. A.; Urbani, A.; Simeoni, M.; Mengali, S.; Zalkovskij, M.; Bilenberg, B.; De Groot, C.; Muskens, O. L. VO₂ Thermo-chromic Metamaterial-Based Smart Optical Solar Reflector. *ACS Photonics* **2018**, *5*, 2280–2286.
- (395) Williams, O. M. Dynamic Infrared Scene Projection: A Review. *Infrared Phys. Technol.* **1998**, *39*, 473–486.
- (396) Liu, X.; Padilla, W. J. Reconfigurable Room Temperature Metamaterial Infrared Emitter. *Optica* **2017**, *4*, 430–433.
- (397) Lee, J.; Sul, H.; Jung, Y.; Kim, H.; Han, S.; Choi, J.; Shin, J.; Kim, D.; Jung, J.; Hong, S.; Ko, S. H. Thermally Controlled, Active Imperceptible Artificial Skin in Visible-to-Infrared Range. *Adv. Funct. Mater.* **2020**, *30*, 2003328.
- (398) Hong, S.; Shin, S.; Chen, R. An Adaptive and Wearable Thermal Camouflage Device. *Adv. Funct. Mater.* **2020**, *30*, 1909788.
- (399) Coppens, Z. J.; Valentine, J. G. Spatial and Temporal Modulation of Thermal Emission. *Adv. Mater.* **2017**, *29*, 1701275.
- (400) Wang, H.; Yang, Y.; Wang, L. Wavelength-Tunable Infrared Metamaterial by Tailoring Magnetic Resonance Condition with VO₂ Phase Transition. *J. Appl. Phys.* **2014**, *116*, 123503.
- (401) Mao, Z.; Wang, W.; Liu, Y.; Zhang, L.; Xu, H.; Zhong, Y. Infrared Stealth Property Based on Semiconductor (M)-to-Metallic (R) Phase Transition Characteristics of W-Doped VO₂ Thin Films Coated on Cotton Fabrics. *Thin Solid Films* **2014**, *558*, 208–214.
- (402) Thorn, R.; Simpson, O. Spectral Emissivities of Graphite and Carbon. *J. Appl. Phys.* **1953**, *24*, 633–639.
- (403) Kats, M. A.; Sharma, D.; Lin, J.; Genevet, P.; Blanchard, R.; Yang, Z.; Qazilbash, M. M.; Basov, D.; Ramanathan, S.; Capasso, F. Ultra-Thin Perfect Absorber Employing a Tunable Phase Change Material. *Appl. Phys. Lett.* **2012**, *101*, 221101.
- (404) Kim, H.; Cheung, K.; Auyeung, R. C.; Wilson, D. E.; Charipar, K. M.; Piqué, A.; Charipar, N. A. VO₂-Based Switchable Radiator for Spacecraft Thermal Control. *Sci. Rep.* **2019**, *9*, 11329.
- (405) Kocer, H.; Butun, S.; Palacios, E.; Liu, Z.; Tongay, S.; Fu, D.; Wang, K.; Wu, J.; Aydin, K. Intensity Tunable Infrared Broadband Absorbers Based on VO₂ Phase Transition Using Planar Layered Thin Films. *Sci. Rep.* **2015**, *5*, 13384.
- (406) Zhu, M.; Ren, K.; Song, Z. Ovonic Threshold Switching Selectors for Three-Dimensional Stackable Phase-Change Memory. *MRS Bull.* **2019**, *44*, 715–720.
- (407) Ketov, S.; Sun, Y.; Nachum, S.; Lu, Z.; Checchi, A.; Beraldin, A.; Bai, H.; Wang, W.; Louzguine-Luzgin, D.; Carpenter, M.; Greer, A. L. Rejuvenation of Metallic Glasses by Non-Affine Thermal Strain. *Nature* **2015**, *524*, 200–203.
- (408) Zhou, G.; Dai, P.; Wu, J.; Jin, B.; Wen, Q.; Zhu, G.; Shen, Z.; Zhang, C.; Kang, L.; Xu, W.; et al. Broadband and High Modulation-Depth THz Modulator Using Low Bias Controlled VO₂-Integrated Metasurface. *Opt. Express* **2017**, *25*, 17322–17328.
- (409) Kargar, R.; Rouhi, K.; Abdolali, A. Reprogrammable Multifocal THz Metalens Based on Metal-Insulator Transition of VO₂-Assisted Digital Metasurface. *Opt. Commun.* **2020**, *462*, 125331.
- (410) Wang, D.; Zhang, L.; Gu, Y.; Mehmood, M. Q.; Gong, Y.; Srivastava, A.; Jian, L.; Venkatesan, T.; Qiu, C.-W.; Hong, M. Switchable Ultrathin Quarter-Wave Plate in Terahertz Using Active Phase-Change Metasurface. *Sci. Rep.* **2015**, *5*, 15020.
- (411) Feldmann, J.; Youngblood, N.; Karpov, M.; Gehring, H.; Li, X.; Stappers, M.; Le Gallo, M.; Fu, X.; Lukashchuk, A.; Raja, A. S.; et al. Parallel Convolutional Processing Using an Integrated Photonic Tensor Core. *Nature* **2021**, *589*, 52–58.
- (412) Rios, C.; Youngblood, N.; Cheng, Z.; Le Gallo, M.; Pernice, W. H.; Wright, C. D.; Sebastian, A.; Bhaskaran, H. In-Memory Computing on a Photonic Platform. *Sci. Adv.* **2019**, *5*, No. eaau5759.
- (413) Feldmann, J.; Youngblood, N.; Wright, C. D.; Bhaskaran, H.; Pernice, W. H. All-Optical Spiking Neurosynaptic Networks with Self-Learning Capabilities. *Nature* **2019**, *569*, 208–214.
- (414) Chakraborty, I.; Saha, G.; Roy, K. Photonic In-Memory Computing Primitive for Spiking Neural Networks Using Phase-Change Materials. *Phys. Rev. Appl.* **2019**, *11*, 014063.
- (415) Michel, A.-K. U.; Zalden, P.; Chigrin, D. N.; Wuttig, M.; Lindenberg, A. M.; Taubner, T. Reversible Optical Switching of Infrared Antenna Resonances with Ultrathin Phase-Change Layers Using Femtosecond Laser Pulses. *ACS Photonics* **2014**, *1*, 833–839.
- (416) Zhu, H.; Li, Q.; Zheng, C.; Hong, Y.; Xu, Z.; Wang, H.; Shen, W.; Kaur, S.; Ghosh, P.; Qiu, M. High-Temperature Infrared Camouflage with Efficient Thermal Management. *Light Sci. Appl.* **2020**, *9*, 60.
- (417) Luo, H.; Li, Q.; Du, K.; Xu, Z.; Zhu, H.; Liu, D.; Cai, L.; Ghosh, P.; Qiu, M. An Ultra-Thin Colored Textile with Simultaneous Solar and Passive Heating Abilities. *Nano Energy* **2019**, *65*, 103998.
- (418) Luo, H.; Zhu, Y.; Xu, Z.; Hong, Y.; Ghosh, P.; Kaur, S.; Wu, M.; Yang, C.; Qiu, M.; Li, Q. Outdoor Personal Thermal Management with Simultaneous Electricity Generation. *Nano Lett.* **2021**, *21*, 3879–3886.
- (419) Franklin, D.; Modak, S.; Vázquez-Guardado, A.; Safaei, A.; Chanda, D. Covert Infrared Image Encoding through Imprinted Plasmonic Cavities. *Light Sci. Appl.* **2018**, *7*, 93.
- (420) Zhu, H.; Li, Q.; Tao, C.; Hong, Y.; Xu, Z.; Shen, W.; Kaur, S.; Ghosh, P.; Qiu, M. Multispectral Camouflage for Infrared, Visible, Lasers and Microwave with Radiative Cooling. *Nat. Commun.* **2021**, *12*, 1805.
- (421) Xu, C.; Stiubianu, G. T.; Gorodetsky, A. A. Adaptive Infrared-Reflecting Systems Inspired by Cephalopods. *Science* **2018**, *359*, 1495–1500.

(422) Salihoglu, O.; Uzlu, H. B.; Yakar, O.; Aas, S.; Balci, O.; Kakenov, N.; Balci, S.; Olcum, S.; Süzer, S.; Kocabas, C. Graphene-Based Adaptive Thermal Camouflage. *Nano Lett.* **2018**, *18*, 4541–4548.

Recommended by ACS

Recent Advances in Tunable Metasurfaces: Materials, Design, and Applications

Omar A. M. Abdelraouf, Hong Liu, *et al.*

AUGUST 17, 2022
ACS NANO

READ 

2D Monolayers for Superior Transparent Electromagnetic Interference Shielding

Dillon C. Yost, Jeffrey C. Grossman, *et al.*

JUNE 06, 2022
ACS NANO

READ 

Relaxing Symmetry Rules for Nonlinear Optical Interactions in Van der Waals Materials via Strong Light–Matter Coupling

Mandeep Khatoniar, Vinod M Menon, *et al.*

JANUARY 26, 2022
ACS PHOTONICS

READ 

Reconfigurable and Nonvolatile Terahertz Metadevices Based on a Phase-Change Material

Xieyu Chen, Zhen Tian, *et al.*

MARCH 10, 2022
ACS PHOTONICS

READ 

Get More Suggestions >
